IMPERIAL

Directional Ice Templating for Cathode and Anode of Lithium Ion Batteries

Guanting Li

Supervisor: Dr. Chun Ann Huang

Imperial College London
Department of materials

Submitted in part fulfilment of the requirements
For the degree of Doctor of Philosophy at
Imperial College London, Oct 2025



I hereby declare that this thesis and the work reported herein was composed by and originated entirely from me. Information derived from the published and unpublished work of others has been acknowledged in the text and references are given in the list of sources.

Guanting Li (2025)

The copyright of this thesis rests with the author. Unless otherwise indicated, its contents are licensed under a Creative Commons Attribution-NonCommercial 4.0 International Licence (CC BY-NC). Under this licence, you may copy and redistribute the material in any medium or format. You may also create and distribute modified versions of the work. This is on the condition that you credit the author and do not use it, or any derivative works, for a commercial purpose. When reusing or sharing this work, ensure you make the licence terms clear to others by naming the licence and linking to the licence text. Where a work has been adapted, you should indicate that the work has been changed and describe those changes. Please seek permission from the copyright holder for uses of this work that are not included in this licence or permitted under UK Copyright Law.

Abstract

This thesis investigates the development of sustainable and scalable fabrication strategies for lithium-ion battery electrodes using Directional Ice Templating (DIT). The aim was to overcome the limitations of conventional slurry coating, particularly the use of toxic NMP solvents and the inability to control electrode microstructure. Chapter 1 provided the background and motivation for the study, highlighting the importance of thick, low-tortuosity electrodes for next-generation energy storage. Chapter 2 described the materials and experimental methods, including the design of aqueous electrode slurries, fabrication procedure and characterization techniques.

Chapter 3 demonstrated the feasibility of an aqueous DIT process to fabricate NMC811 cathodes with vertically aligned structures. This architecture enhanced both electronic and ionic transport kinetics while eliminating the need for NMP solvent. Surface-sensitive techniques confirmed the chemical stability of NMC811 under aqueous processing, and electrochemical testing showed that DIT cathodes delivered significantly higher capacities and energy densities than slurry coating electrodes.

Chapter 4 addressed scalability of DIT method and developed a directional extreme supercooling process to fabricate ultra-thick electrodes with mass loadings up to 70 mg cm^{-2} with large scale. A systematic calendaring study identified 30% reduction as the critical threshold for balancing vertical alignment with packing density. At this point, DIT cathodes achieved high volumetric capacity, low impedance and superior pouch cell energy density compared to slurry coating controls, validating the method for industrial relevance.

Chapter 5 extended the versatility of DIT to graphite anodes. Thick, free-standing DIT anodes exhibited high mass loading and excellent reversibility. They also showed lithium-ion diffusion

coefficients several orders of magnitude higher than slurry coating electrodes. This demonstrated that DIT could overcome thickness limitations on both cathode and anode sides.

Together, these results establish DIT as a sustainable, scalable, and versatile electrode fabrication strategy, with significant implications for high energy density lithium-ion batteries in electric vehicles and grid-scale storage.

Acknowledgements

Time flies, and my four-year PhD journey is now approaching its end. At this moment, I would like to express my deepest gratitude to my supervisor, Dr. Chun Huang. From the very first email I sent expressing my interest in her research, she treated me with patience and respect. Throughout my PhD, she has guided me with her profound knowledge, unwavering patience, and continuous encouragement. Her kindness, passion for research, and professionalism have not only shaped my academic growth but also inspired me personally. I am especially grateful for the opportunity she gave me to enter and grow in this field. As her second PhD student, I regard her as a role model in both academia and life.

I would also like to sincerely thank all those who have provided technical assistance and support throughout my research. I am grateful to Dr. Mahmoud Ardakani and Dr. Cati Ware for their guidance with SEM and TEM training, and for their invaluable help whenever I encountered challenges in microscopy. My thanks also go to Dr. Gwilherm Kerherve, and Mr. Willam Skinner who trained me in XPS and provided helpful advice during my work. I am indebted to Dr. Jin Su for his assistance with the ToF-SIMS experiments and to Mr. Kaiyi Wang for his support with the TGA measurements. I would also like to thank Mr. Jiapeng Song for his help with 3D printing moulds, which greatly accelerated the progress of my experiments. These contributions were fundamental to building the results presented in this thesis. I am also thankful to Dr. Annalisa Neri, our department's postgraduate research coordinator, whose energy, kindness, and continuous support made a real difference. She has always stood on the side of students, helped resolve difficulties, organized events to build community and cared deeply about our wellbeing. I would further like to acknowledge the valuable discussions I had with Prof. Stephen Skinner, whose leadership in solid-state battery research provided inspiration, and with Dr. Mengzheng Ouyang and Dr. Tianhao He who generously shared his knowledge and advice.

I am deeply grateful to all my friends and colleagues who have accompanied me during my PhD journey. Their encouragement, companionship, and support have made this experience far more enjoyable and meaningful. In particular, I would like to thank Dr. Yidong Han, Mr. Tianyi Zhang, Dr. Haochen Zhou, Mr. Zhixu Zhu and Mr. Feiran Li for their friendship, stimulating discussions and countless moments of laughter both inside and outside the lab. I also extend my appreciation to all members of our research group and the department, who created a collaborative and welcoming environment.

Finally, I owe my deepest gratitude to my family. First, to my father Mr. Qiang Li and my mother Mrs. Shulin Shen, who have supported my education from childhood to the final year of my PhD. They helped me develop strong learning abilities and always stood by me no matter what happened. Their encouragement gave me the confidence to explore new fields and face challenges without fear. I am also deeply thankful to my wife Weitong Xia, whom I met just before starting my PhD. She gave me great support in life and allowed me to focus on my research. She always trusted me and believed that I could succeed. During this time, she also brought our daughter Charlotte Beining Li into the world. Her presence has been the best comfort whenever I felt anxious about my research.

This thesis would not have been possible without the guidance, support, and encouragement of many people, to whom I am truly grateful.

Publications and Conference

Journal Articles

1. Li, G., …, Huang, C.
   Battery Cathode with Vertically Aligned Microstructure Fabricated by Directional Ice Templating, Small Science, Vol. 5, Issue 8, 22 May 2025. (Published)
2. Li, G., …, Huang, C.
   Fabrication Method of Directional Microstructure for High Energy Density, High Power Battery Cathodes. (Under review)
3. Li, G., …, Huang, C.
   Ultra-thick Graphite Anode Vertical Microstructure by Directional Ice Templating. (Manuscript completed)

Conference Presentations

41st International Battery Seminar & Exhibit, Florida, USA

Poster: *Developing New Manufacturing Method of Electrodes for Lithium-ion Batteries*

Contents

Abstract 3

Acknowledgements 5

Publications and Conference 8
Journal Articles 8
Conference Presentations 8

Abbreviations 16

1 Introduction 17
1.1 Why Lithium-ion Battery as Energy Storage Solution 18
1.2 Background of Lithium-ion battery 22
1.2.1 Brief History of the Development of Lithium Ion Battery 22
1.2.2 The Components and Working Principle of LIBs 23
1.2.3 The Importance of Electrode Design in Performance 25
1.3 Conventional Electrode Fabrication and Limitation 27
1.3.1 Conventional Electrode Fabrication 27
1.3.2 The Limitation of Conventional Electrode Fabrication 28
1.4 Directional Ice Templating (DIT): a novel electrode fabrication strategy 30
1.4.1 Process Overview and Principles 30
1.4.2 Prior Research of DIT in Battery Electrode 32
1.4.3 Limitations of Alternative Microstructure-controlled Methods for Electrode Fabrication 34
1.4.4 Advantages and Challenge of DIT Method 35
1.5 Research Objectives and Scope 36
1.6 Motivation of the Thesis 37
1.6.1 Motivation of Chapter 3 38
1.6.2 Motivation of Chapter 4 39
1.6.3 Motivation of Chapter 5 39
1.6.4 Research Significance and Potential Impact 40

2 Materials and Methods 42
2.1 Materials Applied 43
2.1.1 Cathode Materials 43
2.1.2 Anode Materials 46
2.1.3 Other Materials 47
2.2 Electrode Fabrication Procedure 48
2.2.1 Conventional Slurry Coating Cathode 49
2.2.2 Small-scale DIT Cathode 49
2.2.3 Scale-up DIT Cathode 50
2.2.4 Conventional Slurry Coating Graphite Anode 51
2.2.5 Small-scale DIT Graphite Anode 52
2.3 NMC811 Water Exposure Study Characterization 52

2.3.1 Transmission Electron Microscope (TEM) 53
2.3.2 Time-of-Flight Secondary Ion Mass Spectrometry (ToF-SIMS) 54
2.3.3 X-ray Photoelectron Spectroscopy (XPS) 55
2.4 Electrode Morphology Characterization 57
2.4.1 Scanning Electron Microscopy (SEM) 57
2.5 Electrochemical Performance of the Electrodes 58
2.5.1 Cell Assembly 58
2.5.2 Galvanostatic Charge 60
2.5.3 Cyclic Voltammetry (CV) 63
2.5.4 Electrochemical Impedance Spectroscopy (EIS) 63
2.5.5 Diffusion Coefficient Determination Method 65
2.5.6 Energy Density Estimation in Battery Pack 67
2.6 Battery Performance Stability 68

3 Battery Cathode with Vertically Aligned Microstructure Fabricated by Directional Ice Templating 70
3.1 Introduction 71
3.2 Results and Discussion 74
3.2.1 Fabrication of Cathodes by DIT 74
3.2.2 Cathode Active Material Particle Surface Properties 76
3.2.3 Electrode Structures 81
3.2.4 Electrochemical Performance 84
3.3 Experimental Section 95
3.3.1 Fabrication of Electrodes 95
3.3.2 Characterization 95
3.3.3 Electrochemical Testing 96
3.4 Conclusion 97

4 Fabrication Method of Directional Microstructure for High Energy Density, High Power Battery Cathodes 99
4.1 Introduction 100
4.2 Results and Discussion 103
4.2.1 Fabrication of Electrodes by Scaled-up Directional Ice Templating (DIT) 103
4.2.2 Compositional Uniformity of Scaled-up DIT Electrodes 105
4.2.3 Electrode Microstructure 107
4.2.4 Electrochemical Performance 109
4.3 Experimental Section 119
4.3.1 Characterization 119
4.3.2 Electrochemical Testing 119
4.4 Conclusion 120

5 Ultra-thick Graphite Anode Vertical Microstructure by Directional Ice Templating 122
5.1 Introduction 123
5.2 Results and Discussion 126
5.2.1 Fabrication of Graphite Anode by DIT 126
5.2.2 Electrode Structure 128
5.2.3 Electrochemical Performance 131
5.3 Experimental Section 136
5.3.1 Fabrication of Electrodes 136

5.3.2 Characterization....137
5.3.3 Electrochemical Testing....137
5.4 Conclusion....138

6 Conclusion....139
6.1 Conclusion....140
6.2 Future Work....142

Reference....144

List of Figures

Figure 1.1 Global average surface temperature anomalies relative to the 20th-century average.[3] 18
Figure 1.2 Energy Density Characteristics of Battery Technologies. (a) Comparison of energy density among various battery chemistries (Lead-acid, Ni-Cd, Ni-MH, and Li-ion). (b) Trend of lithium-ion battery energy density improvements from 2008 to 2020.[4][5] 20
Figure 1.3 Schematic illustration of the working principle of a lithium-ion battery during charge and discharge cycles, showing lithium-ion diffusion between electrodes and electron flow through the external circuit. 24
Figure 1.4 Schematic representation of the conventional slurry coating electrode fabrication process: slurry mixing, slurry coating, drying and calendaring. 27
Figure 1.5 (a)Schematics of the DIT apparatus, and the DIT processing steps showing (b) initial electrode slurry state, (c) slurry during directional freezing, and (d) fully frozen slurry. 30
Figure 1.6 Modified water phase diagram showing freeze-drying pathway[52] 32
Figure 1.7 Alternative microstructure-controlled method for electrode fabrication (a)magnetic alignment method, (b)3-D print method and (c)laser structuring method. 34
Figure 2.1 Synthesis route for NMC811 44
Figure 2.2 Crystal structure of graphite[82] 46
Figure 2.3 Schematic of TEM imaging 53
Figure 2.4 Schematic of ToF-SIMS, where a pulsed primary ion beam sputters the sample surface and produces secondary ions that are separated by mass-to-charge ratio for chemical mapping. 54
Figure 2.5 Schematic of XPS 55
Figure 2.6 Schematic illustration of SEM operation 57
Figure 2.7 The schematic of coin cell in this study 59
Figure 2.8 Schematic of the five-point sampling locations used for compositional uniformity analysis of the scaled-up DIT cathode sheet. 69
Figure 3.1 TEM images of the NMC811 particle surface and their corresponding magnified images for (a,d) pristine particle in ambient room conditions without deliberate water exposure; (b,e) particle immersed in water for 30 minutes; (c,f) particle immersed in water for 7 days. 77
Figure 3.2 XPS C1s spectra of (a) three types of NMC811 particles superimposed together showing the content of Li_2CO_3; and the fitted spectra of (b) pristine particle in ambient room conditions without deliberate water exposure (NMC-ambient conditions); (c) particle immersed in water for 30 minutes (NMC-30 min); (d) particle immersed in water for 7 days (NMC-7 days). 78
Figure 3.3 ToF-SIMS depth profile showing the formation of Li_2CO_3 and LiOH from the surface of NMC811 particles to the inside particles under three conditions: NMC-ambient conditions; NMC-30 min; and NMC-7 days. (a) ToF-SIMS depth profiles showing the intensity of OH^- and CO_3^{2-} as a function of sputtering depth, (b) ToF-SIMS depth profile of Li^+. 79

Figure 3.4 CV curves of DIT-C electrode at a scan rate of 0.1 mV s^{-1} 80
Figure 3.5 Top view SEM image (after ion milling to reveal the inside microstructure) of DIT-C electrode. The freeze direction was towards out of the page, a cellular structure emerged wherein all active material particles were interconnected in the conductive network of the electrode. 82
Figure 3.6 Cross-sectional SEM images of (a–b) SC electrodes; (c–d) DIT electrodes made with a dilute slurry (30:70, DIT-D); and (e–f) DIT electrodes made with a concentrated slurry (40:60, DIT-C). Blue arrows in (c) and (e) mark the freezing direction used in the DIT process. 83
Figure 3.7 Galvanostatic charge and discharge profiles showing (a) areal capacities at 0.1 C; (b) gravimetric capacities at 0.1 C; (c) areal capacities at 0.4 C; (d) gravimetric capacities at 0.4 C. (e) reversible areal capacity of electrodes at different C rates. (f) Equivalent circuit and fitted Nyquist plots for comparison between DIT-C and SC cathodes. 86
Figure 3.8 CV curves of (a) SC cathode and (b) DIT-C cathode, at scan rates of 0.1, 0.2, and 0.5 mV s^{-1}. 87
Figure 3.9 Fitting slop of (a) SC cathode and (b) DIT-C cathode from the normalized peak current of the CV curves. 87
Figure 3.10 Long cycling test of DIT-C, DIT-D and SC electrodes at 2.8 mA cm^{-2} for DIT-C, DIT-D and 1.5 mA cm^{-2} for SC. 88
Figure 3.11 Galvanostatic (dis)charge curves for DIT-D and SC electrodes at 0.1 C. 89
Figure 3.12 Galvanostatic (dis)charge curves for DIT-D and SC electrodes at 0.4 C. 90
Figure 3.13 Reversible gravimetric capacity of the DIT-C and SC electrodes from 0.1 C to 2 C. 90
Figure 3.14 Reversible areal capacity of DIT-D and SC electrodes at different C rates. 91
Figure 3.15 (a)A cross section schematic diagram of SC and DIT-C pouch cell configurations with the same total volume and (b) the volume ratio of components in SC and DIT-C pouch cells. 94
Figure 4.1 Schematics of (a) the directional-ice-templating (DIT) scaled-up apparatus; and (b) the DIT process. 104
Figure 4.2 TGA curves from five representative points across the scaled-up DIT electrode sheet. 107
Figure 4.3 (a) Photo of free-standing NMC811 electrode sheet fabricated by the scaled-up DIT method. Scanning electron microscopy (SEM) images of (b) DIT electrode top surface and (c) its magnified view; (d) DIT electrode bottom surface and (e,f) its magnified views. 107
Figure 4.4 Cross-sectional SEM images of the as-fabricated scaled-up DIT electrode and under subsequent varying degrees of calendering. 109
Figure 4.5 Galvanostatic (dis)charge curves of the scaled-up DIT NMC811 electrodes under varying calendering degrees at 0.1 C, showing (a) gravimetric capacities; and (b) areal capacities. Rate capability of the same electrodes, showing (a) gravimetric capacities; and (d) volumetric capacities. 110

Figure 4.6 Galvanostatic (dis)charge curves of the scaled-up DIT NMC811 electrodes under varying calendering levels at (a,b) 0.2 and (c,d) 0.5 C, showing gravimetric and areal capacities. 112
Figure 4.7 Rate capability of the DIT NMC811 electrodes under varying calendering levels, showing areal capacities..... 112
Figure 4.8 Cyclic voltammograms at 0.05 mV s^{-1}, 0.10 mV s^{-1}, 0.15 mV s^{-1} for (a) 30% calendered DIT electrode; and (c) 0% calendered DIT electrode. Fitted linear relations of the peak current in both anodic and cathodic scans against the square root of scan rate for (b) 30% calendered DIT electrode; and (d) 0% calendered DIT electrode. 114
Figure 4.9 (a) Nyquist plots of the DIT NMC811 electrodes at different calendering levels and the conventional slurry coated electrode of the same materials at a frequency range from 1 MHz to 0.01 Hz, all at the pristine state; and (b) magnified high frequency region of the Nyquist plots. The inset of (b) is the equivalent circuit model that was used for fitting the Nyquist plots. 116
Figure 4.10 Long-term cycling performance of DIT NMC811 electrodes under varying calendering levels at 0.2 C (current density = 2.8 mA cm^{-2}) over 100 cycles. 117
Figure 5.1 (a)Schematics of DIT apparatus for anode, and (b)-(d) cross section of the anode slurry during freezing and freeze-drying procedure..... 126
Figure 5.2 SEM images of the top surface and the magnification views of (a)-(c) SC graphite anode and (d)-(f) DIT graphite anode 128
Figure 5.3 SEM images of the cross section and the magnification views of (a)-(c) SC graphite anode and (d)-(f) DIT graphite anode 130
Figure 5.4 Comparative C-rate Performance and Charge–Discharge Profiles of FD(DIT) and SC Graphite Anodes 131
Figure 5.5 (a)Nyquist plots for comparison between DIT graphite anode and SC graphite anode and (b)-(c) linear fitting of real part Re(Z) of the impedance of SC and DIT anode. 133
Figure 5.6 Long cycling results of DIT electrode and SC electrode 135

List of Tables

Table 3.1 Summary of gravimetric and volumetric energy densities of the cathodes in battery pouch cell configurations. 93
Table 3.2 Details of thickness of each component in pouch cell configurations. 94
Table 3.3 Thickness Distribution of Components in DIT-C vs. SC Cell Stacks 94
Table 4.1 Fitting resistances of the Nyquist plots of the DIT NMC811 electrodes under different calendering levels and the slurry coated electrode of the same materials as a reference using the equivalent circuit model. 116
Table 4.2 Properties and gravimetric and volumetric energy densities of scaled-up A4 pouch cells containing DIT NMC811 cathodes under varying calendering levels and conventional slurry coated electrodes of the same materials for comparison estimated by the CAMS model. 118

Abbreviations

Abbreviation	Description
DIT	Directional Ice Templating
DIT-D	Directional Ice Templating – Dilute
DIT-C	Directional Ice Templating – Concentrated
SC	Slurry Coating
NMC811	$LiNi_{0.8}Mn_{0.1}Co_{0.1}O_2$
LIB	Lithium-ion Battery
EV	Electric Vehicle
ABS	Acrylonitrile Butadiene Styrene
ULEZ	Ultra Low Emission Zone
PVDF	Polyvinylidene Fluoride
NMP	N-Methyl-2-pyrrolidone
SBR	Styrene–Butadiene Rubber
CMC	Carboxymethyl Cellulose
SEI	Solid Electrolyte Interphase
DI water	Deionised Water
TEM	Transmission Electron Microscopy
HRTEM	High-Resolution Transmission Electron Microscopy
ToF-SIMS	Time-of-Flight Secondary Ion Mass Spectrometry
XPS	X-ray Photoelectron Spectroscopy
SEM	Scanning Electron Microscopy
PECS	Precision Etching and Coating System (ion milling)
CV	Cyclic Voltammetry
EIS	Electrochemical Impedance Spectroscopy
TGA	Thermogravimetric Analysis
EC/EMC	Ethylene Carbonate and Ethyl Methyl Carbonate

Chapter 1

1 Introduction

1.1 Why Lithium-ion Battery as Energy Storage Solution

Energy has played a pivotal role in the advancement of human civilization and continues to be essential for modern daily life. Since approximately 200,000 BC, when early humans were first recorded to harness fire for warmth and cooking[1], the pursuit of more efficient and cleaner energy sources has remained a constant endeavour. In 1690, coal began to replace wood as a dominant energy source in Europe, marking a shift toward fossil fuel dependency. Later, in 1885, the introduction of petrol by Karl Benz for use in motorcars led to its widespread adoption across the globe. While these conventional energy sources have undoubtedly facilitated technological progress and improved quality of life, they have also contributed significantly to environmental degradation. Global warming is now widely recognized as a critical issue[2], giving rise to numerous environmental problems such as rising global temperatures, sea-level rise and ecological disruption (Figure 1.1). In Figure 1.1, blue bars represent years with temperatures below the 20th-century average, while red bars indicate years with temperatures above the average. Notably, the global average surface temperature has shown a marked increase since 1880, with the rate of warming accelerating significantly in recent decades.

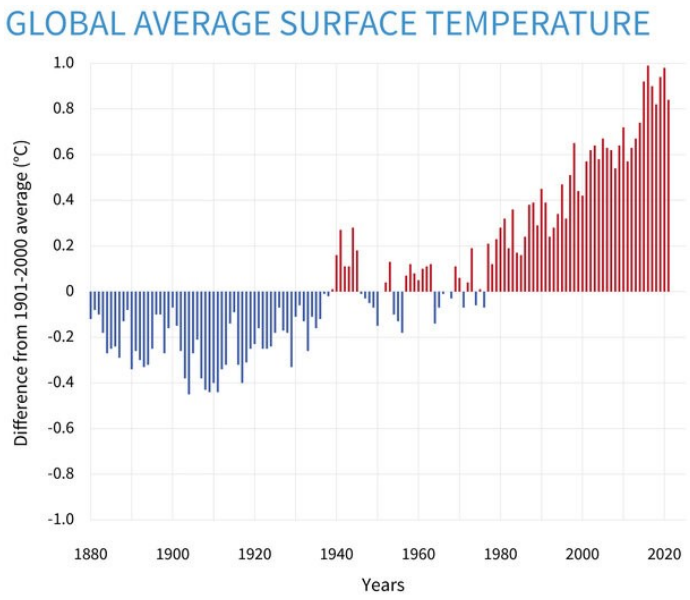


Figure 1.1 Global average surface temperature anomalies relative to the 20th-century average.[3]

Although conventional energy sources are not solely responsible for environmental issues, the urgent need to transition toward sustainable and cleaner alternatives is widely acknowledged. To reduce dependence on fossil fuels, significant efforts have been made to develop renewable energy sources such as solar, wind, and hydropower. However, the intermittent nature of these energy sources highlights the critical importance of efficient energy storage systems. Among various technologies, lithium-ion batteries (LIBs) have emerged as one of the most promising solutions for storing energy generated from renewable sources. Due to extensive research and development by the scientific community, the LIB industry has seen substantial advancements and has become increasingly mature and commercially viable.

The LIB has taken place the dominated position because of its widespread application in consumer electronics, electric mobility, stationary energy storage. In consumer electronics, like smart phones laptops and more wearable devices, the LIBs are ideal in this space due to their compact size, light weight, and long battery life. Electric mobility is currently the fastest-growing sector for LIBs, driven by the global push toward carbon neutrality and emission-free transportation. Several major cities around the world have implemented ambitious policies to accelerate the adoption of electric vehicles (EVs) and reduce their dependence on fossil fuels. For example, Oslo, Norway aims to become the world's first fossil fuel–free city by 2030. The city is electrifying all public transport, including buses, taxis, and ferries. Starting in 2024, all taxis in Oslo are required to be zero-emission. Currently, over 80% of new cars sold in the city are electric, supported by generous incentives and an extensive charging infrastructure. In London, United Kingdom, the government has set a target to achieve net-zero emissions by 2030. The introduction of the Ultra Low Emission Zone (ULEZ) discourages the use of older, more polluting vehicles. All new black cabs must be either electric or hybrid, and there are plans to ensure all new cars and vans are zero-emission by 2030. London's zero-emission bus fleet has grown significantly, from just 30 in 2016 to more than 2,000 today. Shenzhen, China

stands out as the first city in the world to fully electrify its public bus fleet, which includes over 16,000 electric buses. Additionally, all taxis in the city were converted to electric by 2020, showcasing a comprehensive approach to clean urban transportation. In the United States, Los Angeles has set a goal for 100% of its municipal vehicle fleet to be zero-emission by 2035. As part of its "Green New Deal," the city is electrifying its buses, garbage trucks, and other public service vehicles. Significant investments have also been made in EV charging infrastructure, with a focus on providing access in underserved communities.

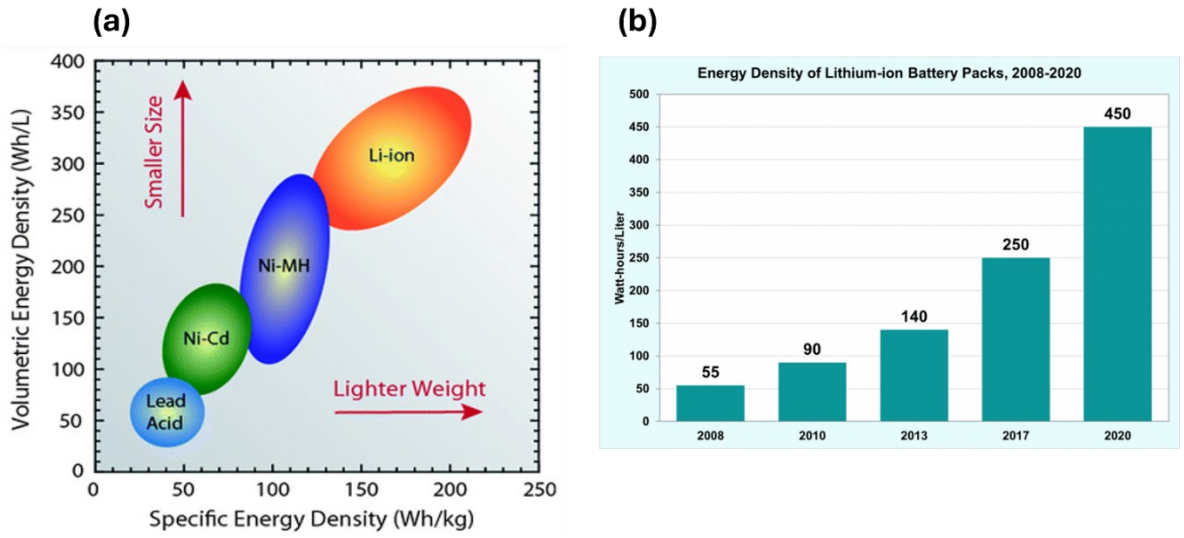


Figure 1.2 Energy Density Characteristics of Battery Technologies. (a) Comparison of energy density among various battery chemistries (Lead-acid, Ni-Cd, Ni-MH, and Li-ion). (b) Trend of lithium-ion battery energy density improvements from 2008 to 2020.[4][5]

In the field of stationary energy storage, LIBs play a crucial role due to five key attributes: high energy density, high efficiency, long cycle life and scalability and modularity. The high energy density of LIBs enables compact energy storage solutions, which is particularly beneficial for residential applications with space constraints, such as wall-mounted battery systems (e.g., Tesla Powerwall[6]). Their high efficiency enhances the overall energy utilization and economic viability of storage systems by minimizing energy losses during charge and discharge cycles. Furthermore, the extended cycle life of LIBs reduces the frequency of battery replacement, thereby lowering maintenance requirements and long-term operational costs[7]. Their rapid response capability makes them well-suited for applications

such as grid balancing, frequency regulation and peak shaving, where immediate energy delivery is essential[8]. Finally, the inherent scalability and modularity of LIB systems allow for flexible deployment, enabling the design of storage configurations that can be easily adapted to meet specific energy demands at both residential and grid levels[9][10]. Beyond traditional rechargeable systems such as lead–acid, Ni-Cd, Ni-MH, and conventional Li-ion, several emerging battery technologies offer significantly higher specific and volumetric energy densities. Lithium metal batteries, enabled by solid or semi-solid electrolytes, can exceed 400 - 500 $Wh \cdot kg^{-1}$ due to the high capacity of lithium metal anodes. Solid-state batteries further improve safety and enable even higher energy density by pairing lithium metal with high-voltage cathodes. Lithium–sulphur (Li-S) batteries can theoretically reach 500 - 600 $Wh \cdot kg^{-1}$, with exceptionally low material weight. Lithium-air (Li-O_2) systems offer among the highest theoretical energy densities (>1000 $Wh \cdot kg^{-1}$), although they remain at an early research stage. These next-generation chemistries highlight the ongoing push toward lighter, higher-energy storage technologies beyond conventional Li-ion systems.

Overall, in response to the increasing global energy demand and environmental considerations, LIBs remain one of the most widely adopted energy storage technologies[11]. Their favourable characteristics—such as high energy density, long cycle life, and high efficiency—have positioned LIBs at the forefront of energy storage solutions across various applications. Despite existing challenges, including temperature sensitivity and the need for effective thermal management, LIBs continue to receive significant research and industrial attention[12][13]. Ongoing advancements aim to address these limitations and further enhance their performance, safety, and sustainability.

1.2 Background of Lithium-ion battery

1.2.1 Brief History of the Development of Lithium Ion Battery

The first electrochemical artifact that had been discovered in the first century BC was called 'Baghdad Battery'. It is also widely accepted that Luigi Galvani at the University of Bologna made the first electrochemical cell to humanity. In 1866, a French engineer Georges-Lionel Leclanche successfully designed the world's first carbon-zinc and alkaline cell[14]. This kind of battery gained a great success because it was introduced to the field of car ignition and portable tools. However, in the late 1960s, the carbon-zinc battery couldn't meet the requirement because the demand for high-energy density, long-lasting reliable energy in implantable medical devices increased. What's more, the request for high-energy source in military industry was urgent. At that time, researchers realized that the energy density was vital to the performance of a battery. The good news was that lithium-based battery was then invented and widely used in medical industry to relieve the suffering of the patient because the lithium-based battery had a lower weight. In 1970s, a lot of popular electronic devices like watches and toys was bought to the market for people to purchase. Despite the great success in portable electronics devices, the lithium polymer battery couldn't be applied in mass production since the lithium mental was very reactive which may cause significant risks[15]. Thanks to the devotion of John B. Goodenough who invented first lithium-ion cathode ($LiCoO_2$) in 1980, Sony successfully commercialised the lithium-ion battery using a graphite anode in 1991.[16][17]. Nowadays, the most used materials are Lithium cobalt oxide (LCO), lithium nickel manganese cobalt oxide (NMC), lithium nickel cobalt oxide doped with alumina (NCA), lithium manganese oxide (LMO) and lithium iron phosphate (LFP). The global lithium-ion battery market size was valued at 21.3 billion US dollars[18], and this number is estimated to be 113.89 billion US dollars in 2030[19].

1.2.2 The Components and Working Principle of LIBs

After years of development, a LIB consists of several key components: a cathode, an anode, a separator, an electrolyte, and current collectors[20]. The current collectors in lithium-ion batteries are typically aluminium foil for the cathode and copper foil for the anode because each metal is electrochemically stable within the relevant potential window. At the high cathode potentials (3.5 - 4.3 V vs. Li/Li^+), copper would oxidise and dissolve whereas aluminium remains stable. Conversely, at the low anode potential near 0 V vs. Li/Li^+, aluminium would alloy with lithium and lose conductivity while copper remains stable and does not form Li alloys, making it the suitable choice for the anode.

The cathode serves as the positive electrode during discharge. It is the source of lithium ions, which migrate through the electrolyte toward the anode during discharge[21]. An effective cathode should offer high lithium storage capacity and operate at high voltage, typically between 3.0 and 4.3 V depending on the material[22]. Cathode materials are commonly coated on aluminium foil, which is stable under high-voltage conditions[23].

The anode acts as the negative electrode during discharge. It stores lithium ions during charging and releases them during discharge[24]. A good anode should exhibit high reversible capacity and is often made of graphite, silicon-based composites, or lithium titanate[25]. The anode is typically coated on copper foil, which remains stable at low potentials.

The electrolyte provides a medium for lithium-ion transport between the electrodes while blocking electron flow[26]. It must be electrochemically stable within the operating voltage window (0 - 4.3 V), compatible with both electrodes, and have high ionic conductivity[27]. Common electrolytes include liquid electrolytes such as $LiPF_6$ in Ethylene Carbonate and Ethyl Methyl Carbonate (EC/EMC) solvents, solid electrolytes (ceramic or polymer-based), and gel electrolytes (a polymer matrix containing liquid electrolyte)[28][29][30].

Current collectors enable electron transport to and from the external circuit. Aluminium foil is used on the cathode side due to its lightweight nature and corrosion resistance at high voltage. Copper foil is used on the anode side for its excellent conductivity and stability at low potentials. Both aluminium and copper foils should be thin, flexible, and adhere well to the electrode coating[31].

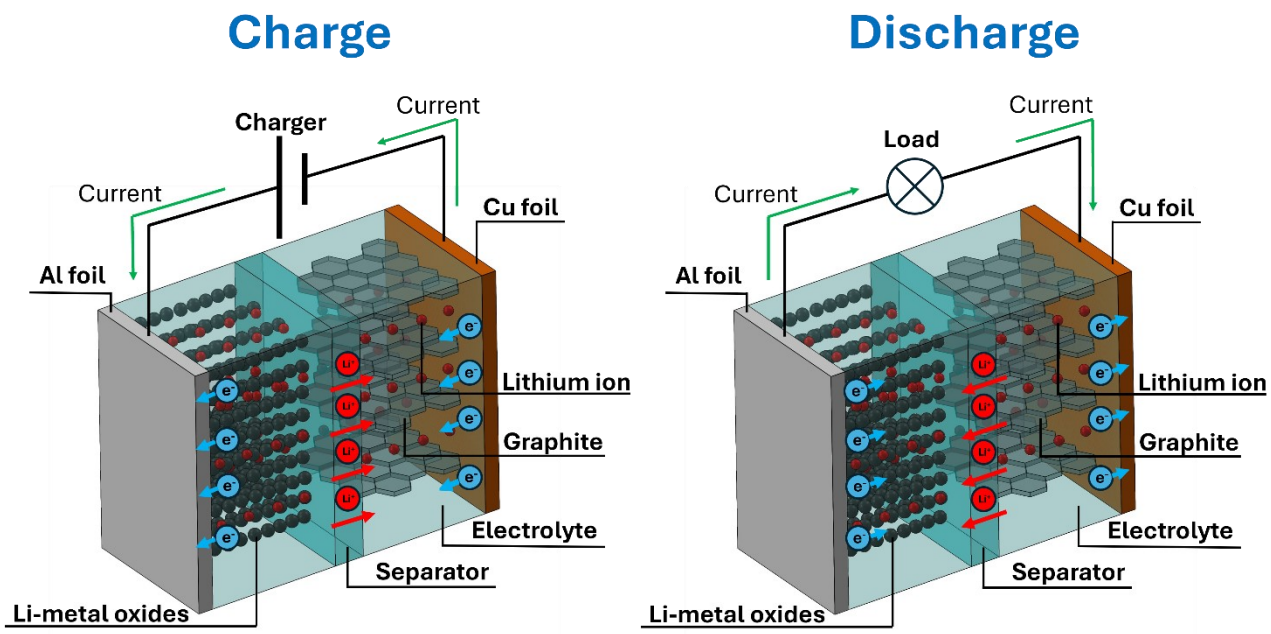


Figure 1.3 Schematic illustration of the working principle of a lithium-ion battery during charge and discharge cycles, showing lithium-ion diffusion between electrodes and electron flow through the external circuit.

During charging, the charger provides current flows for the cathode from the external circuit, while electrons move toward the anode, as illustrated in Figure 1.3. The loss of electrons from the cathode induces the extraction (deintercalation) of lithium ions from the cathode material, leading to a higher lithium-ion concentration on the cathode side[32]. These lithium ions then migrate through the electrolyte, cross the separator, and move toward the anode, where the concentration is lower[33]. At the anode, the incoming electrons provide the necessary negative charge to balance the positive charge of the incoming lithium ions. The anode, typically composed of graphite or lithium metal, accommodates the lithium ions through intercalation

into the graphite layers or alloying with lithium metal[34]. This ion movement is accompanied by electron flow in the same direction through the external circuit.

During discharge, the process reverses. Lithium ions are extracted (deintercalated) from the anode, where their concentration is relatively high, and migrate through the electrolyte toward the cathode, where the lithium-ion concentration is lower. This movement is driven by the concentration gradient and the electrochemical potential difference between the electrodes. Simultaneously, electrons flow from the anode to the cathode through the external circuit, delivering electrical energy to the load. As lithium ions reach the cathode, they are re-inserted (intercalated) into the cathode material and combine with the incoming electrons, restoring charge neutrality. The redistribution of lithium ions from the anode to the cathode continues until the cell reaches its lower voltage limit, indicating that most of the mobile lithium ions have returned to the cathode and the battery is fully discharged[35].

When charge, the reaction in cathode and anode are:

Cathode: $LiNi_{0.8}Mn_{0.1}Co_{0.1}O_2 \rightarrow Li_{1-x}Ni_{0.8}Mn_{0.1}Co_{0.1}O_2 + xLi^+ + xe^-$

Anode: $C_6 + xLi^+ + xe^- \rightarrow Li_xC_6$

When discharge, the reaction in cathode and anode are:

Cathode: $Li_{1-x}Ni_{0.8}Mn_{0.1}Co_{0.1}O_2 + xLi^+ + xe^- \rightarrow LiNi_{0.8}Mn_{0.1}Co_{0.1}O_2$

Anode: $Li_xC_6 \rightarrow C_6 + xLi^+ + xe^-$

1.2.3 The Importance of Electrode Design in Performance

The working principle of LIBs replies on the reversible intercalation and deintercalation of lithium ions between the cathode and anode during charge and discharge[36]. This process was controlled by ion diffusion between electrodes, electrons transportation and interfacial electrochemical reactions[37][38]. These factors are directly related to the electrode structure and composition.

The ionic and electronic pathways in the electrode is one of the most important factors[39]. In LIBs cycling life, hundreds of lithium-ion migrations between electrode requires efficient and continuous ionic pathway within the electrodes. A well-designed electrode structure can minimize tortuosity and optimize both ionic and electronic diffusion, resulting in a lower internal resistance and improving battery C-rate capability[40].

Surface area and interfacial reactions also play important roles in determining LIB performance. Electrodes with high surface area enable more effective interfacial reactions. A larger surface area improves contact between the electrolyte and active materials[41]. As a result, high-surface-area electrodes typically offer better lithium-ion exchange kinetics and higher capacity utilization, especially under high current density during charge and discharge.

Porosity and electrolyte wetting are also critical to performance. Optimized electrode porosity ensures sufficient electrolyte penetration[42]. This is essential for maintaining continuous and stable ion diffusion from the bulk electrolyte to the electrode surface, particularly in thick electrodes. Electrodes that are too dense or poorly wetted can restrict lithium-ion transport and promote irreversible degradation, especially under high mass loading or fast cycling conditions. However, excessive porosity may compromise mechanical integrity and reduce overall energy density.

Electrode thickness is another important design parameter. Increasing electrode thickness allows for higher mass loading of active materials. This directly increases the proportion of active material in the battery and enhances energy density. However, excessively thick electrodes without structural control can cause slow ion diffusion and polarization issues[43]. A well-designed electrode must balance thickness and structural properties to improve energy density while maintaining good cycling performance and long-term stability.

In summary, electrode design during the fabrication process has a significant impact on battery performance, including energy density, rate capability (C-rate performance) and cycling stability.

1.3 Conventional Electrode Fabrication and Limitation

1.3.1 Conventional Electrode Fabrication

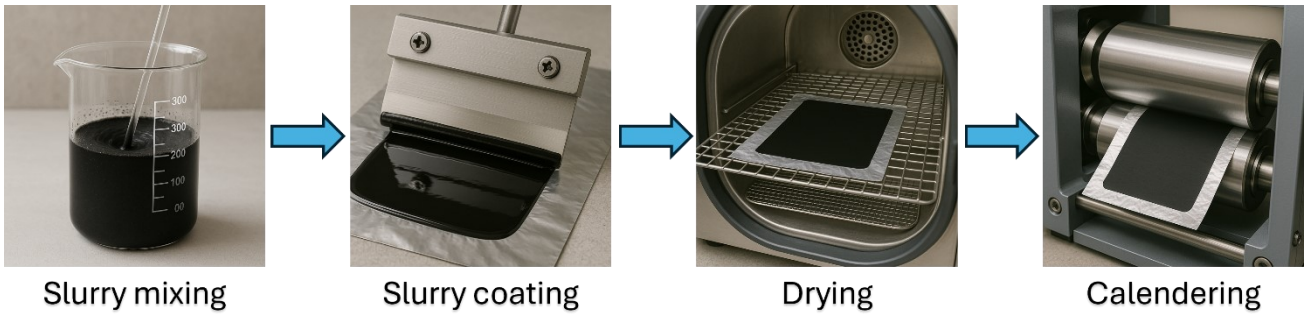


Figure 1.4 Schematic representation of the conventional slurry coating electrode fabrication process: slurry mixing, slurry coating, drying and calendaring.

The conventional electrode fabrication method includes the following steps: material mixing, slurry coating, drying and calendaring.

In the material mixing step, active materials (e.g., NMC811 powder for the cathode or graphite powder for the anode) are combined with conductive additives (e.g., carbon black) and polymer binders. Common binders include Polyvinylidene Fluoride (PVDF) dissolved in N-methyl-2-pyrrolidone (NMP) for cathodes, and Styrene Butadiene Rubber (SBR) with Carboxymethyl Cellulose (CMC) in aqueous solvent for anodes[44]. The goal is to produce a homogeneous slurry with uniformly dispersed particles. Proper mixing is essential to ensure good electrical conductivity and mechanical stability in the final electrode.

Slurry coating step defines the electrode thickness and ensures a uniform coating across the substrate. In this step, the prepared slurry is coated onto a metal current collector (Al foil for cathode and Cu foil for anode) by a doctor blade or slot-die coater.

After slurry coating, the coated foil is first subjected to preliminary drying in an oven at 80 °C for 50 minutes to remove most of the solvent. The partially dried electrode is then transferred

to a vacuum oven and heated at 110 °C for 120 minutes to ensure complete removal of residual solvent and moisture. Inadequate drying may lead to the formation of cracks in the electrode, and the presence of moisture can degrade the electrolyte and trigger undesirable side reactions during cell operation[45].

In the calendaring process, the dried electrode sheet is compressed using heated rollers to reduce its thickness and porosity, while enhancing mechanical strength. This step also improves particle-to-particle contact within the electrode, thereby lowering internal resistance. Additionally, the reduction in electrode volume contributes to an increase in energy density. Under typical calendering pressures, the aluminium current collector undergoes only small elastic deformation, with most of the compression occurring within the porous active-material layer.

Finally, the electrode sheet is cut into the desired shape and size. The electrodes are then assembled into cells together with separators and electrolyte. This step involves component stacking or winding, depending on the cell format, followed by electrolyte filling and cell sealing. All assembly processes must be conducted in a moisture- and oxygen-controlled environment to prevent contamination and degradation of battery components[46].

1.3.2 The Limitation of Conventional Electrode Fabrication

The slurry coating method is widely adopted in both industrial and academic settings for electrode fabrication. However, several limitations remain associated with this approach. Firstly, the conventional slurry coating method faces challenges in producing thick electrodes[47]. Thicker electrodes are desirable because they increase the proportion of active material relative to inactive components such as current collectors and separators, which raises the overall energy density of the cell and the entire battery pack. Thick coatings increase the risk of cracking due to high capillary forces generated during solvent evaporation in the drying process. Secondly, thick electrodes generally exhibit higher porosity and therefore require more

extensive thickness reduction during calendering. However, excessive calendering can increase tortuosity and hinder lithium-ion transport, negatively affecting rate capability and overall electrochemical performance[48]. Achieving a balance between increasing electrode thickness and maintaining optimal ion transport remains a significant challenge. Thirdly, thick electrodes are prone to uniformity issues. As the electrode thickness increases, it becomes more difficult to control particle distribution and coating uniformity, leading to performance variability. Fourthly, concerns arise from limited electrolyte penetration in densely packed electrodes. After drying and calendering, particles become highly compacted, leaving insufficient pore space for electrolyte infiltration. This can result in uneven electrode wetting and reduced electrochemical activity, particularly under high-rate conditions. Finally, there are health and environmental concerns associated with the use of NMP, a common solvent for cathode slurry preparation. NMP is classified as hazardous, posing risks to human health through inhalation or skin absorption[49]. Exposure may cause respiratory irritation, headaches, nausea, and gastrointestinal discomfort. Furthermore, NMP has potential environmental impacts due to its persistence and toxicity to aquatic and soil ecosystems.

1.4 Directional Ice Templating (DIT): a novel electrode fabrication strategy

1.4.1 Process Overview and Principles

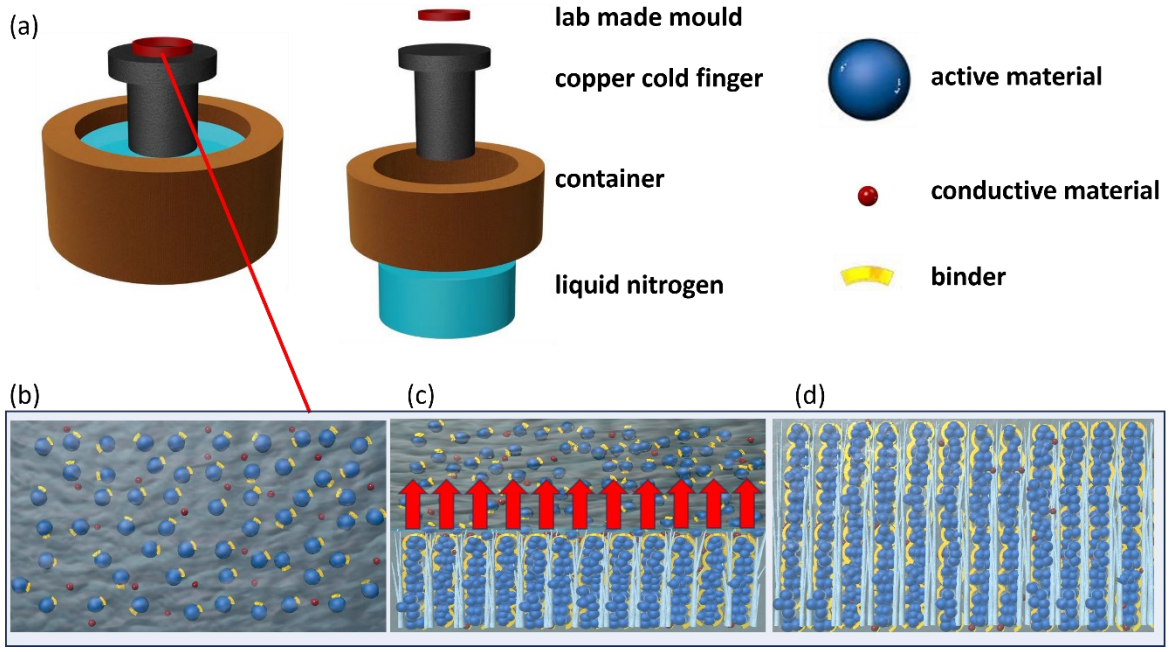


Figure 1.5 (a)Schematics of the DIT apparatus, and the DIT processing steps showing (b) initial electrode slurry state, (c) slurry during directional freezing, and (d) fully frozen slurry.

In this work, we show a novel, rapid bottom-up approach of DIT to make NMC811 cathodes with high thickness (660-1100 µm) and control the anisotropic cathode microstructure containing alternating vertically aligned lamellae of electrode materials (10-15 µm in width) and pore arrays (6-12 µm in diameter) through the electrode thickness to provide fast dual electron and lithium ion transport pathways and thus to improve the battery energy density and C-rate capability at the cell-stack level simultaneously[50].

The process of DIT includes slurry mixing, slurry frozen, slurry freeze drying and demould for assembly. In the slurry mixing process, active materials along with conductive materials and binders are mixed with aqueous solvent because we want to eliminate the hazard solvent NMP. In this work, the electrode formulation was transferred from an NMP-based slurry to a water-based system by replacing NMP with deionised water as the solvent and substituting the PVDF binder with a water-soluble binder. This allowed the slurry to be dispersed, mixed and cast

entirely in an aqueous phase. In the slurry frozen process, a lab made electrode freeze set was applied. The lab-made apparatus of the DIT method integrates three parts including a lab-designed round acrylonitrile butadiene styrene (ABS) mould for the electrode slurry, a copper cold finger, and a container of liquid nitrogen [51]. The ABS mould was placed on top of the copper cold finger platform which was placed in the container (Figure 1.5a). The electrode active material particles and electrical conductivity enhancer carbon particles with polymeric binder were first homogeneously mixed in the electrode slurry (Figure 1.5b). During the DIT process, the electrode slurry experienced rapid vertical directional freezing from underneath. Ice crystals started to nucleate at the supercooling interface on the copper cold finger. Ice columns started to grow vertically from the bottom along the freezing temperature gradient. As these dendrites grew along the vertical freezing direction, the ice dendrites exerted pressure on the NMC811 and carbon particles, displacing them into the columns in-between the ice dendrites and in situ shaping them into the desired microstructure (Figure 1.5c). As heat was efficiently taken away from the electrode slurry through conduction, ice columns continued to grow vertically through the entire electrode thickness (Figure 1.5d). During this process, the water transitions from Status 1 (liquid) to Status 2 (solid) as depicted in Figure 1.6.

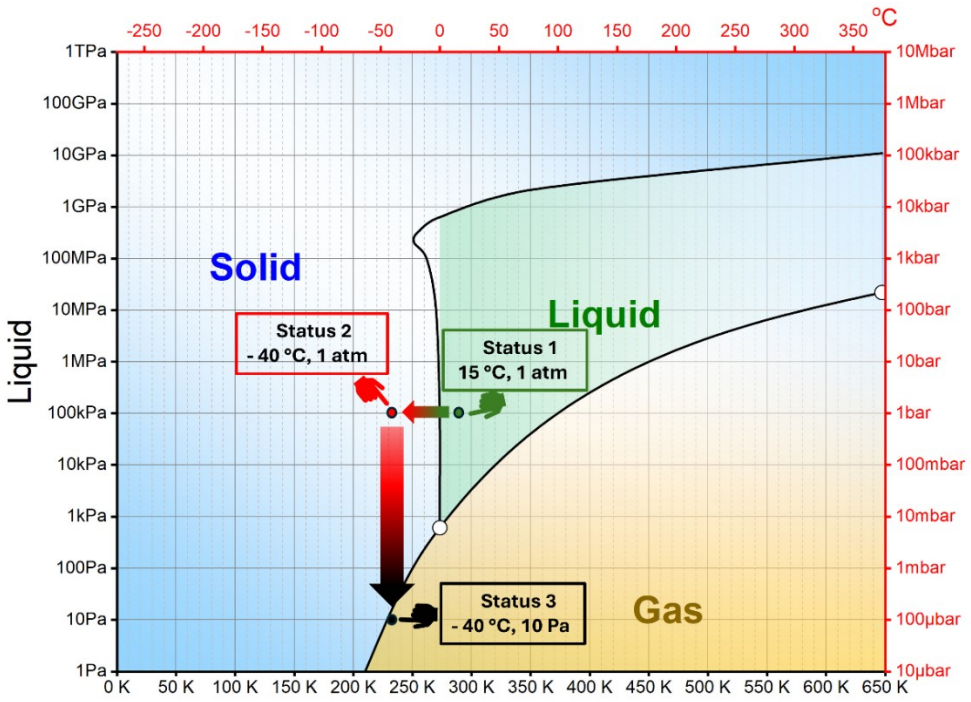


Figure 1.6 Modified water phase diagram showing freeze-drying pathway[52]

After the electrode reached full solidity, the ice columns were directly sublimed from solid to vapour through freeze-drying to preserve the formed microstructure. The freeze-drying process is carried out at -40 °C and 10 Pa (Status 3 in Figure 1.6). The critical step of ice sublimation prevented the ice dendrites from transitioning back into a liquid phase before ice removal, and hence, preventing the effect of shrinkage that usually takes place in conventional SC electrodes due to the capillary force during conventional evaporation of solvent from liquid to vapour through heating[53]. Thus, we were able to make ultra-thick (660-1100 µm) DIT cathodes without cracking to increase mass loading of the electrodes while maintaining the designed internal microstructure.

1.4.2 Prior Research of DIT in Battery Electrode

DIT has been widely explored as a method to create vertically aligned, low-tortuosity porous structures in a variety of functional materials, including ceramics, polymers and carbon-based electrodes. Previous studies have demonstrated that DIT can significantly enhance ion transport pathways, improve electrolyte infusion and enable the fabrication of thick electrodes with

reduced diffusion limitations. The previous work was done by other researcher in our group, and they have developed the DIT method for other materials of $LiCoO_2$ [54] and $LiFePO_4$ [55] and directional freezing and polymerisation (DFP) method for NMC811 in polymer-based solid batteries [56]. Different active material size and surface characteristics resulted in slightly different pore channel diameter and tortuosity, but the vertically aligned microstructure was maintained.

A similar method was applied to graphite anode fabrication by the Ruhul Amin group[57]. However, several important aspects were not addressed in previous studies. Firstly, the reported methods are often time-consuming and require extensive material modification. In some cases, the preparation of rare or customized materials involved more than 20 hours of processing, limiting their practicality and scalability. Secondly, there has been limited discussion on the side reactions associated with high-nickel cathode materials in aqueous systems. NMC811, as a Ni-rich cathode material, is less stable compared to lower-Ni compositions and is more reactive with aqueous solvents[58]. It is therefore crucial to understand and control the side reactions that may occur during exposure to water-based processing. Thirdly, most previous studies were conducted at lab scale, without addressing issues related to production efficiency or scalability. Moreover, the calendaring process, as a critical step for reducing electrode thickness that could increase electrode density and ultimately improving energy density was not included in earlier work. In this study, we present a comprehensive investigation to address these gaps. We evaluate the time efficiency of the fabrication process, examine the side reactions of Ni-rich NMC811 in aqueous environments, and demonstrate the scalability of the approach. Additionally, we optimize the calendaring conditions for DIT electrodes to achieve controlled porosity and enhanced energy density.

1.4.3 Limitations of Alternative Microstructure-controlled Methods for Electrode Fabrication

Compared with other methods such as magnetic alignment[59], 3D printing, and laser structuring, the DIT approach offers unique advantages in controlling electrode microstructure.

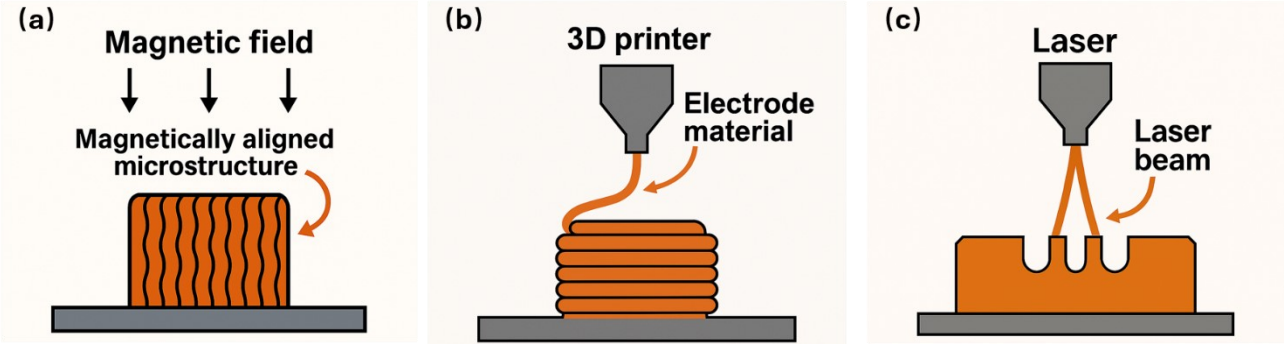


Figure 1.7 Alternative microstructure-controlled method for electrode fabrication (a)magnetic alignment method, (b)3-D print method and (c)laser structuring method.

The magnetic alignment technique involves magnetically responsive particles, such as functionalized conductive additives into the electrode slurry[60]. During the coating or drying process, an external magnetic field is applied to align these particles along a preferred orientation, typically in the through-thickness direction. This alignment creates anisotropic pathways that enhance both electronic and ionic conductivity. The goal is to reduce tortuosity and facilitate more efficient ion transport. However, only magnetically responsive materials or additives can be aligned, which limits the choice of active materials. Furthermore, achieving uniform alignment over large-area electrodes requires strong and homogeneous magnetic fields, which are challenging to implement and scale in industrial settings.

3D printing fabricates electrodes layer by layer using specially formulated inks composed of active materials, conductive additives, and binders[61]. The geometry, porosity, and internal architecture of the printed electrodes can be controlled by adjusting the printing path, ink rheology, and deposition parameters. This method allows for the creation of customized microstructures that enhance ion diffusion and structural integrity. However, the layer-by-layer printing process is time-consuming and currently unsuitable for high-throughput

manufacturing. Additionally, fine structural features may compromise mechanical strength or introduce defects that negatively impact long-term cycling stability.

Laser structuring uses focused laser beams to ablate or pattern the surface of dried electrodes. This technique creates vertical microchannels or pores that reduce tortuosity and facilitate improved lithium-ion transport and electrolyte infiltration[62]. Laser structuring can be applied as a post-treatment to conventional electrodes without altering their bulk composition. However, the high energy of laser pulses may induce localized thermal damage to active materials, conductive agents, and binders. The ablation process also leads to material loss, reducing the active mass and overall energy density of the electrode. Moreover, laser systems are expensive, require high energy input, and pose scalability challenges for large-area electrode processing.

1.4.4 Advantages and Challenge of DIT Method

The DIT method offers several significant advantages for electrode fabrication. First, scalability is a key strength of the DIT approach. The method is compatible with scalable slurry coating techniques and requires only the application of a directional freezing temperature gradient, which from the bottom of the substrate to rapidly form in situ ice templates. This makes it suitable for both laboratory research and potential industrial implementation.

Second, DIT demonstrates strong versatility. It can be applied to a wide range of cathode and anode materials, including NMC-based compounds, graphite, silicon composites, and lithium titanate. This broad applicability allows for integration into various lithium-ion battery chemistries without the need for major modifications to the material system.

Third, the method offers excellent structural controllability. The diameter and alignment of the pore channels, as well as the overall porosity, can be tuned by adjusting the solid content of the slurry and the freezing rate. This allows for precise tailoring of electrode architecture to optimize ionic transport pathways while maintaining mechanical integrity.

Despite these advantages, there are two major challenges associated with applying DIT to NMC811 cathode fabrication. The first is aqueous processing, as Ni-rich layered oxides like NMC811 are prone to surface degradation and lithium leaching when exposed to water[58]. Managing the stability of NMC811 in an aqueous environment is critical to preserving electrochemical performance[63]. The second challenge is porosity control. While DIT naturally produces porous structures favourable for ion transport, excessive porosity reduces volumetric energy density. Therefore, balancing pore architecture with densification strategies—such as calendaring—is essential for maximizing energy storage performance.

In this study, we address both critical issues. We investigate the interfacial stability of NMC811 in aqueous slurries and implement calendaring procedures to reduce porosity in DIT-structured electrodes, ultimately improving their energy density while retaining directional microstructural advantages.

1.5 Research Objectives and Scope

The primary objective of this research is to enhance the electrochemical performance of lithium-ion battery electrodes by controlling their microstructure through an advanced manufacturing method. Specifically, the study aims to improve fast (dis)charging capability, increase energy density, and extend cycling life by reducing tortuosity and promoting efficient ion and electron transport within the electrode.

To achieve this, a DIT technique was employed to fabricate vertically aligned porous electrodes. This method offers several advantages over other microstructure engineering strategies such as magnetic alignment, 3D printing, and laser structuring. DIT enables the formation of vertically aligned pore channels, which significantly reduce tortuosity and facilitate more uniform electrolyte penetration and ion diffusion.

The DIT method was applied to both the cathode NMC811 and the graphite anode. While the application of DIT to graphite electrodes was relatively straightforward—given that water-based slurries are already standard in conventional fabrication—the water-to-solid ratio was optimized to achieve the desired porosity and structural alignment. In contrast, adapting DIT for NMC811 cathodes presented a greater challenge. Traditional NMC811 cathode processing uses NMP as a solvent, which is incompatible with freeze-casting. To enable DIT and improve environmental sustainability, the solvent system was switched to water. However, this introduced concerns regarding water-induced surface degradation of Ni-rich NMC811 particles. Therefore, additional studies were conducted to evaluate the extent of water-induced surface reactions and to control the exposure time during aqueous processing.

The scope of this study includes the fabrication, morphological characterization, and electrochemical evaluation of electrodes produced via the DIT method in half-cell configuration. Electrode microstructure was assessed in terms of pore alignment and porosity, while electrochemical testing—including rate performance and cycling stability—was performed to evaluate practical performance benefits. An estimation of energy density at the battery pack level was also carried out.

Furthermore, the research explores the scalability of the DIT approach. A modified experimental setup was developed to demonstrate the feasibility of scaling up this method from laboratory scale toward more practical production levels.

1.6 Motivation of the Thesis

The overarching motivation of this thesis is to address the increasing demand for high energy density and fast charging lithium-ion batteries by developing electrode microstructure that overcome the transport and manufacturing limitations of conventional slurry coating designs. As applications such as electric vehicles and large-scale energy storage continue to require electrodes with higher mass loading and improved electrochemical performance. New

fabrication methods are needed to reduce ion-transport resistance, maintain mechanical stability and enable scalable production. DIT provides a promising approach for creating vertically aligned, low-tortuosity structures that can enhance electrochemical performance. This thesis therefore investigates the potential of the DIT method applied to widely used commercial active materials as an advanced electrode manufacturing approach, with the aim of increasing cell-level energy density while remaining compatible with practical battery production processes.

1.6.1 Motivation of Chapter 3

A central challenge in lithium-ion battery manufacturing is achieving high energy density while maintaining efficient ion transport, particularly in thick electrodes. This chapter investigates the feasibility of applying the DIT method to fabricate thick NMC811 cathodes with vertically aligned microstructures. While DIT has demonstrated promise in microstructure control, its application to Ni-rich layered oxide cathodes remains unexplored due to the inherent instability of NMC811 in aqueous environments. Replacing NMP with water as the processing solvent not only supports environmental sustainability but also introduces the critical need to manage side reactions between NMC811 and water. Therefore, two key objectives guided this study: (i) to optimize the water-to-solid ratio in the electrode slurry to achieve both structural integrity and desirable microstructural features such as low tortuosity and similar porosity with conventional slurry coating electrode, and (ii) to evaluate the chemical compatibility of NMC811 with water during slurry preparation. This small-scale fabrication study establishes the process window for achieving free-standing, ultra-thick NMC811 electrodes (>1000 μm) with enhanced energy density, while also confirming that controlled water exposure introduces minimal surface degradation. These foundational results provide the basis for further scaling and performance evaluation in subsequent chapters.

1.6.2 Motivation of Chapter 4

Following the successful small-scale fabrication of NMC811 electrodes using the DIT method, the next critical step was to evaluate the scalability of this technique for practical application. Unlike the initial lab-scale process, which used a 6 mm diameter mould and liquid nitrogen as a cooling medium, this chapter focuses on adapting the DIT method to a larger-format electrode using a flat plate system and a Peltier cooling module. This approach eliminates the reliance on extremely low temperature freezing, making the process more suitable for industrial manufacturing. The primary objective was to demonstrate that the DIT method can be scaled to fabricate large-area electrodes while maintaining the vertical pore alignment and structural integrity achieved at small scale. In addition to proving the feasibility of DIT method in large scale electrode fabrication, this chapter also investigates the effect of calendering—a widely adopted post-processing step in battery manufacturing—on the DIT-derived microstructure. Since calendering can densify the electrode and improve volumetric energy density, understanding its impact on the vertically aligned pore structure was essential. Through optimization of the calendering rate and evaluation of structural uniformity via thermogravimetric analysis (TGA), this chapter establishes that the DIT method can be successfully scaled without compromising the desired microstructure or performance benefits, thereby supporting its industrial relevance.

1.6.3 Motivation of Chapter 5

While DIT method has demonstrated significant benefits for cathode structuring, its applicability to other electrode materials remains a key question. Graphite anodes, as the dominant commercial anode material in lithium-ion batteries, present a critical test case for evaluating the generalizability of the DIT approach. This chapter aims to demonstrate that DIT can be effectively applied to graphite electrodes, despite the material's distinct particle shape, size distribution, and packing characteristics. Importantly, the study utilizes fully commercial graphite materials without any lab-scale modification, highlighting the practical relevance of

the method. By carefully optimizing slurry composition and processing parameters, this work shows that vertically aligned, free-standing, and ultra-thick graphite anodes can be fabricated using DIT. This not only confirms the technique's adaptability but also establishes a foundation for future full-cell configurations in which both the cathode and anode employ DIT-based architectures. Ultimately, this chapter reinforces the scalability, material versatility, and industrial potential of the DIT fabrication route.

1.6.4 Research Significance and Potential Impact

This study presents a significant advancement in lithium-ion battery electrode manufacturing by introducing and validating the DIT method as a scalable, versatile, and cost-effective approach for fabricating thick, vertically aligned electrodes. In contrast to conventional slurry coating techniques, which produce electrodes with randomly distributed particles and disordered pore networks, the DIT method enables controlled microstructural engineering. It generates vertically aligned pore channels that reduce electrode tortuosity, thereby enhancing lithium-ion transport and overall electrochemical performance.

When compared to other advanced structuring methods—such as 3D printing, magnetic alignment, and laser structuring—DIT offers several key advantages. It is inherently more scalable and adaptable to a wide range of materials, requires lower capital investment, and is operationally simpler, making it highly attractive for industrial implementation. Furthermore, the use of water-based processing, as demonstrated in this work, eliminates the need for hazardous solvents like NMP, aligning with growing demands for environmentally sustainable manufacturing.

The ability to fabricate ultra-thick electrodes with vertically aligned architectures has substantial implications for next-generation energy storage systems. Thick electrodes reduce the relative proportion of inactive components such as current collectors, separators, spacers, and casing materials in a battery cell or pack, thereby increasing the overall energy density.

Vertically aligned pore structures shorten lithium-ion diffusion pathways and mitigate the transport limitations typically observed in thick electrodes. These improvements enable faster charging and discharging, reduce degradation associated with high tortuosity, and support better performance under high-power operating conditions[64].

The impact of this work extends beyond the laboratory scale. By demonstrating the feasibility of large-area electrode fabrication using a Peltier-cooled DIT setup, this research provides a foundation for scaling the technique toward industrial production. Structural uniformity was confirmed through thermal and morphological analysis, and although further optimization may be needed for full commercial adoption, all critical process parameters are technically achievable with current manufacturing technologies.

The advancements presented here are relevant for both EV applications and grid-scale energy storage. In EVs, increased energy density translates to greater driving range and improved power performance. In stationary storage, the ability to store more energy per unit volume supports higher capacity installations within space-constrained environments. As the demand for high-performance, sustainable, and cost-effective batteries continues to grow, this work positions the DIT method as a promising pathway toward next-generation electrode design and manufacturing.

Chapter 2

2 Materials and Methods

2.1 Materials Applied

2.1.1 Cathode Materials

In this thesis, electrodes fabricated via the conventional slurry coating (SC) method were used as a benchmark for comparison[65]. All materials employed in the SC electrodes are commercially available and have been extensively developed and validated in both industrial and academic settings[66].

NMC811 was selected as the active cathode material due to its layered α-$NaFeO_2$-type crystal structure, which is known to facilitate two-dimensional lithium-ion diffusion pathways[67]. The high nickel content contributes significantly to the specific capacity by increasing the proportion of redox-active Ni^{2+}/Ni^{4+} centres, resulting in a high theoretical capacity of approximately 200 mAh g^{-1}[68]. The partial substitution of nickel with manganese and cobalt further enhances the structural and electrochemical properties of the material[69]. The manganese improves structural stability, while cobalt enhances electronic conductivity[70]. As a result, NMC811 offers a great combination of high energy density, cost-effectiveness, and relatively stable cycling performance compared to lower-nickel-content NMC variants. The most common synthesis route for NMC811 involves a coprecipitation method followed by high-temperature solid-state reaction and shown in the Figure 2.1[71]. In this process, transition metal salts are first coprecipitated to form a $Ni_{0.8}Mn_{0.1}Co_{0.1}(OH)_2$ precursor, which is then mixed with lithium hydroxide (LiOH) and calcined at approximately 800 °C. This yields the final NMC811 product with a layered α-$NaFeO_2$-type crystal structure. It should be noted that this thesis does not involve any study related to the synthesis of active materials. Instead, commercially available NMC811 powder was used throughout all experiments.

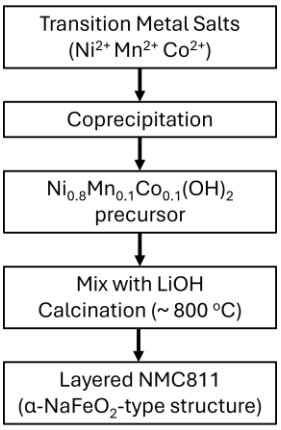


Figure 2.1 Synthesis route for NMC811

Carbon black powder was used as the conductive additive to enhance the electronic conductivity of the electrode by forming interconnected conductive pathways between the NMC811 particles[72]. This material was chosen due to its high electrical conductivity, which ensures efficient electron transport during charge and discharge processes. In addition, its small particle size and high specific surface area allow uniform dispersion within the electrode matrix and enable the formation of a conductive network[73]. Carbon black is also chemically stable and cost-effective, making it a widely used additive in lithium-ion battery electrodes. PVDF powder was employed as the binder to hold together the active material and conductive additive particles and to ensure their strong adhesion to the current collector (typically aluminium foil on cathode side). PVDF was selected due to its excellent chemical stability against electrolyte components and resistance to oxidative degradation at high operating voltages[74]. It also exhibits good thermal stability, maintaining mechanical integrity during cycling, and adheres effectively to both the current collector and active material surface. Moreover, PVDF can easily dissolve in NMP, which helps to create a uniform and stable slurry. NMP was used as the solvent to dissolve the PVDF binder and to provide appropriate fluidity for the SC process. It offers excellent solvency for PVDF, evaporates cleanly during the drying stage, and enables good slurry stability and viscosity control[75]. However, due to its toxicity and environmental hazards, there is a growing demand to develop water-based alternatives that are more

sustainable and compatible with electrode materials such as NMC811[76]. The slurry was coated onto aluminium foil because aluminium offers excellent electrical conductivity, enabling efficient collection and transport of electrons between the external circuit and the active cathode material during charge and discharge[77]. Additionally, aluminium exhibits good electrochemical stability, remaining stable under the high operating potentials typical of cathode materials such as NMC811[78].

In the DIT method, a water-based electrode formulation was used to enable environmentally friendly processing and to produce free-standing cathode structures without the use of a current collector foil. The choice of DI water as the solvent was also driven by the specific requirements of the DIT process, which involves directional freezing followed by freeze-drying of the solvent. Water has a relatively high freezing point, which facilitates controlled solidification during the freezing process. It also could form well-oriented ice crystals, which is essential for generating vertically aligned pore structures in the electrode. NMC811 was again selected as the active material due to its high specific capacity and layered crystal structure that facilitates efficient lithium-ion transport. And for fair comparison with SC electrode. Carbon black was included as the conductive additive to form continuous electron-conducting pathways throughout the electrode. Its high conductivity, fine particle size, and large surface area enable effective network formation and uniform dispersion within the slurry. A dual binder system consisting of SBR and CMC was used to provide both mechanical strength and particle adhesion[79]. CMC, a water-soluble polysaccharide, acts as a dispersant and enhances slurry stability, while SBR, a flexible latex polymer, contributes elasticity and cohesion to the dried electrode structure. This binder combination is well-suited for aqueous processing and enables the formation of mechanically robust, binder-rich domains that maintain structural integrity during ice templating and subsequent drying. DI water served as the solvent to dissolve the CMC binder and facilitate homogeneous mixing of all components.

Its non-toxic and sustainable nature makes it an attractive alternative to organic solvents like NMP, particularly in large-scale electrode manufacturing.

2.1.2 Anode Materials

For the anode materials, the SC method used a common and widely adopted composition. Graphite powder was used as the active material. A dual binder system of SBR and CMC was applied, with deionized water as the solvent[80]. Copper foil served as the current collector. This composition is well-suited for aqueous processing and provides good electrochemical performance. In the DIT method, the same slurry composition was used. The only difference was that the resulting electrode was free-standing, so copper foil was not included.

Graphite was selected as the anode active material due to several key advantages that make it highly compatible with high-energy-density cathode materials such as NMC811. Graphite possesses a layered structure composed of hexagonally arranged sp^2-bonded carbon atoms (shown in Figure 2.2), which facilitates the reversible intercalation and deintercalation of lithium ions. Upon full lithiation, it forms a stable compound (LiC_6) with a theoretical specific capacity of 372 mAh g^{-1}[81]. Its low operating potential, typically in the range of 0.1–0.2 V vs. Li/Li^+, complements the high working voltage of NMC811 (3.0 - 4.3 V), thereby contributing to a high overall cell voltage and energy density.

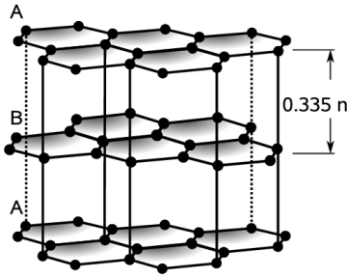


Figure 2.2 Crystal structure of graphite[82]

In addition to its electrochemical properties, graphite exhibits excellent structural stability during extended cycling[83]. This stability allows the electrode to maintain mechanical

integrity and deliver long-term durability, both of which are critical for practical battery applications. It is also widely available, cost-effective, and compatible with large-scale industrial electrode manufacturing processes. Furthermore, the electrochemical behaviour of graphite is well understood. This makes it a reliable and commercially mature anode material.

Alternative anode materials such as silicon and lithium metal have also been explored in combination with high-capacity cathodes like NMC811 due to their significantly higher theoretical capacities which were approximately 4200 mAh g^{-1} for silicon and 3860 mAh g^{-1} for lithium metal[84][85]. However, their widespread application is limited by significant technical challenges. Silicon suffers from severe volume expansion (~300%) during lithiation, leading to mechanical degradation and unstable solid electrolyte interphase (SEI) formation[86]. Lithium metal offers the highest possible capacity among anode materials. However, its use is associated with dendrite formation and serious safety risks, including potential short-circuiting. As a result, graphite remains the most practical and widely adopted anode material for use in commercial NMC811-based lithium-ion batteries.

2.1.3 Other Materials

In the DIT electrode fabrication process, the freezing step was carried out using liquid nitrogen as the cold source, which was stored in a Dewar container. Liquid nitrogen was chosen for the initial stage of the study due to its suitability for small-scale experiments. During this phase, many trials were required to optimize the slurry composition and processing parameters. The use of liquid nitrogen provided a rapid and consistent cooling environment, making it an effective and practical cold source for early-stage DIT optimization.

In the small-scale implementation of the DIT method, a customized experimental setup was designed and constructed in the laboratory, with fabrication support from the departmental engineering workshop. Copper was selected as the material for the cold finger due to its excellent thermal conductivity, which ensures efficient and uniform heat transfer during the

freezing process[87]. To accommodate the directional freezing configuration, a mould made of ABS was designed using SolidWorks software and subsequently 3D printed in the lab. This ABS mould was designed to meet the dimensional and structural requirements of the DIT process. Additionally, a dedicated container (referred to as the liquid nitrogen pool) was developed to hold the liquid nitrogen during the freezing stage. This container was also designed in-lab and fabricated in the engineering workshop. High-density polyurethane was chosen as the construction material for its good thermal insulation properties and mechanical strength, ensuring safe handling and stable thermal performance during freezing.

In the scaled-up DIT setup, an aluminium plate was used to support the slurry. Its excellent thermal conductivity promoted uniform heat distribution during the freezing process. At this stage, liquid nitrogen was no longer suitable as a cold source due to its rapid evaporation, handling complexity, and limited scalability for larger setups. Instead, a ceramic Peltier module was employed for heat dissipation, offering compact size, and the ability to generate a stable temperature gradient necessary for directional freezing. To enhance the cooling efficiency of the Peltier system, a water-cooling setup was integrated into the design. The system circulated chilled water to extract heat continuously from the hot side of the Peltier module. The water temperature was maintained at a low level by adding ice cubes, ensuring stable cooling performance during the freezing process.

2.2 Electrode Fabrication Procedure

This thesis includes the fabrication of 5 types of electrodes: a conventional SC cathode, a small-scale DIT cathode, a scale-up DIT cathode, a conventional SC graphite anode, and a small-scale DIT graphite anode. While these electrodes share general fabrication principles, each follows a slightly different protocol to suit its specific structure and material requirements.

2.2.1 Conventional Slurry Coating Cathode

A conventional SC cathode was fabricated to provide a benchmark for comparison with DIT cathodes. The slurry was prepared by mixing 90 wt% NMC811 powder (Xiamen TOB, China), 5 wt% carbon black (Sigma Aldrich, UK), and 5 wt% PVDF binder (Sigma Aldrich, UK). NMP solvent (Sigma Aldrich, UK) was used as the solvent in a 1:1 weight ratio with the solid mixture. All components were weighed using a precision balance (Ohaus PR124/E, Switzerland; resolution: 0.001 g). The mixture was homogenized in a planetary mixer (ARE-250, Thinky, Japan) at 2000 rpm for 20 minutes. The resulting uniform slurry was coated onto 16 μm-thick aluminium foil using a doctor blade coater (AFA-V, Shanghai Modern Instruments, China) at a coating speed of 5 mm s^{-1}. The coated foil was initially dried in a conventional oven at 80 °C for 50 minutes, followed by vacuum drying at 110 °C for 120 minutes (Vacuum Oven, MTI Corporation, USA). Circular electrodes with a diameter of 16 mm were punched from the dried sheets using a disc cutter. Their mass and thickness were then measured using a precision balance and micrometre (DML Ltd., UK), respectively.

2.2.2 Small-scale DIT Cathode

The small-scale DIT cathode was fabricated through a four-step process: mixing, freezing, freeze-drying, and demoulding. In the mixing step, a precision balance (Ohaus Model PR124/E, Switzerland) was used to measure the dry components in the following weight ratios: 90 wt% NMC811 powder (Xiamen TOB Company, China), 5 wt% carbon black (Sigma Aldrich, United Kingdom), 3 wt% SBR binder (Cambridge Energy Solution Ltd.), and 2 wt% CMC. Deionised water was then added as the solvent. Two formulations were prepared based on the weight ratio of solid powders to DI water: 30:70 for a dilute slurry and 40:60 for a more concentrated one. The resulting mixture was transferred into a container and homogenized using a planetary mixer (ARE-250, Thinky Company, Japan). The slurry was mixed at 500 rpm for 5 minutes for pre-dispersion, followed by 2,000 rpm for 15 minutes to achieve a uniform dispersion of particles. The slurry was then poured into a custom-designed mould (6 mm diameter, 1 mm

depth) and placed on a cold finger cooled by liquid nitrogen to induce directional freezing for 15 minutes. Following freezing, the mould containing the solidified slurry was transferred into a 150 mL freeze-drying flask (Labconco Company, United Kingdom), which was connected to a benchtop freeze dryer (Labconco Company, United Kingdom). The freeze-drying process was carried out at – 40 °C under a vacuum of 0.1 mbar. After drying, the DIT cathode was demoulded, and its mass and thickness were measured using a precision balance and a micrometre, respectively.

2.2.3 Scale-up DIT Cathode

The scaled-up DIT cathode fabrication followed a five-step process: mixing, freezing, freeze-drying, demoulding, and calendaring. The electrode slurry was prepared using 90 wt% NMC811 powder (Xiamen TOB Company, China), 5 wt% carbon black (Sigma Aldrich, United Kingdom), 3 wt% SBR binder (Cambridge Energy Solution Ltd.), and 2 wt% CMC, with deionised water as the solvent. A 1:1 weight ratio between the powder mixture and DI water was used. The slurry was initially mixed at 500 rpm for 5 minutes, followed by intensive mixing at 2000 rpm for 20 minutes using a planetary mixer (ARE-250, Thinky Company, Japan) to ensure uniform dispersion. The well-mixed slurry was then cast onto an aluminium plate positioned on top of four Peltier cooling modules (TEC1-12706, Diymore Company, China). The casting process was controlled by a doctor blade coater (AFA-V, Shanghai Modern Instruments, China) with a coating speed of 5 mm s^{-1}. The Peltier modules were powered by a regulated DC power supply (Universal Regulated Switching Power Supply, inShareplus Company, China). To maintain effective thermal management, a heat dissipation plate was attached to the hot side of the Peltier modules, connected to a lab-designed water-cooling system using chilled water circulation. After complete freezing, the aluminium plate with the frozen slurry was transferred into a benchtop freeze dryer (Labconco Company, United Kingdom). Freeze-drying was performed at – 40 °C and 0.1 mbar. Upon completion of freeze-

drying, the system temperature was raised to 15 °C under vacuum to allow the aluminium plate to gradually return to room temperature. Following this, one group of electrode sheets was demoulded and cut into the required shape for cell assembly, while comparison groups were subjected to a calendaring process using a rolling press machine (Xiamen TOB Company, China), with thickness carefully controlled. Finally, all electrodes were weighed using a precision balance and their thicknesses measured using a micrometre.

2.2.4 Conventional Slurry Coating Graphite Anode

The conventional SC graphite anode was fabricated in this study to enable a fair comparison with the DIT-structured graphite anode. The electrode slurry was prepared using 95 wt% graphite powder (American Elements Company, United States), 3 wt% SBR binder (Cambridge Energy Solution Ltd.), and 2 wt% CMC, with deionised water added as the solvent. A 1:1 weight ratio between the dry powder mixture and DI water was maintained. All components were weighed using a precision balance (Ohaus Model PR124/E, Switzerland) with a resolution of 0.001 g. The slurry was mixed in a suitable container using a planetary mixer (ARE-250, Thinky Company, Japan) at 2000 rpm for 20 minutes to achieve uniform dispersion. The homogenized slurry was then uniformly coated onto flat copper foil (10 μm thickness) using a doctor blade coater (AFA-V, Shanghai Modern Instruments, China) at a coating speed of 5 mm s^{-1}. Following coating, the electrode sheet underwent preliminary drying in a convection oven at 80 °C for 50 minutes. Subsequently, the partially dried electrode was transferred to a vacuum oven (MTI Corporation, United Stated) and further dried at 100 °C for 120 minutes to remove residual moisture and ensure complete drying. Finally, circular electrodes with a diameter of 16 mm were punched from the dried electrode sheet using a disc cutter. The mass and thickness of each electrode were measured using a precision balance and a micrometre, respectively.

2.2.5 Small-scale DIT Graphite Anode

The small-scale DIT graphite anode was fabricated through a sequence of four steps: mixing, freezing, freeze-drying, and demoulding. In the mixing step, a precision balance (Ohaus Model PR124/E, Switzerland) was used to weigh the dry components in the following ratios: 95 wt% graphite powder (American Elements Company, United States), 3 wt% SBR binder (Cambridge Energy Solution Ltd.), and 2 wt% CMC. Deionised water was added as the solvent at a weight ratio of 26:74 (powder mixture to DI water). The mixture was transferred into a mixing container and homogenized using a planetary mixer (ARE-250, Thinky Company, Japan) at a rotation speed of 2000 rpm for 20 minutes to ensure uniform dispersion of all components. The resulting slurry was then poured into a lab-designed mould (6 mm diameter, 1 mm depth) and placed onto a cold finger cooled with liquid nitrogen to induce directional freezing for 15 minutes. After freezing, the mould containing the solidified slurry was transferred into a 150 mL freeze-drying flask (Labconco Company, United Kingdom), which was connected to a benchtop freeze dryer (Labconco Company, United Kingdom). The freeze-drying process was carried out at – 40 °C and 0.1 mbar. Upon completion of freeze-drying, the DIT graphite anode was carefully demoulded. The mass and thickness of the resulting electrode were measured using a precision balance and a micrometre, respectively.

2.3 NMC811 Water Exposure Study Characterization

To investigate the effect of water exposure on the surface chemistry and structural stability of Ni-rich layered cathode materials, three groups of NMC811 powder were prepared: pristine NMC811 with no contact with water (pristine control), NMC811 exposed to deionised water for 30 minutes under the same conditions used in the DIT electrode fabrication process, and NMC811 exposed to deionised water for seven days (degradation reference). These groups were chosen to represent the extremes of no exposure and prolonged exposure, with the 30-

minute condition directly corresponding to the aqueous slurry preparation time in this study. Characterisation was carried out using three complementary surface-sensitive techniques: transmission electron microscopy (TEM) to observe morphological changes and surface coatings, time-of-flight secondary ion mass spectrometry (ToF-SIMS) to detect carbonate (CO_3^{2-}) and hydroxide (OH^-) species, and X-ray photoelectron spectroscopy (XPS) to quantify carbonate formation via C 1s peak analysis.

2.3.1 Transmission Electron Microscope (TEM)

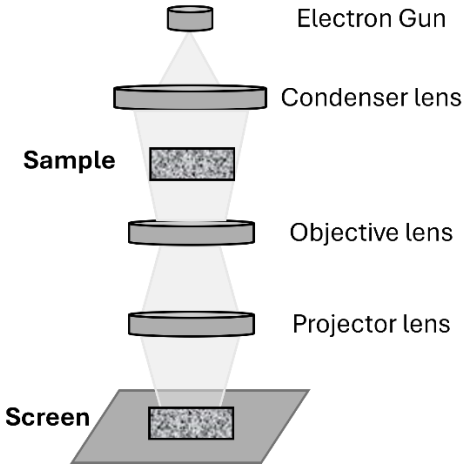


Figure 2.3 Schematic of TEM imaging

TEM is a high-resolution imaging technique in which a beam of high-energy electrons is transmitted through an ultrathin specimen to reveal nanoscale structural details[88]. Electrons emitted from an electron gun are accelerated and focused into a fine probe by electromagnetic lenses. The focused beam interacts with the sample, and the transmitted electrons are used to form an image. Variations in electron scattering and absorption generate contrast, enabling visualisation of morphology, crystallographic features and surface coatings[89]. The resulting image is recorded using a fluorescent screen or a high-sensitivity digital camera.

TEM analysis was performed using a JEOL STEM-2100Plus microscope. Three groups of NMC811 powder with different water exposure durations (pristine, 30 minutes, and 7 days) were prepared. Each sample was dispersed in acetone within a glass vial and sonicated to

produce a uniform particle suspension. A small volume of the suspension was transferred onto copper TEM grids using a glass pipette and allowed to dry under ambient conditions prior to imaging. Previous studies have shown that water-induced side reactions on NMC811 surfaces can result in the formation of a lithium carbonate (Li_2CO_3) layer[90]. In this work, TEM imaging focused on identifying such surface layers, quantifying their thickness, and correlating these observations with water exposure time. It was expected that pristine NMC811 would show no carbonate coating, the 30-minute exposure group would display only a thin layer, and the 7-day exposure group would exhibit a substantially thicker coating.

2.3.2 Time-of-Flight Secondary Ion Mass Spectrometry (ToF-SIMS)

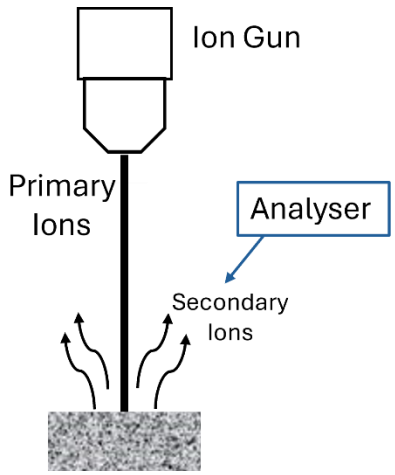


Figure 2.4 Schematic of ToF-SIMS, where a pulsed primary ion beam sputters the sample surface and produces secondary ions that are separated by mass-to-charge ratio for chemical mapping.

ToF-SIMS is a surface-sensitive analytical technique that provides elemental and molecular information from the outermost atomic layers of a material. A pulsed primary ion beam bombards the sample surface, sputtering secondary ions. These ions are accelerated into a time-of-flight analyser, where their mass-to-charge ratios are determined based on the time required to reach the detector[91]. ToF-SIMS offers high sensitivity and spatial resolution, making it

ideal for detecting surface-bound species such as carbonate (CO_3^{2-}) and hydroxide (OH^-) ions formed by aqueous reactions.

ToF-SIMS measurements were carried out using a combined IONTOF TOF.SIMS5–Qtac100 LEIS instrument equipped with a 25 keV bismuth liquid metal ion gun (LMIG) operated in both positive and negative ion modes. High-current bunch mode (beam current: 1 pA) was applied to obtain high-resolution mass spectra. For depth profiling, a 1 keV cesium (90 nA) dual source column (DSC) ion beam was used to progressively remove surface material. The sputtering rate was calibrated to 0.125 nm s^{-1}, providing a linear relationship between sputter time and depth. An interlaced sputtering mode was employed, scanning a 100 × 100 μm^2 field at a resolution of 128 × 128 pixels. This configuration enabled the acquisition of depth-resolved chemical maps, revealing the distribution of CO_3^{2-} and OH^- species within the surface layers. Powder samples from each water exposure group (pristine, 30 minutes, and 7 days) were mounted on conductive carbon tape to ensure stable electrical grounding during analysis.

2.3.3 X-ray Photoelectron Spectroscopy (XPS)

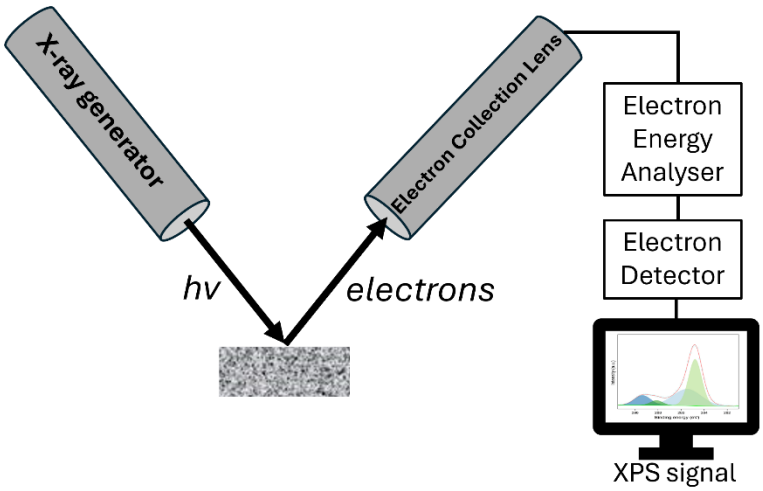


Figure 2.5 Schematic of XPS

XPS is a quantitative surface analysis technique that determines the elemental composition and chemical states of atoms within the top few nanometres of a material. Under monochromatic X-ray irradiation, photoelectrons are emitted from the sample surface[92]. Their kinetic energy

is measured, and the corresponding binding energy is calculated to identify specific elements and bonding environments. High-resolution spectra allow differentiation of species such as carbonate carbon (~290 eV in the C 1s region) from hydrocarbon or organic carbon, providing direct evidence of carbonate layer formation[93].

XPS measurements were performed using a Thermo Scientific K-Alpha spectrometer equipped with a monochromatic Al Kα X-ray source (1486.6 eV). Survey scans were acquired to identify all surface elements, followed by high-resolution scans of the C 1s, O 1s, and Ni 2p regions. The high-resolution C 1s spectra were collected using a pass energy of 35 eV to ensure accurate peak separation. Powder samples from the pristine, 30-minute, and 7-day water exposure groups were mounted on double-sided carbon tape, and charge compensation was applied during acquisition to minimise charging effects. Data processing and peak deconvolution were performed using Thermo Avantage software, with particular attention given to the carbonate carbon peak (~290 eV) associated with CO_3^{2-} species. Based on the hypothesis for this study, the pristine sample was expected to exhibit the lowest carbonate peak intensity, followed by the 30-minute exposure sample with a slightly higher intensity, and the 7-day exposure sample displaying the highest carbonate peak due to prolonged water-induced surface reactions.

2.4 Electrode Morphology Characterization

2.4.1 Scanning Electron Microscopy (SEM)

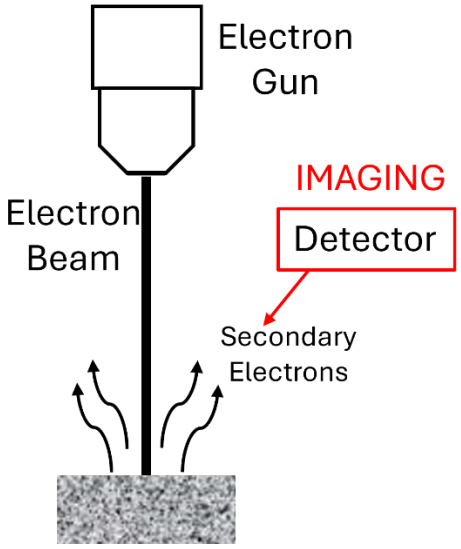


Figure 2.6 Schematic illustration of SEM operation

SEM is a high-resolution imaging technique that uses a focused beam of electrons to scan the sample surface, generating images based on the interaction between the electrons and the specimen. Secondary electrons emitted from the sample surface provide detailed topographical information, while backscattered electrons offer compositional contrast[94]. SEM enables the visualisation of surface features, particle distribution, and cross-sectional morphology at the microscale, making it an essential tool for analysing electrode microstructure.

SEM analysis was performed using a Zeiss Sigma 300 scanning electron microscope to examine the morphology of five electrode types fabricated in this study: a conventional SC cathode, a small-scale DIT cathode, a scale-up DIT cathode, a conventional SC graphite anode, and a small-scale DIT graphite anode. Since this thesis focuses on enhancing electrode performance through the DIT method, SEM was a critical technique for evaluating microstructural differences between DIT-fabricated and conventionally fabricated electrodes. Both the top and bottom surfaces, as well as the cross-sections of the electrodes, were imaged to assess particle alignment, porosity, and microstructural uniformity. For cross-sectional imaging, the samples were prepared using a fully automated argon ion milling system (PECS

II, Gatan) operated at 8 keV for 5 hours to produce uniformly flat cross-sections, ensuring high-quality imaging and accurate structural analysis. Porosity analysis was carried out by processing cross-sectional SEM images in ImageJ software, where segmentation techniques were applied to distinguish pore space from solid material and calculate the overall porosity. It was anticipated that electrodes fabricated using the DIT method would exhibit vertically aligned pore channels and a more uniform internal architecture, whereas conventionally SC electrodes would display a random particle distribution and higher tortuosity.

2.5 Electrochemical Performance of the Electrodes

2.5.1 Cell Assembly

To evaluate the electrochemical performance of the fabricated electrodes, all electrodes were assembled into CR2032-type coin cells in a half-cell configuration. In this configuration, the working electrode (fabricated cathode or anode) was paired with a lithium metal counter electrode to enable characterization. The coin cell consisted of several key components: the working electrode under investigation; a lithium metal disc serving as both the counter and reference electrode, providing a stable potential and acting as the lithium source/sink; CR2032 stainless steel coin cell cases (Xiamen TOB Company, China) that encased and sealed the internal components, ensuring mechanical integrity and preventing electrolyte leakage, with the top cap contacting the counter electrode and the bottom cap contacting the working electrode; two stainless steel spacers (15.8 mm diameter × 0.5 mm thickness, Xiamen TOB Company, China) positioned on each electrode side to ensure uniform pressure distribution and secure electrical contact; a flexible wave spring ring (Xiamen TOB Company, China) to maintain constant pressure on the cell stack; a Celgard 2500 monolayer polypropylene (PP) membrane battery separator (Cambridge Energy Solutions Ltd., United Kingdom) to prevent short-circuiting while allowing ionic conduction; and a liquid electrolyte of 1 M $LiPF_6$ in a mixture of ethylene carbonate (EC) and ethyl methyl carbonate (EMC) (Sigma-Aldrich, United

Kingdom) to facilitate ionic transport during charge and discharge. This configuration ensured a controlled and reproducible environment for electrochemical testing.



Figure 2.7 The schematic of coin cell in this study

All electrode assemblies were conducted in an argon-filled glovebox, in which the concentrations of O_2 and H_2O were strictly maintained below 0.1 ppm. This inert atmosphere was essential to prevent undesirable side reactions between the highly reactive liquid electrolyte and lithium metal. Such reactions could produce lithium hydroxide or lithium carbonate, which impair electrochemical performance and compromise cell stability[95]. The punched electrode discs were first transferred into the glovebox via the antechamber to avoid atmospheric exposure. Assembly followed the sequence illustrated in Figure 2.7, the bottom stainless-steel case was placed first, followed by a stainless-steel spacer, the working electrode under investigation, the Celgard 2500 monolayer polypropylene (PP) separator, the lithium metal counter/reference electrode, a second stainless steel spacer, and the wave spring. The separator was wetted on both sides with 1 M $LiPF_6$ in ethylene carbonate (EC) and ethyl methyl carbonate (EMC) electrolyte (Sigma-Aldrich, United Kingdom), with the total volume

precisely controlled at 80 μL per cell to ensure optimal ionic conductivity while minimising excess electrolyte. The stacked components were sealed using a pressure-adjustable electric crimper (MSK-160E, MTI Corporation, United States) at an applied pressure of 0.8 ton, ensuring a hermetic seal and consistent internal compression. Following assembly, the cells were stored within the glovebox for a minimum of 8 hours prior to electrochemical testing, allowing sufficient time for complete electrolyte wetting and equilibration within the porous electrode structure.

2.5.2 Galvanostatic Charge

Galvanostatic charge means charging or discharge a battery using a constant current. During galvanostatic (dis)charging, the current (I) is held as a constant value and the voltage (V) is monitored as a function of time[96]. Galvanostatic charge-discharge cycling is also called constant current cycling, which is widely used to evaluate capacity, C-rate performance and cycling stability[97].

As the current(I) was input and the software will record the Voltage(V) and the Time(t). The absolute capacity (Q) was calculated as:

$$Q = \int_{t_0}^{t_1} I \, dt$$

With the constant current: $Q = I(t_1 - t_0)$

To calculate capacity (Q) in mAh:

$$Q_{mAh} = \frac{I[mA] \times \Delta t[h]}{1}$$

In this thesis, the capacity of each battery was normalized as specific capacity (mAh g^{-1}), areal capacity (mAh cm^{-2}) and volumetric capacity (mAh cm^{-3}) to make comparison. The normalization equation was followed as:

Specific capacity (mAh g^{-1}): $\frac{Q_{mAh}}{m_{active}}$

Areal capacity (mAh cm^{-2}): $\frac{Q_{mAh}}{A_{electrode}}$

Volumetric capacity (mAh cm^{-3}): $\frac{Q_{mAh}}{V_{electrode}}$

Where, m_{active} refers to the mass of active materials in an electrode, $A_{electrode}$ refers to the areal size of an electrode, $V_{electrode}$ refers to the volume of an electrode.

The coulombic efficiency was calculated as:

$$CE(\%) = \frac{Q_{discharge}}{Q_{charge}} \times 100$$

The absolute energy(E) in Joule was calculated as:

$$E = \int_{t_0}^{t_1} V(t)\ I\ dt$$

With the constant current: $E = I \int V(t) dt$ (J)

To calculate the energy in Wh and mWh, the equation are as follow:

$$E_{Wh} = \int V(t)\ I[A]\ dt[h]$$

$$E_{mWh} = \int V(t)\ I[mA]\ dt[h]$$

The galvanostatic charge–discharge method was employed in this study to evaluate the C-rate capability, coulombic efficiency, and long-term cycling stability of the electrodes. All the experiments were conducted on a battery cycler (Arbin BT-G-48, ARBIN instruments, United Stated).

C-rate capability characterization was conducted to evaluate the ability of the fabricated electrodes to deliver capacity under different charge–discharge rates[98]. The C-rate is defined as the applied current normalized to the theoretical or nominal capacity of the electrode, such that 1C corresponds to a full charge or discharge within 1 hour (0.5C means full charge or discharge within 2 hours). For the C-rate capability measurements, the applied current was adjusted to correspond to different C-rates, with the C-rate value calculated according to the following equation:

$$Current(I) = Crate * (m_{active} * Q_{theroretical})$$

The test procedure involved cycling the coin cells at a low reference rate (0.1C) to determine the baseline capacity, followed by sequential galvanostatic charge–discharge cycles at progressively higher rates, with the voltage range fixed between 3.0 and 4.3 V for NMC811 cathode (0.01- 1.5 V for graphite anode)[99].

In this study, coulombic efficiency was calculated from galvanostatic charge–discharge profiles obtained at a constant current within the defined voltage window (3.0 - 4.3 V vs. Li/Li^+ for cathodes; 0.01 - 1.5 V vs. Li/Li^+ for anodes). Coulombic efficiency is a key electrochemical parameter used to assess the reversibility of lithium-ion insertion and extraction in a cell. During the initial cycles, the coulombic efficiency reflects the irreversible lithium loss associated with SEI formation and other surface reactions with the electrolyte. Over prolonged cycling, monitoring the coulombic efficiency provides insight into the extent of irreversible lithium-ion loss.

Long-cycling stability testing was performed to assess the capacity retention and structural integrity of the fabricated electrodes over extended charge–discharge cycling. This test evaluates the electrode's ability to maintain performance under repeated lithium-ion insertion and extraction, which is critical for practical applications requiring prolonged service life. In

this study, the assembled CR2032 half-cells were cycled within voltage range (3.0 - 4.3 V vs. Li/Li^+ for cathodes; 0.01 - 1.5 V vs. Li/Li^+ for anodes) at a constant 0.2 C-rate for 100 cycles.

2.5.3 Cyclic Voltammetry (CV)

Cyclic voltammetry (CV) is an electrochemical technique in which the cell potential is scanned linearly (constant voltage scan rate ($V\ s^{-1}$)) between two set voltage limits, while the resulting current is recorded as a function of potential[100]. In a lithium-ion battery half-cell, CV reveals the characteristic oxidation and reduction peaks corresponding to lithium-ion insertion and extraction from the electrode material.

In this study, CV measurements were conducted using CR2032-type coin cells with the fabricated electrodes as the working electrode and lithium metal as the counter/reference electrode. The potential was scanned within a fixed voltage range (3.0 - 4.3 V vs. Li/Li^+ for cathodes; 0.01 - 1.5 V vs. Li/Li^+ for anodes) at multiple scan rates, while the current response was continuously recorded. And the experiment was performed on a potentiostat (Biologic SP-240, Bio-Logic Science Instruments, United Kingdon). CV was applied for two primary purposes. First, to evaluate whether aqueous processing induced any changes in the electrochemical reaction mechanism of the electrodes. This was achieved by comparing the redox peak positions and peak currents between electrodes fabricated with and without water exposure. Second, CV was used to determine the lithium-ion diffusion coefficient through Randles–Sevcik analysis, the details of which are presented in a subsequent section.

2.5.4 Electrochemical Impedance Spectroscopy (EIS)

Electrochemical impedance spectroscopy (EIS) is an electrochemical technique used to characterise the internal resistances and kinetic processes within a battery or electrode[101]. In this study, EIS was selected as a safe method, as the applied AC perturbation amplitude was limited to 10 mV, which will not induce significant lithium-ion intercalation, electrolyte decomposition, or other side reactions. All measurements were performed at open-circuit

voltage to avoid altering the state of charge of the cell. The minimal energy input associated with this technique ensured minimal heat generation and no measurable degradation of the electrolyte or electrode materials, thereby enabling repeated measurements on the same cell throughout its lifetime. In EIS measurements, a AC voltage will be input, and the instrument will respond with an AC current[102]. The impedance $Z(\omega)$ is calculated as:

$$Z(\omega) = \frac{V(\omega)}{I(\omega)}$$

In this study, EIS experiment was performed on a potentiostat (Biologic SP-240, Bio-Logic Science Instruments, United Kingdon). And the EIS data was presented in a graphical way called Nyquist plot on EC-Lab software, where the imaginary part of the impedance (Z'') is plotted against the real part of the impedance (Z') for a range of frequencies[103].

In Nyquist plot, the input sinusoidal voltage:

$$E(t) = E_0 \sin(\omega t)$$

And the system responds with a sinusoidal current:

$$I(t) = I_0 \sin(\omega t + \varphi)$$

Where φ is the phase angle between voltage and current.

The impedance at angular frequency ω is:

$$Z(\omega) = \frac{V(\omega)}{I(\omega)} = \frac{E_0 \sin(\omega t)}{I_0 \sin(\omega t + \varphi)} = \frac{E_0}{I_0} \cdot e^{j\varphi}$$

Where $j = \sqrt{-1}$.

Following the above expression and extract the real part $Z'(\omega)$ and imaginary part $Z''(\omega)$,

$$Z'(\omega) = |Z| \cos(\varphi)$$

$$Z''(\omega) = |Z|\sin(\varphi)$$

Where $|Z| = \frac{E_0}{I_0}$ is the magnitude of the impedance.

In this thesis, EIS is employed, and the Nyquist spectra are fitted with an equivalent circuit to quantify the internal resistance contributions of the cell. At high frequency, the x-axis intercept corresponds to the ohmic resistance (R_s), which includes contributions from the electrolyte, separator, current collectors, and electrical contacts. At medium–high frequency, the first semicircle is associated with the interfacial resistance (R_{IR}), which represents ionic and electronic transport limitations across the interface and may also include contributions from SEI. At medium frequency, the second semicircle is assigned to the charge-transfer resistance (R_{CT}) reflecting the kinetics of the redox reactions. At low frequency, the liner line (Warburg impedance) corresponds to the solid-state lithium-ion diffusion within the electrode active material. The sum of R_s R_{IR} and R_{CT} provides the total internal resistance under this specific condition.

2.5.5 Diffusion Coefficient Determination Method

This thesis focuses on modifying electrode microstructures to enhance the electrochemical performance of lithium-ion batteries. The primary objective is to develop vertically aligned structures that optimize electrode porosity and reduce the tortuosity of the lithium-ion diffusion pathways. Such structural modifications are expected to facilitate ion transport by reducing diffusion restrictions. To quantitatively evaluate this improvement, the lithium-ion diffusion coefficient was determined as part of the electrochemical characterization. Both the Randles–Sevcik equation (derived from cyclic voltammetry data) and the Warburg coefficient (obtained from EIS) were employed to calculate the diffusion coefficient[104][105]. The resulting values were compared between electrodes fabricated using the DIT method and those prepared via conventional SC.

The lithium-ion diffusion coefficient D was calculated by the Randles Sevcik equation:

$$i_p = 2.686 \times 10^5 \times n^{\frac{3}{2}} \times A \times D^{\frac{1}{2}} \times C \times v^{\frac{1}{2}}$$

where i_p is the cathodic or anodic peak current from the CV curve (A), n is the number of electrons transferred in the redox event, A is the electrode area (cm^2), D is the diffusion coefficient ($cm^2\ s^{-1}$), C is the bulk concentration of NMC811 (mol cm^{-3}), and v is the scan rate ($V\ s^{-1}$).

To determine the diffusion coefficient using the Randles–Sevcik method, cyclic voltammetry was conducted at multiple scan rates. This approach is necessary because the method relies on the proportional relationship between the peak current (i_p) and the square root of the scan rate ($v^{1/2}$) for a diffusion-controlled process. By performing measurements at several scan rates and plotting i_p against $v^{1/2}$, a linear fit can be obtained. The slope of this line is used to calculate the diffusion coefficient. The use of multiple scan rates also serves as a validation to ensure that the redox process is indeed diffusion-controlled and not significantly affected by kinetic or capacitive effects. In this study, scan rates of 0.10, 0.20, and 0.50 mV s^{-1} were applied for the comparison of small-scale cathodes, while 0.05, 0.10, and 0.15 mV s^{-1} were used for the scaled-up cathode comparison. The CV test under different scan rate was performed on a potentiostat (Biologic SP-240, Bio-Logic Science Instruments, United Kingdon).

EIS was applied to determine the lithium-ion diffusion coefficient for the DIT graphite anode and the conventional SC graphite anode. In the Nyquist plot, the low-frequency region is dominated by the Warburg impedance, which arises from the semi-infinite diffusion of lithium ions within the electrode material. The lithium-ion diffusion coefficient (D_{Li+}) was calculated based on EIS using Warburg impedance analysis[106]. The Warburg coefficient (σ) was obtained by linear fitting of the real part of the impedance (Z′) versus the inverse square root

of angular frequency ($\omega^{-1/2}$) in the low-frequency region. The diffusion coefficient was then calculated using the following equation[107]:

$$D_{Li^+} = \frac{R^2T^2}{2A^2n^4F^4C^2\sigma^2}$$

where: D_{li^+} is the diffusion coefficient of lithium ions ($cm^2\ s^{-1}$), R is the gas constant (8.314 J $mol^{-1}\ K^{-1}$), T is the absolute temperature (K), A is the electrode surface area (cm^2), n is the number of electrons transferred per reaction, F is the Faraday constant (96485 C mol^{-1}), C is the molar concentration of lithium ions in the electrode (mol cm^{-3}), σ is the Warburg coefficient ($\Omega \cdot s^{-1/2}$) obtained from the slope of the Z' vs. $\omega^{-1/2}$ plot.

2.5.6 Energy Density Estimation in Battery Pack

All electrodes in this study were fabricated in the laboratory and assembled into CR2032 coin cells with dimensions of 3.2 mm in height and 20 mm in diameter. To enable comparison of the energy density with commercial products, which are typically manufactured in pouch cell format, a modelling approach was employed to project the performance of the fabricated cathodes into a larger pouch cell configuration. The estimated gravimetric and volumetric energy densities (Wh kg^{-1} and Wh L^{-1}, respectively) were obtained using the Cell Analysis and Modelling System (CAMS) developed by the Faraday Institution[108]. CAMS is designed to rapidly evaluate the potential energy density of various cell chemistries and formats. The model operates through a series of interconnected spreadsheets organised into five primary areas: Cell Modelling: containing the main model dashboard and output interface; Cell Database: comprising both a commercial cell database and a database of modelled cell designs. Material Database: including data for separators, electrolytes, and electrode active materials. Cell Calculations: containing calculation sheets used to perform the modelling operations. Model Defaults and Constants: outlining the underlying assumptions, default formats, and cell dimensions used in the model.

2.6 Battery Performance Stability

To ensure reproducibility of both microstructure and electrochemical performance, and to demonstrate that the fabrication method can be scaled up without introducing significant variability, all electrodes were produced under ambient laboratory conditions with temperatures ranging from 5 °C to 30 °C. Across this temperature range, the fabricated electrodes exhibited consistent electrochemical performance, and their microstructural features remained comparable as observed through SEM morphology analysis. For each electrode type, a total of 30 units were fabricated to support the assessment of process stability.

In this study, a scaled-up DIT cathode was also fabricated, for which a new schematic was designed to accommodate the larger electrode dimensions. To evaluate the compositional uniformity of the scaled-up DIT electrode sheet, thermogravimetric analysis (TGA) was conducted using a five-point sampling method, with the sampling locations indicated in Figure 2.8[109]. From each selected region, approximately 10 mg of electrode material was collected and analysed under identical conditions. TGA measurements were performed using an STA 449 F5 Jupiter simultaneous thermal analyser (Netzsch GmbH, Germany) over a default temperature range of 20 - 1600 °C. Prior to each experiment, a background measurement was conducted for baseline correction by placing a reference crucible containing Al_2O_3 and an empty crucible on the balance holder. Data were processed using Proteus software (Netzsch GmbH, Germany). Argon and air purge gases were supplied at a flow rate of 50 mL min^{-1}, with protective argon at 20 mL min^{-1}. For the NMC811 electrode samples, the temperature program consisted of heating under argon from 20 °C to 280 °C, followed by heating under air from 280 °C to 800 °C, at a rate of 3 °C min^{-1}.

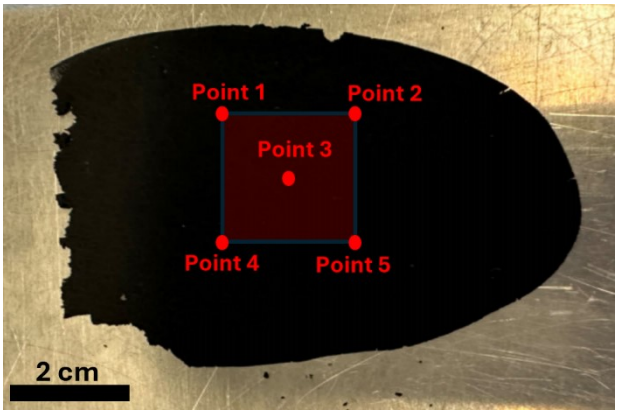


Figure 2.8 Schematic of the five-point sampling locations used for compositional uniformity analysis of the scaled-up DIT cathode sheet.

Chapter 3

3 Battery Cathode with Vertically Aligned Microstructure Fabricated by Directional Ice Templating

3.1 Introduction

Electrode processing methods can significantly impact electrode microstructure and LIB performance[110][111]. In the conventional cathode manufacturing method of SC, the slurry is made by mixing NMC811 particles with electrical conductivity enhancer (usually carbon nanoparticles) and binder usually in a toxic, combustible, organic solvent NMP[112][113], then a doctor blade or a similar equipment is used to coat the prepared slurry on an aluminium foil followed by drying and calendar steps[114][115]. This method helps hold the particles together and adheres them to the current collector[116, 117]. Conventional SC electrodes are 100-200 μm in thickness, higher electrode thicknesses and mass loadings can increase the proportion of electrode active materials and increase battery energy densities at the cell-stack level within a confined volume[118][119]. However, the capillary force generated in the drying process by heating causes electrodes to crack and prevents SC from making thicker (≥340 μm) electrodes. Furthermore, the electrode microstructure made by the SC method is not controlled well[120], the congested particle arrangement with tortuous pores prevents efficient electrolyte penetration and ion diffusion, and this problem is exacerbated at higher thicknesses[121]. Poor lithium-ion diffusion limits the contact between the active electrode material particles and the electrolyte[122][123], hindering the ability of lithium ions moving into and out of the electrode material particles and impairing rate capability of the cell especially at faster (dis)charge rates[124][125]. Some studies focus on investigating component-interface interactions and the mechanical behaviour of electrodes such as studying mechanical relaxation behaviour and bending capability[126], highlighting the importance of the active material microenvironment (ME@AM)[127, 128]. Therefore, optimizing electrode microstructure is imperative for enhancing the overall performance and efficiency of LIBs[129][130][131]. Many studies aim to develop new active materials and applying additives to battery components [132], but less attention falls on the processing to control the hierarchical nano- and microstructure[133][54].

In this work, we show a novel, rapid bottom-up approach of DIT to make NMC811 cathodes with high thickness (660-1100 μm) and control the anisotropic cathode microstructure containing alternating vertically aligned lamellae of electrode materials (10-15 μm in width) and pore arrays (6-12 μm in diameter) through the electrode thickness to provide fast dual electron and lithium ion transport pathways and thus to improve the battery energy density and C-rate capability at the cell-stack level simultaneously[50]. Compared with other methods such as 3D printing, laser structuring, etc., the advantages of the DIT method include (i) scalability (we can use the scalable slurry coater and simply apply a directional freezing temperature gradient from the bottom during rapid formation of *in situ* ice template), (ii) versatility (this method can be applied to a wide range of cathode and anode materials), and (iii) structure controllability (the pore channel diameter and porosity of the structure can be controlled by the solid concentration of electrode slurry). We have developed the DIT method for other materials of $LiCoO_2$ [54] and $LiFePO_4$ [134] and directional freezing and polymerisation (DFP) method for NMC811 in polymer-based solid batteries [56]. Different active material size and surface characteristics resulted in slightly different pore channel diameter and tortuosity, but the vertically aligned microstructure was maintained. Here, we develop the aqueous DIT method for the lithium-rich NMC811 cathode materials for the first time. There are two major challenges associated with using DIT of making NMC811 cathodes, one is aqueous processing of NMC811, and the other is reducing porosity of the DIT method to increase battery energy density. This chapter addresses both of the key challenges.

Firstly, the solvent of the slurry is changed from NMP that is usually used in SC of cathodes to water in DIT which can improve processing sustainability[135]. We systematically studied the effects of the aqueous processing on the NMC811 properties. Any residue water remained in the electrodes after electrode drying or cycling at voltages over the upper voltage limit (e.g. 4.6 V[136][137]) may cause side reactions of water with $LiPF_6$ in the electrolyte that will harm

electrolyte stability and ultimately battery capacities[138][139]. To address the first challenge, all water was rigorously removed from the DIT cathode directly from ice to vapor during ice sublimation before battery assembly in our experiments to prevent any residue water. Although water in contact with the NMC particles during processing may cause side reactions with NMC811 such as lithium leaching after prolonged exposure to water[140][141], this is usually due to the long term exposure rather than the rapid process of DIT, e.g. a research showed long term (>28 days) exposure to the ambient environment (CO_2, H_2O, and O_2) may affect the performance of high-nickel NMC (Ni wt% among all transition metals >80%) materials due to the formation of coating consisting of carbonate, hydroxide species and enrichment of lithium ions on the particle surface[142]. On the other hand, aqueous SC within a controlled processing environment has been demonstrated on NMC811 materials, showing water does not affect the electrochemical properties of NMC811[143]. We developed the DIT process to involve very rapid nucleation and growth of ice and used a high solid concentration slurry to minimize the contact between the NMC811 particles and water[142][144]. We used a variety of surface-sensitive techniques to study the chemical composition, bonding and morphology of the top 35 nm of the particle surface under different conditions. We showed the properties of the NMC particles exposed to water within the duration and controlled environment of DIT were compatible to those of the pristine NMC particles in ambient conditions.

Secondly, DIT usually makes samples with a high porosity (50-60%)[145] which may reduce energy densities at the practical cell-stack level for real battery applications. We studied changing electrode slurry concentrations as an effective method to reduce porosity to 35% to be compatible to the conventional SC electrodes while creating the aligned microstructure for the DIT electrodes. We systematically compared the chemical, nano- and microstructural, and electrochemical properties of the NMC811 cathodes made by DIT and conventional SC. Notable differences emerged across various charge rates, at a (dis)charge rate of 0.1 C (the

(dis)charge current density was 1.4 and 0.76 mA cm^{-2} for the DIT and SC electrodes, respectively, due to the almost doubling of electrode thickness and mass loading of the DIT than SC), the DIT cathode exhibited an areal capacity of 12 mAh cm^{-2} and a gravimetric capacity of 201 mAh g^{-1}, compared to an areal capacity of 7.0 mAh cm^{-2} and a gravimetric capacity of 200 mAh g^{-1} for the cathode made by SC. The advantage was already obvious when the (dis)charge rate was increased to 0.4 C (the (dis)charge current density was 5.7 and 2.9 mA cm^{-2} for the DIT and SC electrodes, respectively), the DIT cathode exhibited a higher areal capacity of 9.8 mAh cm^{-2} and gravimetric capacity of 186 mAh g^{-1}, compared to 2.1 mAh cm^{-2} and 64 mAh g^{-1} for the SC cathode. At higher C-rates of 0.5, 1 and 2 C, the DIT cathode also maintained higher areal and gravimetric capacities than the SC electrodes. In this work, we highlight the following key contributions: (i) developing aqueous processing for the NMC811 material within the DIT processing window to improve processing sustainability; and (ii) overcoming low porosity that is usually associated with the DIT processing method and achieving higher electrode densities compared to the previous electrodes, e.g.[134] and increasing volumetric capacity and energy density.

3.2 Results and Discussion

3.2.1 Fabrication of Cathodes by DIT

The slurry composition consisted of NMC811 (90 wt%) as the active material, complemented by carbon black nanoparticles (5 wt%) serving as the conductive element[146], and mixed binders of SBR (3 wt%) and CMC (2 wt%)[147]. The weight ratio between the solid mixture and deionised water was 30:70 and 40:60 for the dilute and concentrated slurry, respectively. We denote the electrodes as DIT-D (electrode made by the dilute slurry) and DIT-C (electrode made by the concentrated slurry), respectively. We investigated the effects of solid concentration in electrode slurry on controlling pore channel diameter and porosity. The lab-made apparatus of the DIT method integrates three parts including a lab-designed round ABS mould for the electrode slurry, a copper cold finger, and a container of liquid nitrogen[51]. The

ABS mould was placed on top of the copper cold finger platform which was placed in the container (Figure 1.5a). The electrode active material particles and electrical conductivity enhancer carbon black with polymeric binder were first homogeneously mixed in the electrode slurry (Figure 1.5b). During the DIT process, the electrode slurry experienced rapid vertical directional freezing from underneath. Ice crystals started to nucleate at the supercooling interface on the copper cold finger. Ice columns started to grow vertically from the bottom along the freezing temperature gradient. As these dendrites grew along the vertical freezing direction, the ice dendrites exerted pressure on the NMC811 and carbon particles, displacing them into the columns in-between the ice dendrites and *in situ* shaping them into the desired microstructure (Figure 1.5c). As heat was efficiently taken away from the electrode slurry through conduction, ice columns continued to grow vertically through the entire electrode thickness (Figure 1.5d). After the electrode reached full solidity, the ice columns were directly sublimed from solid to vapour through freeze-drying to preserve the formed microstructure. The critical step of ice sublimation prevented the ice dendrites from transitioning back into a liquid phase before ice removal, and hence, preventing the effect of shrinkage that usually takes place in conventional SC electrodes due to the capillary force during conventional evaporation of solvent from liquid to vapour through heating[53]. Thus, we were able to make ultra-thick (660-1100 μm) DIT cathodes without cracking to increase mass loading of the electrodes while maintaining the designed internal microstructure.

The reference electrode group was made by the conventional SC method[7]. The average thickness of the SC electrode was 340 μm with an average mass loading of 36 mg cm^{-2}. The reason for using this thickness was that this was the highest thickness (for fair comparison in ion diffusion kinetics with the ultra-thick DIT electrodes) made by SC without cracking due to the capillary forces during heat drying. The average thicknesses of DIT-C and DIT-D electrodes were 660 and 1070 μm, respectively, with the same average mass loading of 70 mg cm^{-2}. Note

that we deliberately made the DIT electrodes thicker to demonstrate that even at this high thickness, ion transport kinetics through the electrode thickness were still higher than the thinner conventional SC electrodes. In real battery applications, the DIT electrode thickness can be modified according to the requirements of specific applications.

3.2.2 Cathode Active Material Particle Surface Properties

To investigate the influence of water exposure on NMC811, we investigated three types of electrode for comparison, (i) NMC-ambient conditions (NMC811 without deliberate water exposure), (ii) NMC-30 min (NMC811 particles deliberately immersed in water for 30 minutes to simulate conditions in the DIT method where the NMC811 particles are in contact with water for 25–30 minutes), (iii) NMC-7 days (NMC811 particles immersed in water for prolonged exposure of seven days). All the NMC particles then underwent freeze-drying before being investigated. TEM was employed to investigate the NMC811 particle surface morphology and to quantify the thickness of the coating (if any) on the particle surface from reacting with water. The TEM images in Figure 3.1a,d show the pristine NMC811 particle in ambient conditions that has not been deliberately exposed to water (NMC-ambient conditions), the particle displayed a coating thickness of ~5.0 nm, likely due to the inevitable exposure to CO_2, moisture, and O_2 in the ambient environment. The particle immersed in water for 30 minutes (NMC-30 min) exhibited a similar coating thickness of ~5.5 nm (Figure 3.1b,e), indicating minimal additional reaction compared to the pristine particle. In contrast, the sample immersed in water for 7 days (NMC-7 days) showed a substantially thicker coating of ~30.0 nm (Figure 3.1c,f), suggesting significant surface reactions over the prolonged exposure.

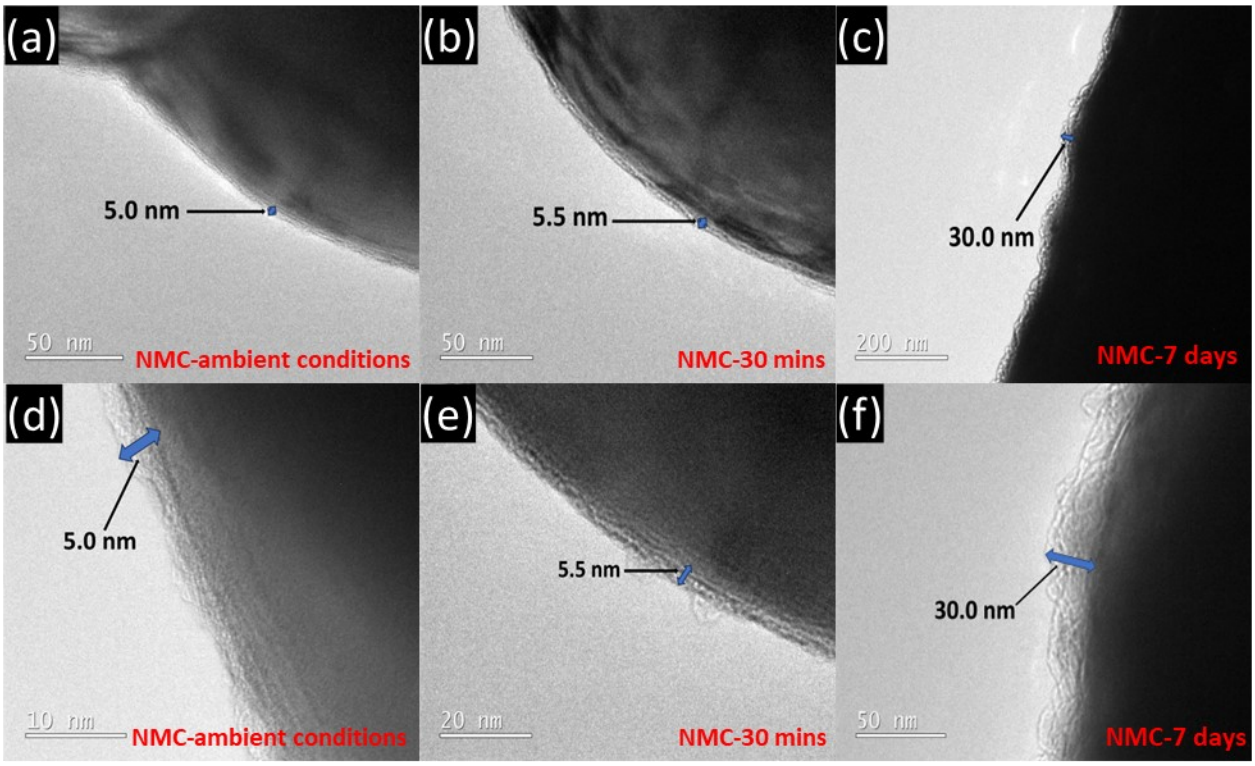


Figure 3.1 TEM images of the NMC811 particle surface and their corresponding magnified images for (a,d) pristine particle in ambient room conditions without deliberate water exposure; (b,e) particle immersed in water for 30 minutes; (c,f) particle immersed in water for 7 days.

Figure 3.2a shows the XPS C1s spectra for the three types of particles superimposed together, showing the highest intensity of Li_2CO_3 was found in NMC-7 days. The intensity ratio between the Li_2CO_3 and C-C peaks was 12.0%, 16.0% and 26.6% for NMC-ambient conditions, NMC-30 min, and NMC-7 days, respectively. Figure 3.2b-d show the fitted XPS C1s spectra for the three types of particles individually, with the highest intensity of the C-O=C peak for the NMC-7 days sample.

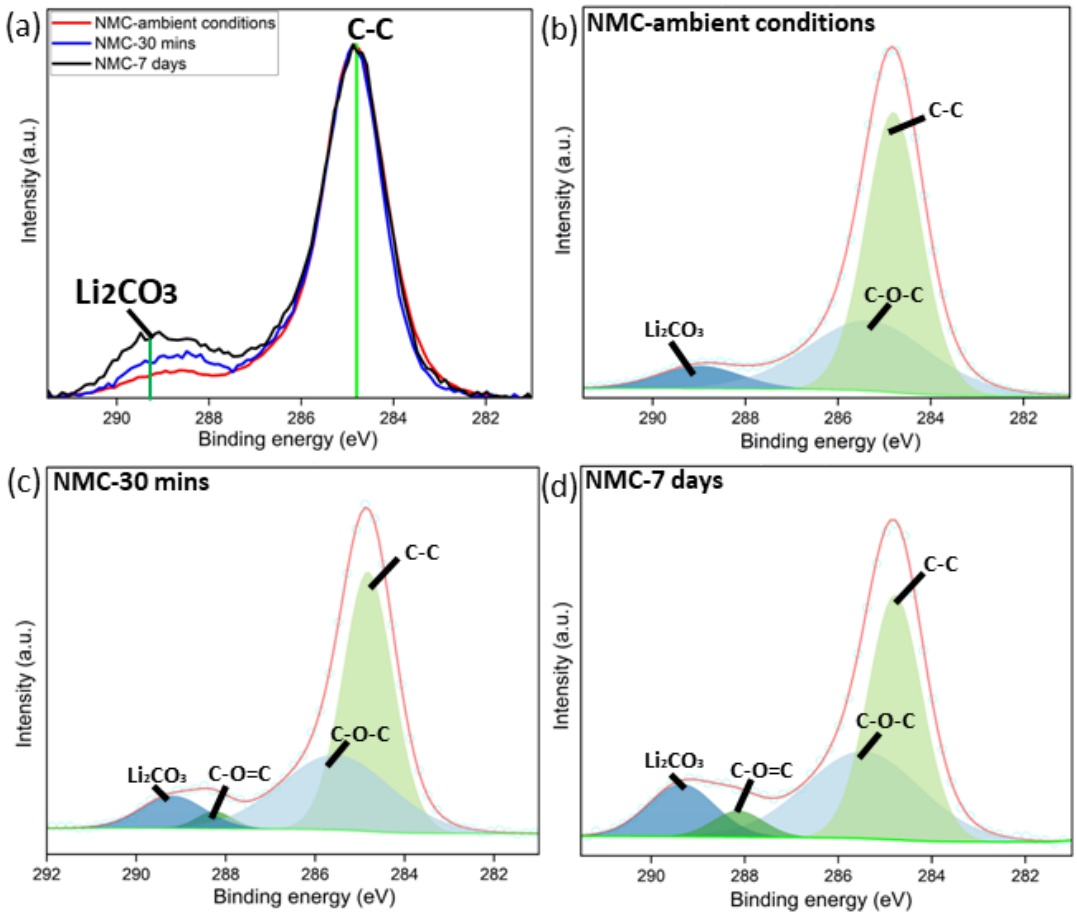


Figure 3.2 XPS C1s spectra of (a) three types of NMC811 particles superimposed together showing the content of Li_2CO_3; and the fitted spectra of (b) pristine particle in ambient room conditions without deliberate water exposure (NMC-ambient conditions); (c) particle immersed in water for 30 minutes (NMC-30 min); (d) particle immersed in water for 7 days (NMC-7 days).

To provide quantitative analysis of the distributions of lithium-ion enrichment and the carbonate and hydroxide species, ToF-SIMS depth profiling was conducted on the three types of particles. The samples were sputtered using an ion beam, allowing for depth profiling of the top 35 nm on the particle surface. The ToF-SIMS depth profiles show the negatively charged CO_3^{2-} and OH^- species content and indicate that NMC-7 days had the highest intensities of CO_3^{2-} and OH^- at each depth, and NMC-30 min and NMC-ambient conditions exhibited much lower intensities (Figure 3.3a), consistent with the thicknesses of the coatings observed in TEM in Figure 3.1. Figure 3.3b presents ToF-SIMS depth profiles of the positively charged Li^+ specie from the surface to the inside particle of the three types of samples. NMC-7 days exhibited a significantly higher Li^+ intensity compared to the other two samples. Corroborating with Figure

3.3a, the results show a higher presence of Li_2CO_3 and LiOH on the particle surface of NMC-7 days, suggesting that more Li^+ was leached from NMC-7 days. The consistency among the TEM, XPS and ToF-SIMS results suggests that the coating formed during 30 minutes of water exposure was comparable to the naturally occurring coating formed under ambient conditions. These results indicate that exposure of NMC811 to water for less than 30 minutes during aqueous slurry mixing resulted in minimal side reactions compared with the naturally occurring coating for the pristine particles. However, longer exposure time may lead to substantial surface reactions and coating formation.

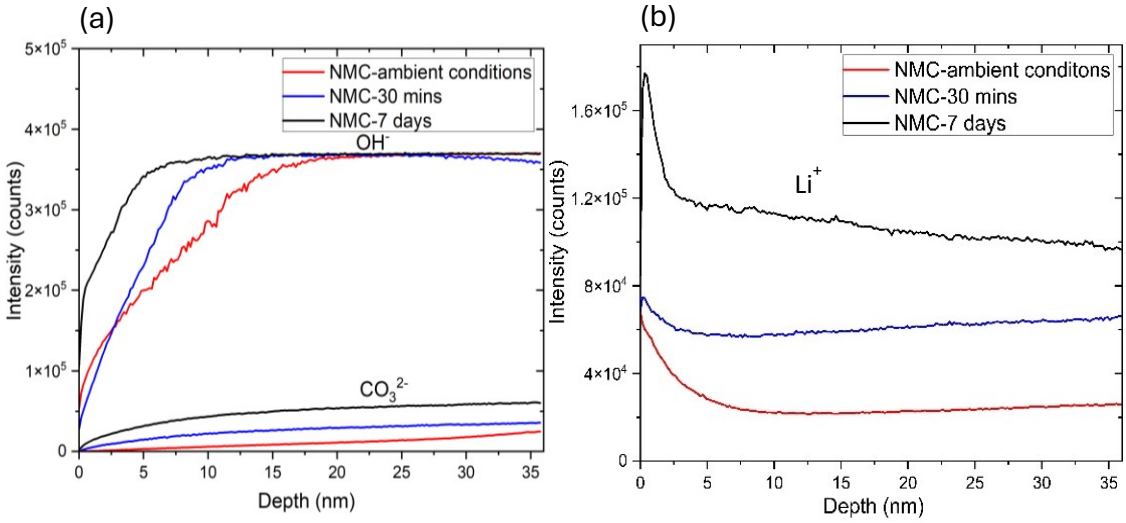


Figure 3.3 ToF-SIMS depth profile showing the formation of Li_2CO_3 and LiOH from the surface of NMC811 particles to the inside particles under three conditions: NMC-ambient conditions; NMC-30 min; and NMC-7 days. (a) ToF-SIMS depth profiles showing the intensity of OH^- and CO_3^{2-} as a function of sputtering depth, (b) ToF-SIMS depth profile of Li^+.

A CV test was conducted on electrodes prepared using the DIT method, and the resulting CV curve is shown in Figure 3.4. In the pristine NMC811 electrode fabricated by the conventional SC method, the stepwise redox behaviour of Ni and Co resulted in four distinct peaks—two oxidation and two reduction peaks, each pair corresponding to a specific redox reaction at given potentials. During the first CV scan, irreversible electrochemical processes occur as the electrode equilibrates with the electrolyte. These include surface reactions, initial structural activation and SEI formation. All of these contribute to deviations in peak shape and intensity

compared with later cycles. During charging, the first oxidation peak appeared within the 3.7 - 4.0 V range, corresponding to the removal of Li^+ from the NMC811 structure, while the second oxidation peak occurred between 4.2 - 4.5 V due to further Ni oxidation [148–150]. During discharge, the first reduction peak emerged between 4.1 - 3.9 V, indicating lithium reinsertion, followed by a second reduction peak in the 3.7 - 3.6 V range, representing additional lithium insertion. After the first cycle, the formation of a cathode-electrolyte interphase stabilized the system, leading to more consistent and overlapping CV curves in subsequent cycles. As shown in the Figure 3.4, the CV curves of the NMC811 electrode fabricated by the DIT method at 0.1 mV s^{-1} over the first four cycles exhibited a behaviour highly consistent with conventional NMC811. From the second to the fourth cycle, the CV curves overlapped more closely, demonstrating stable electrochemical behaviour. The oxidation peaks for these cycles appeared at 3.87 and 3.88 V (first oxidation) and 4.24 and 4.25 V (second oxidation), while the reduction peaks were observed at 4.08 and 4.07 V (first reduction) and 3.65 and 3.62 V (second reduction). This strong agreement with the conventional NMC811 characteristics using NMP solvent, further confirms that the aqueous DIT method did not alter the redox reaction mechanism.

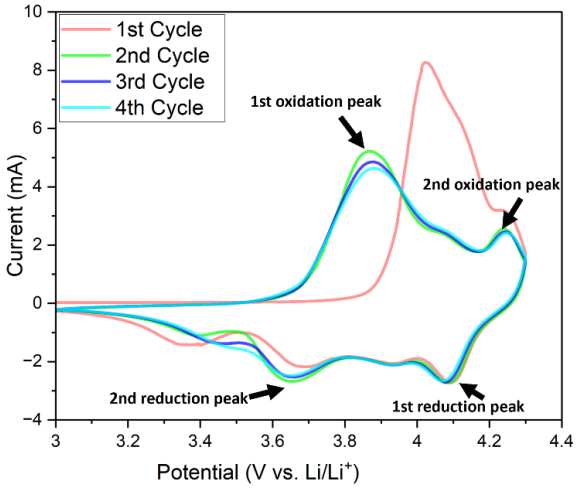


Figure 3.4 CV curves of DIT-C electrode at a scan rate of 0.1 mV s^{-1}

3.2.3 Electrode Structures

Figure 3.6 shows the cross-sectional SEM images of the SC electrode, DIT electrode made by dilute slurry (DIT-D), and DIT electrode made by concentrated slurry (DIT-C), with increasing magnifications, and the blue arrows in the figures show the freezing direction during the DIT process. The cross sections were polished by an argon ion beam to reveal the interior microstructure of the electrodes. The average secondary particle size of NMC811 was 12 ± 5 μm, while the carbon black particles were around 8-100 nm. Figure 3.6a,b shows non-directional porosity with highly tortuous pores for the SC electrode. Figure 3.6c-f show well-ordered pore channels extending through the thickness direction for the DIT-D and DIT-C electrodes. These pore channels were formed along the freezing direction during the ice columns growth. The vertical structure framework enables shorter diffusion pathways along the kinetically favourable through-electrode-thickness direction for ion diffusion during (dis)charging. Individual NMC811 particles were observed in DIT-C in Figure 3.6e,f, the width of the lamellae of the electrode materials was 10-15 μm, facilitating efficient insertion and extraction of lithium ions as active sites for electrochemical processes. The SC electrode exhibited a large pore size distributions of 2-30 μm (Figure 3.6a,b), whereas the DIT-D (Figure 3.6c,d) and DIT-C (Figure 3.6e,f) electrodes exhibited more uniform pore channel diameters of 4-10 μm and 2-6 μm, respectively. The overall porosity was 35%, 57%, and 35%, ±5%, for the SC, DIT-D, and DIT-C electrodes, respectively, demonstrating that increasing the solid content in the electrode slurry for DIT effectively increased electrode density to be compatible to that of SC electrodes, and modifying the electrode slurry solid concentration can effectively control the pore-channel size and porosity. The DIT electrodes were also able to be made much thicker (660-1100 μm) than the SC electrode (340 μm), and no obvious cracks were observed in the DIT electrodes, showing good mechanical properties of the DIT electrodes. Additionally, Figure 3.5 shows a top view SEM image of DIT-C (freeze direction was towards out of the page) after ion milling to reveal the internal microstructure, a cellular structure emerged

wherein all active material particles were interconnected in the conductive network of the electrode. We have also performed calendering tests on the DIT electrodes showing the electrode thickness of porosity were reduced by moderate calendaring, the vertically ordered porous structures bended but largely preserved the ordered porous microstructure.

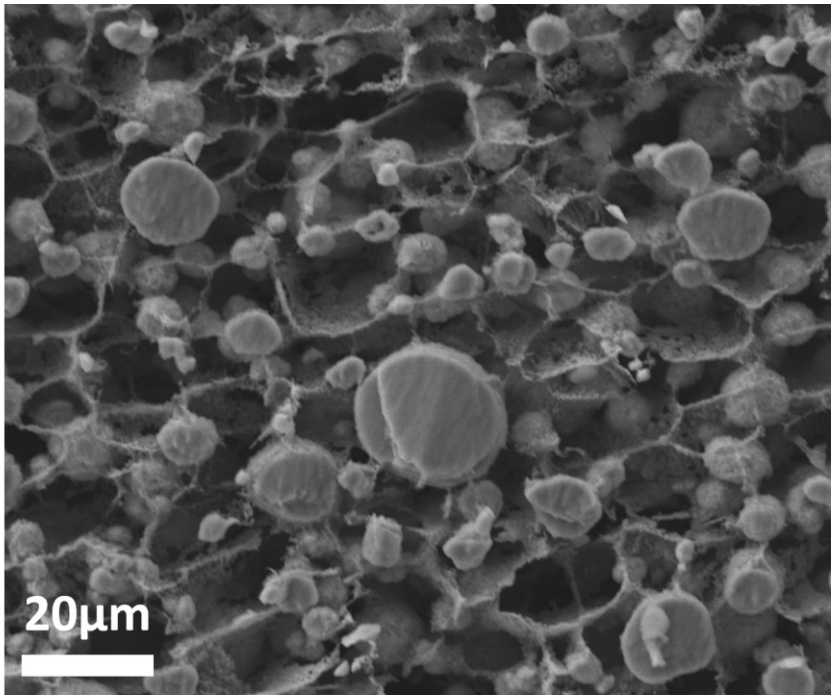


Figure 3.5 Top view SEM image (after ion milling to reveal the inside microstructure) of DIT-C electrode. The freeze direction was towards out of the page, a cellular structure emerged wherein all active material particles were interconnected in the conductive network of the electrode.

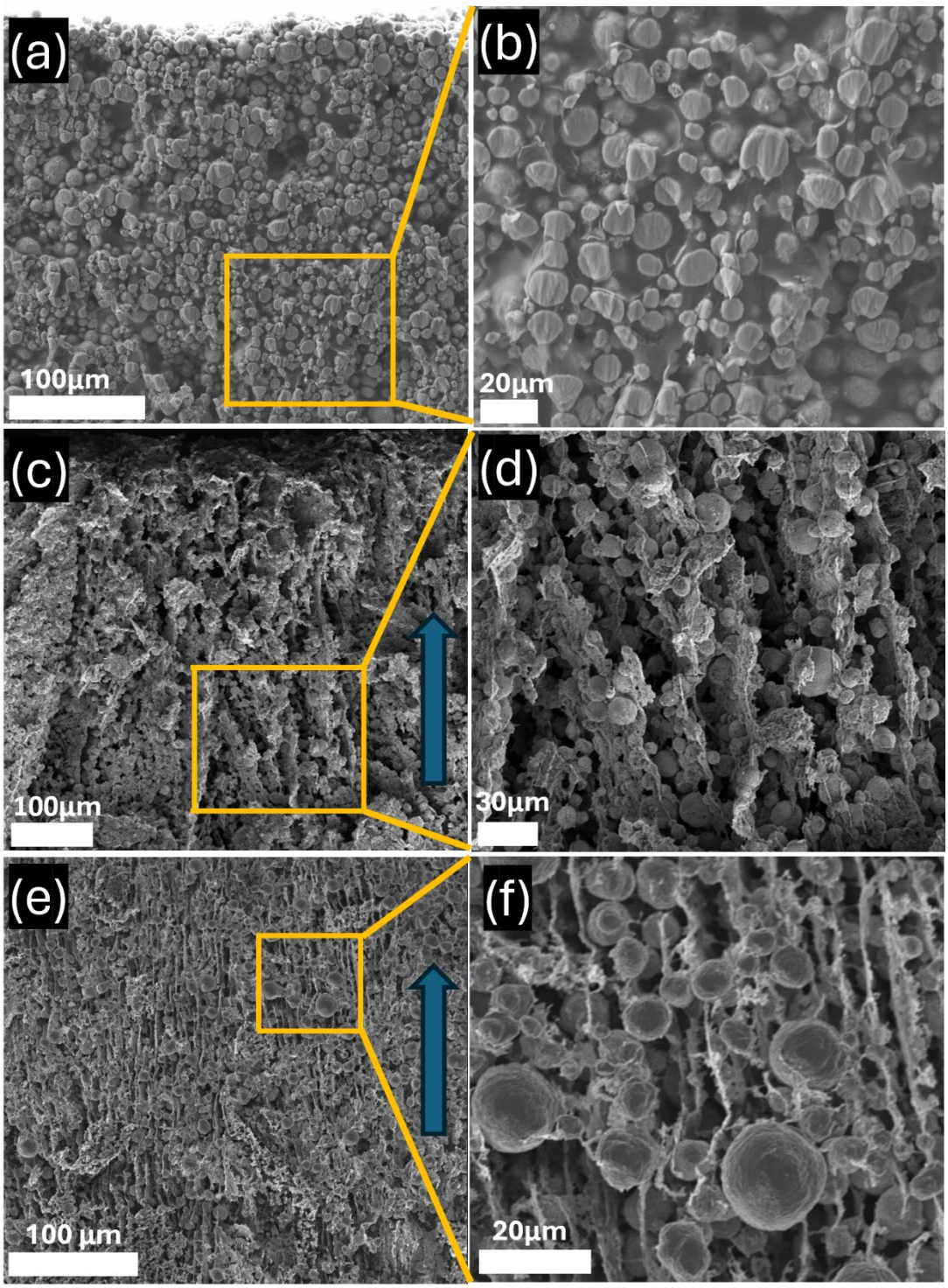


Figure 3.6 Cross-sectional SEM images of (a–b) SC electrodes; (c–d) DIT electrodes made with a dilute slurry (30:70, DIT-D); and (e–f) DIT electrodes made with a concentrated slurry (40:60, DIT-C). Blue arrows in (c) and (e) mark the freezing direction used in the DIT process.

3.2.4 Electrochemical Performance

Figure 3.7a,b show the galvanostatic (dis)charge profiles for the DIT-C and SC cathodes, showing both gravimetric and areal capacities at (dis)charge rates of 0.1 and 0.4 C. The mass loading of the DIT-C cathode is almost double of the thick SC cathode we made for comparison purposes and the mass loading of the DIT-C cathode is almost four times of the average of the SC cathodes in the literature [151], hence, the magnitudes of the current applied (parameter for practical applications) to the three types of cathode at the same C rate were different. At 0.1 C, the (dis)charge current density was 1.4 and 0.76 mA cm^{-2} and the gravimetric capacities were 201 and 200 mAh g^{-1} for the DIT-C and our SC cathodes, respectively. The gravimetric capacity of DIT-C was also comparable to the other thinner NMC811 cathodes made by SC (17 mg cm^{-2}) in the literature[151], although the current applied to the DIT electrodes (70 mg cm^{-2}) and our SC electrodes (36 mg cm^{-2}) was significantly higher than the conventional SC electrodes, demonstrating that the DIT-C cathode fully utilised its active materials in the aligned microstructure despite the higher thickness. On the other hand, due to the higher mass loading of the DIT-C cathode, DIT-C significantly increased areal capacity (12 mAh cm^{-2}) compared with 7.0 mAh cm^{-2} for the SC electrode in this study and ~3.25 mAh cm^{-2} for the other SC cathodes in the literature[152]. The Coulombic efficiency was 98.5% and 97% for the DIT-C and SC cathodes, respectively. Figure 3.11 shows that the DIT-D cathode exhibited an areal capacity of 9.3 mAh cm^{-2} since it still had higher mass loading than SC and the vertical pore arrays improved ion diffusion. At 0.4 C, the (dis)charge current densities were 5.7 and 2.9 mA cm^{-2} and the gravimetric capacities were 186 and 64 mAh g^{-1} for the DIT-C and SC cathodes, respectively. The lower gravimetric capacity of the SC cathode here is because the SC cathode thickness in this study (340 μm) was still 2-3 times higher than that of conventional SC cathodes[153] and the tortuous porosity heavily impeded ion diffusion. In contrast, the DIT-C cathode still maintained a higher gravimetric capacity and 4 times higher areal capacity (9.8

mAh cm^{-2}) than the SC cathode (2.1 mAh cm^{-2}). Figure 3.12 shows the DIT-D electrode exhibited a medium areal capacity of 8.0 mAh cm^{-2} at 0.4 C.

Figure 3.7e shows the comparison of reversible areal capacities for the DIT-C and SC cathodes from 0.1 C to 2 C (the corresponding reversible gravimetric capacities comparison is shown in Figure 3.13. Due to the significantly higher mass loading of the DIT-C electrode than the SC electrode[154], the current densities applied to DIT-C (mass loading 70 mg cm^{-2}) at 0.1, 0.2, 0.4, 0.5, 1, and 2 C were approximately equivalent to the current densities applied to our SC electrode (mass loading 36 mg cm^{-2}) at 0.2, 0.4, 0.8, 1, 2, and 4 C, and the current densities applied to conventional SC electrodes in the literature (average mass loading 17 mg cm^{-2} [155] at 0.4, 0.8, 1.6, 2, 4, and 8 C. At the same current density of 1.4 mA cm^{-2} for a fair comparison, the DIT-C electrode exhibited 200 mAh g^{-1} whereas the SC electrode exhibited 182 mAh g^{-1}; at the same current density of 1.4 mA cm^{-2}, the DIT-C electrode exhibited 156 mAh g^{-1} whereas the SC electrode exhibited 140 mAh g^{-1} [156]; and the difference became larger and larger as the current density increased, showing the advantage of the DIT electrode. The areal capacity of DIT-C was 2-4 times higher than SC at all C rates. The trend was the same for the gravimetric capacities, showing the advantages of DIT-C at increasing C rates. Upon reverting the C-rate back to 0.1 C, the DIT-C capacity restored to its initial value, exemplifying the robustness of the DIT method, whereas the inability of the SC electrode to fully recover to its initial capacity upon returning to 0.1 C indicate structural instability of the randomly porous microstructure. Figure 3.14 summarises the rate capability of the DIT-D electrode at increasing C rates, showing the DIT-D electrode capacities were consistently higher than SC but lower than DIT-C. These results demonstrate that the aligned pore arrays in the DIT electrodes improved lithium-ion diffusion kinetics through the electrode particularly at increasing C rates.

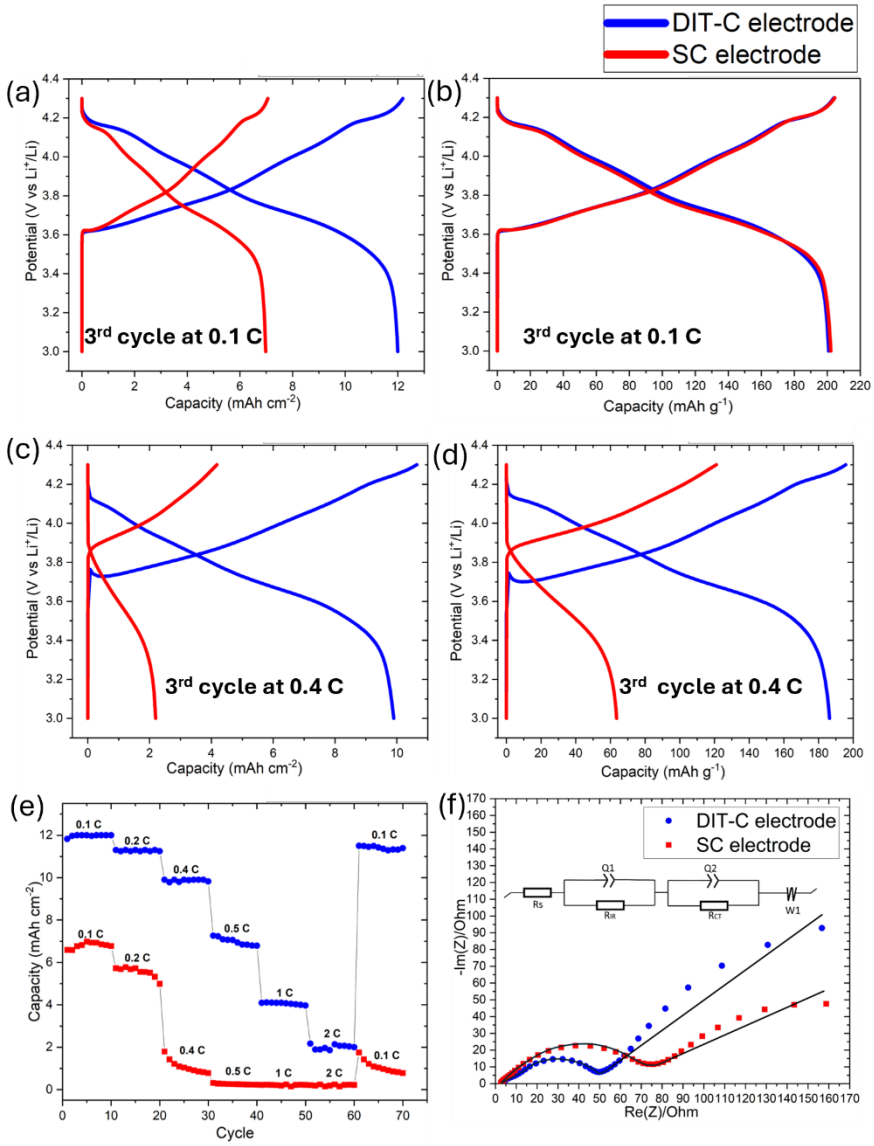


Figure 3.7 Galvanostatic charge and discharge profiles showing (a) areal capacities at 0.1 C; (b) gravimetric capacities at 0.1 C; (c) areal capacities at 0.4 C; (d) gravimetric capacities at 0.4 C. (e) reversible areal capacity of electrodes at different C rates. (f) Equivalent circuit and fitted Nyquist plots for comparison between DIT-C and SC cathodes.

EIS was applied after 3 charge and discharge cycles. Figure 3.7f shows the Nyquist plot of DIT-C and SC, and the corresponding equivalent circuit is shown in the Figure 3.7f[157]. The intercept between the Nyquist plot and Z' axis at high frequency indicates the resistance of electrolyte R_s and was estimated at 1.9 and 3.5 Ω for the DIT-C and SC electrodes, respectively. The high frequency semicircle and midfrequency semicircle emerged together, where the high frequency semicircle diameter indicates charge transfer resistance R_{CT} and the midfrequency semicircle diameter can be attributed to the electrolyte-oxide interfacial impedance R_{IR}[158].

The overall R_{CT} and R_{IR} was 46.8 and 78.4 Ω for the DIT-C and SC electrodes, respectively, indicating lower impedance for the aligned microstructure.

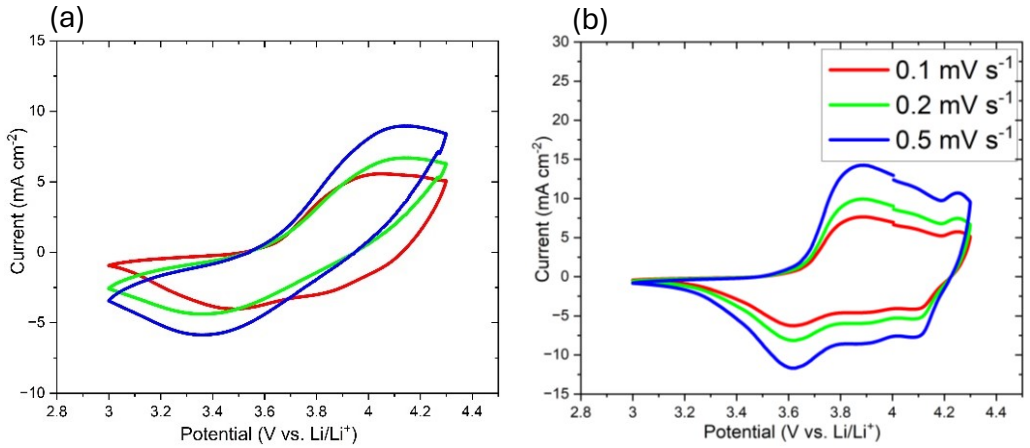


Figure 3.8 CV curves of (a) SC cathode and (b) DIT-C cathode, at scan rates of 0.1, 0.2, and 0.5 mV s^{-1}.

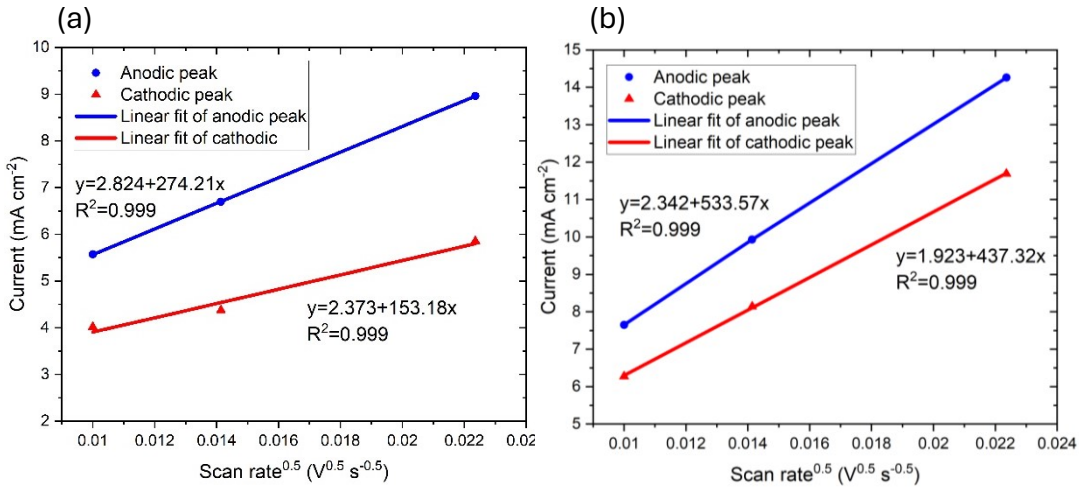


Figure 3.9 Fitting slop of (a) SC cathode and (b) DIT-C cathode from the normalized peak current of the CV curves.

Figure 3.8 shows the CV curves of the DIT-C and SC cathodes at 0.1-0.5 mV s^{-1} where the redox peaks are more prominent in DIT-C (Figure 3.8 b) than SC (Figure 3.8 a). Each peak in the CV curves represents reduction or oxidation reaction[159]. The normalized peak current (i_p) had a linear relation with the square root of the scan rate ($v^{0.5}$) as shown in Figure 3.9, indicative of an ion diffusion-controlled process. The slope values for the cathodic and anodic peaks were similar for the DIT-C cathode, but asymmetric for the SC cathode, indicative of more reversible redox reactions and faster ion diffusion in both ways in the aligned

microstructure of the DIT-C electrode. The lithium-ion diffusion coefficient *D* was calculated by the randles-sevcik equation[160][161]:

$$i_p = 2.686 \times 10^5 \times n^{\frac{3}{2}} \times A \times D^{\frac{1}{2}} \times C \times v^{\frac{1}{2}} \quad (1)$$

where i_p is the cathodic or anodic peak current from the CV curve (A), *n* is the number of electrons transferred in the redox event, *A* is the electrode area (cm^2), *D is the* diffusion coefficient (cm2 s-1), C is the bulk concentration of NMC811 (mol cm-3), and *v* is the scan rate ($V\ s^{-1}$). *D* was 4.2×10^{-6} and 2.8×10^{-6} $cm^2\ s^{-1}$ for the cathodic and anodic reactions respectively for DIT-C, higher than 1.1×10^{-6} and 1.2×10^{-8} $cm^2\ s^{-1}$ for the cathodic and anodic reactions of the SC cathode, respectively. The reduced impedance and enhanced lithium-ion diffusion coefficient explained the higher rate capability for the DIT-C cathode in Figure 3.7.

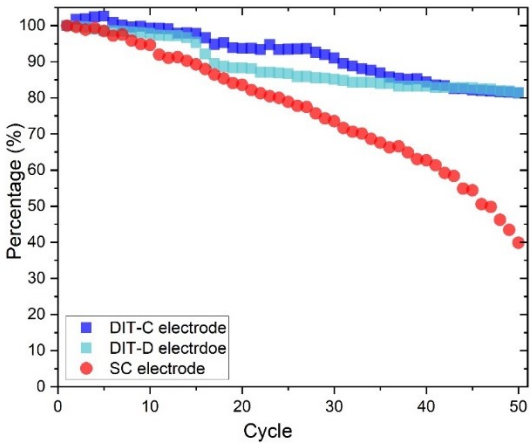


Figure 3.10 Long cycling test of DIT-C, DIT-D and SC electrodes at 2.8 mA cm^{-2} for DIT-C, DIT-D and 1.5 mA cm^{-2} for SC.

Finally, Figure 3.10 shows long cycling performance of the DIT-C cathode, DIT-D (with lower mass loading) cathode and SC (also with lower mass loading) at 0.2 C for 50 times after 70 cycles of rate capability (120 cycles in total). The current of 0.2 C corresponds to (dis)charge current densities of 2.8 and 1.5 mA cm^{-2} for DIT-C and SC, respectively. The DIT-C and DIT-D cathode exhibited higher capacity retention than the SC cathode, confirming enhanced cycling stability and robustness of DIT method. The DIT-C and DIT-D cathodes exhibited

similar capacities towards the end, showing water in the low mass loading scenario did not affect NMC811 with any noticeable changes within the rapid DIT processing window before the electrodes were completely dried through ice sublimation. At the high current density, Li metal anode became the limiting factor instead of the cathode. Our future work will optimise the anode[59].

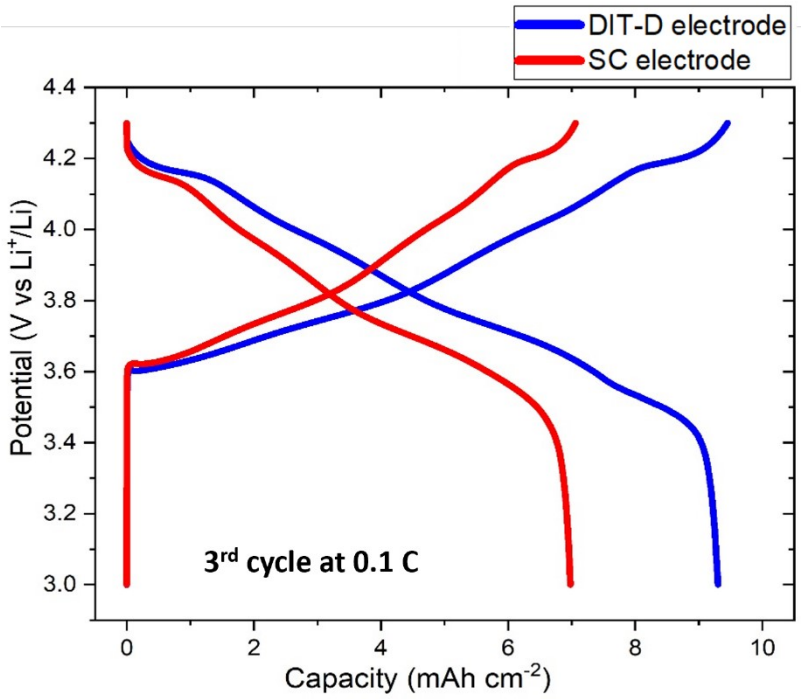


Figure 3.11 Galvanostatic (dis)charge curves for DIT-D and SC electrodes at 0.1 C.

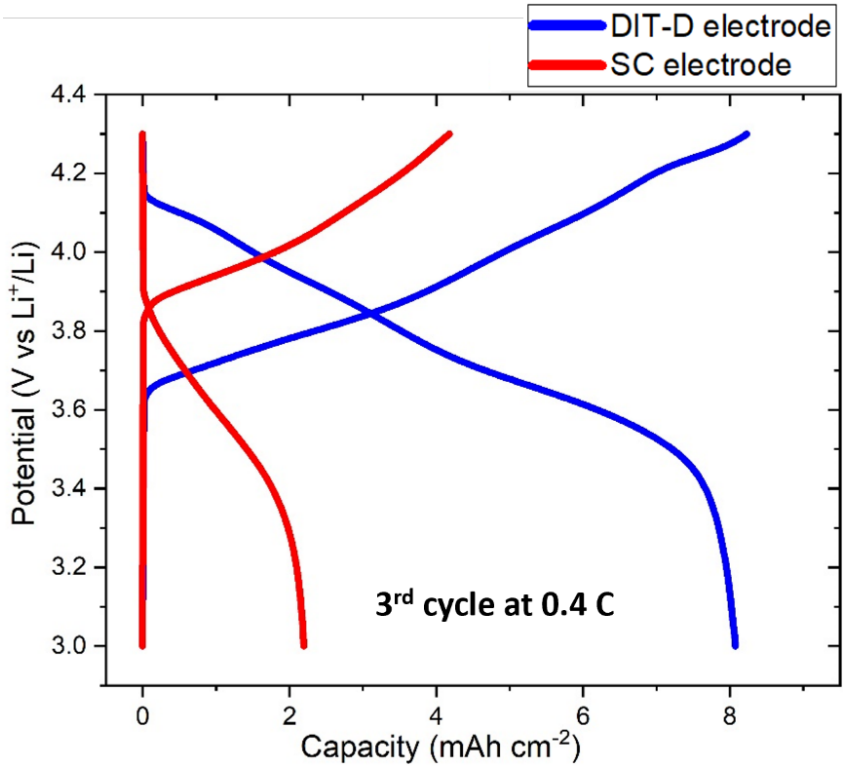


Figure 3.12 Galvanostatic (dis)charge curves for DIT-D and SC electrodes at 0.4 C.

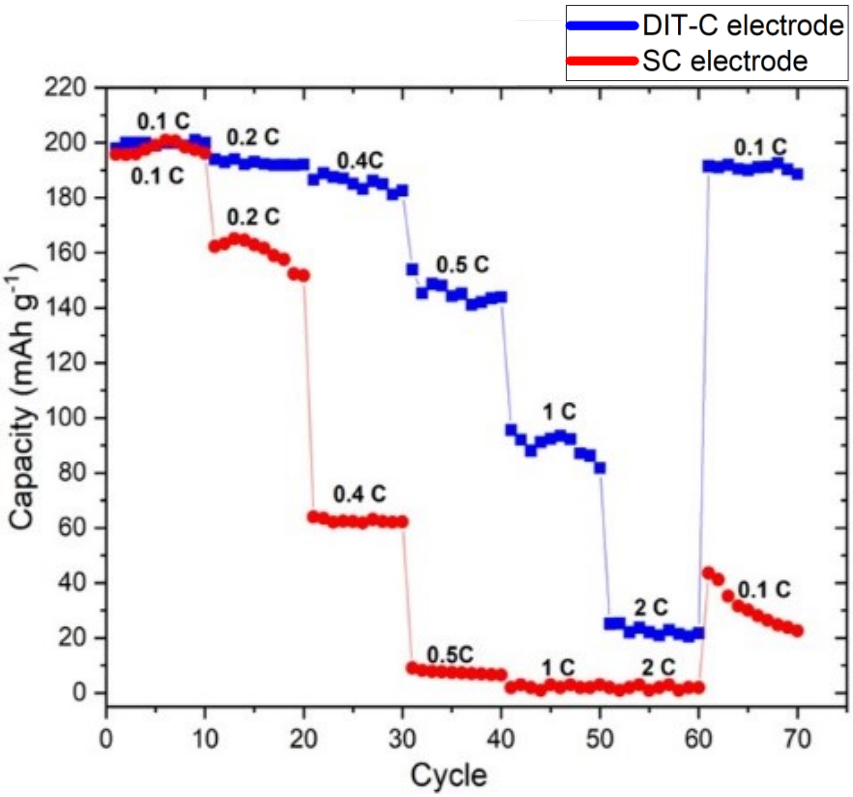


Figure 3.13 Reversible gravimetric capacity of the DIT-C and SC electrodes from 0.1 C to 2 C.

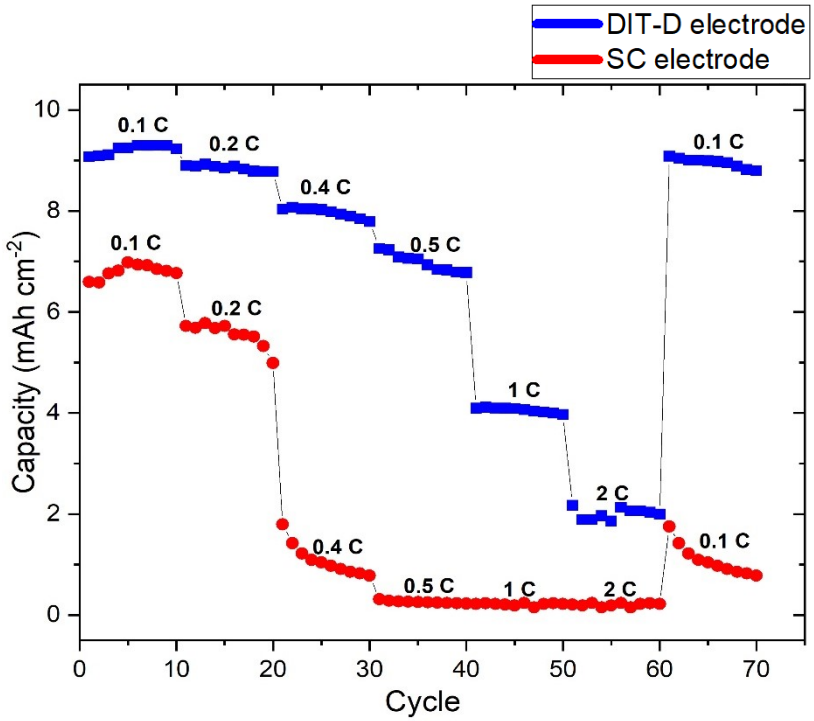


Figure 3.14 Reversible areal capacity of DIT-D and SC electrodes at different C rates.

To investigate the energy storage performance of the structured electrodes in real-world devices, we used a Cell Analysis and Modelling System (CAMS) model[108] to calculate both gravimetric and volumetric energy density of the batteries using the three types of cathodes in a pouch cell configuration. The schematic diagram of SC and DIT-C pouch cell configurations (31.9 cm (L) x 23.2 cm (W)) of approximately the same total volume is shown in Figure 3.15a. For the SC electrode cell stack in this study (340 µm, deliberately made thicker to compare ion diffusion with the DIT electrodes), 12 layers of cathode and 12 layers of anode were used, whereas an 8-layer configuration was used for the DIT-C electrode (660 µm). Figure 3.15b shows the volume contributions of each component in SC and DIT-C-based pouch cell stacks. In addition, a 5.5 layer-configuration was used for the DIT-D electrode (1074 µm), and a 16.6 layer-configuration was used for the conventional SC electrode from the literature (160 µm), to keep the total volume of the pouch cells approximately the same. Table 3.2 shows the properties of the other components inside the pouch cells including copper foil with connecting tab, graphite anode, separator and aluminium foil with connecting tab while Table 3.3 shows

the proportions of these components inside the cell stacks in a pouch cell for real world applications. Figure 3.15 shows directly that as the DIT electrode thickness increased (with vertically aligned pore arrays to speed up ion diffusion in thick electrodes), the proportion of active materials in cell stacks, and hence the battery energy density increased. Table 3.1 summarizes the gravimetric and volumetric energy densities of the 4 types of electrodes (DIT-C, DIT-D, SC in this study and SC in literature) at different C rates. As shown in Figure 3.10(b), The DIT-C cell contained 68.85% active materials by volume, compared to 53.33 % in the SC cell. This represents a 15.52% increase in the volumetric allocation for active materials in the DIT-C cell within the same total volume. Consequently, as shown in Table 3.3, the DIT-C electrode stack contains only 5.07% inactive components, compared to 7.46% in the SC stack. This means the DIT-C stack reduces inactive component usage by 32% than that in the SC cell stacks, contributing to an overall enhancement in the energy density of the battery cell-stack. As a result, DIT-C exhibited a competitive gravimetric energy density of 533.5 Wh kg^{-1}, and 27% higher volumetric energy density of 1162.2 Wh L^{-1} compared with SC in this study and SC from the literature at 0.1 C. However, as soon as the C rate was increased to 0.4 C, DIT-C exhibited 3 times higher gravimetric energy density of 496.2 Wh g^{-1} and over 3 times higher volumetric energy density of 1080.9 Wh L^{-1} than the SC in this study.

Table 3.1 Summary of gravimetric and volumetric energy densities of the cathodes in battery pouch cell configurations.

C rate (h^{-1})	Energy density	Cathode			
		DIT-C	DIT-D	SC (in this study)	SC (from the literature[162])
0.1	Gravimetric (Wh kg^{-1})	533.5	321.1	511.1	464.8
	Volumetric (Wh L^{-1})	1162.2	587.1	1076.5	914.1
0.4	Gravimetric (Wh kg^{-1})	496.2	278.2	163.5	418.3
	Volumetric (Wh L^{-1})	1080.9	510.7	344.5	822.7
Aligned electrode microstructure?		√	√	×	×
Electrode thickness (μm)		660	1074	340	160
Mass loading (mg cm^{-2})		70	70	36	17
Average porosity (%)		35	57	35	35
Pore size (μm)		4 ± 2	6 ± 4	16 ± 14	16 ± 14

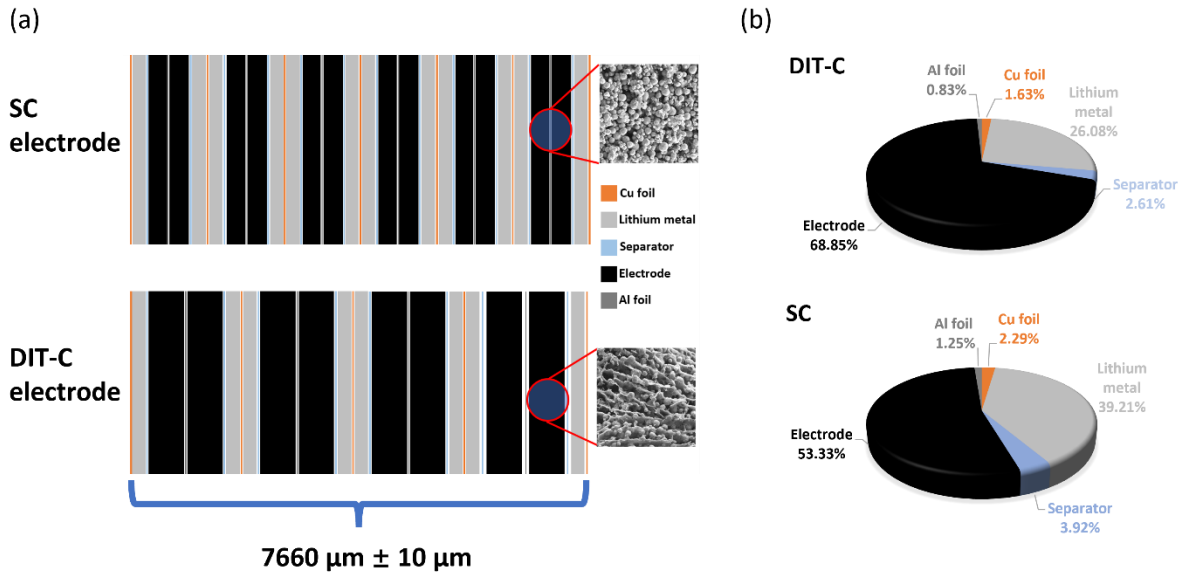


Figure 3.15 (a)A cross section schematic diagram of SC and DIT-C pouch cell configurations with the same total volume and (b) the volume ratio of components in SC and DIT-C pouch cells.

Table 3.2 Details of thickness of each component in pouch cell configurations.

Components	Thickness of each component (µm)			Numbers of components			Thickness (µm)		
	12 layers SC electrode	8 layers DIT-C electrode	5.5 layers DIT-D electrode	12 layers SC electrode	8 layers DIT-C electrode	5.5 layers DIT-D electrode	12 layers SC electrode	8 layers DIT-C electrode	5.5 layers DIT-D electrode
Cu foil with tab	25	25	25	7	5	3.75	175	125	93.75
Lithium metal	250	250	250	12	8	5.5	3000	2000	1375
Separator	25	25	25	12	8	5.5	300	200	137.5
Cathode sheet	340	660	1074	12	8	5.5	4080	5280	5907
Al foil with tab	16	16	16	6	4	2.75	96	64	44
				Total thickness (µm)			**7651**	**7669**	**7558**

Table 3.3 Thickness Distribution of Components in DIT-C vs. SC Cell Stacks

	SC stack	**DIT-C stack**	**Difference trend**
Electrode	53.33%	68.85%	↗
Separator	3.92%	2.61%	↘
Lithium metal	39.21%	26.08%	↘
Al foil	1.25%	0.83%	↘
Cu foil	2.29%	1.63%	↘
Inactive component (Separator, Al and Cu foil)	7.46%	5.07%	↘

3.3 Experimental Section

3.3.1 Fabrication of Electrodes

The slurry utilized in the DIT method was prepared under ambient conditions at a room temperature of 15 °C. To ensure the slurry was homogeneous, the suspension was mixed by a planetary mixer (mixer ARE-250, Thinky company) at a rotation speed of 2,000 rpm for 20 minutes for both the DIT and SC cathodes. For making cathodes by SC, the process commenced with mixing of the NMC811 particles, carbon black, and PVDF binder in the same weight ratio of 90:5:5 in the NMP solvent. The weight ratio between NMP and solid mixture was 50:50[126]. Subsequently, the homogeneous slurry was evenly coated onto a flat aluminium foil (16 μm in thickness) at a coating speed of 5 mm s^{-1}, employing a doctor blade coater (AFA-V, Shanghai Modern instruments). Following this, the coated foil was subjected to preliminary drying in an oven at 80 °C for 50 minutes. The preliminary dried electrode sheet was then transferred to a vacuum oven and exposed to a temperature of 110 °C for 120 minutes to ensure thorough drying[163]. Finally, electrodes with a diameter of 16 mm were precisely cut from the dried electrode sheets using a disc cutter. For DIT, the electrode slurry was rapidly cooled from room temperature down to -40 °C using liquid nitrogen. 30 sets of samples were produced for both DIT and SC cathodes with the mass loading error controlled within 5%.

3.3.2 Characterization

The electrode microstructure was investigated by scanning electron microscopy (SEM, Zeiss Sigma300). Cross-sectional SEM images were taken after the electrode cross section was polished by a fully automated argon ion milling system (PECS II, GATAN) at 8 keV beam for 5 hours to ensure a uniformly flat cross section for subsequent analysis. Segmentation of the cross-sectional SEM images followed by quantification of the phases were used to estimate the electrode porosity. TEM (JEOL STEM 2100 Plus), XPS (K-Alpha), and ToF-SIMS (ION-TOF GmbH, Munster, Germany) depth profiling were used to analyse three types of sample: (i) as-purchased pristine NMC811 particles under ambient conditions without deliberate water

exposure (NMC-ambient conditions); (ii) NMC811 particles that have been immersed in water for 30 minutes (longer than the aqueous slurry mixing duration in the DIT process) (NMC811-30 min); and (iii) NMC811 particles that have been immersed in water for 7 days as a reference for long-term water exposure (NMC-7 days). All the samples were then freeze-dried. To ensure the reliability of these observations, TEM measurements were taken from 10 particles in each sample group, with representative data included in this study. ToF-SIMS data was acquired using a 25 keV Bismuth liquid metal ion gun (LMIG) analytical beam in positive and negative modes. To obtain high resolution mass spectra, high current bunch mode was used with a beam current of 1 pA. For the ToF-SIMS depth profile, all samples were sputtered using a 1 keV cesium (90 nA) dual source column (DSC) ion beam to remove the surface materials layer-by-layer, and the sputter time had a linear relation with the depth using a constant sputter speed of 0.125 nm s^{-1}. The interlaced sputter mode was applied by scanning 100^2 μm^2 field at 128^2 pixels. The XPS measurements (Thermo Scientific K-alpha) were conducted with 35 eV pass energy for high resolution C1s spectra, and Thermo Avantage software was used for data analysis.

3.3.3 Electrochemical Testing

To analyse the electrochemical performance of the electrodes, all types of the electrodes made by DIT and SC were transferred into a glovebox (H_2O level < 0.1 ppm, O_2 level < 0.1 ppm) and assembled and tested in the standard CR2032 coin cell configuration[164][165]. A lithium chip was employed as the counter electrode, lithium hexafluorophosphate solution (1.0 M $LiPF_6$ in ethylene carbonate (EC) and ethyl methyl carbonate (EMC) with 50/50 v/v) was used as the electrolyte[166], a microporous membrane (Celgard 2500) was applied as a separator[167]. Galvanostatic charge and discharge was performed from 3.0 V to 4.3 V at different C-rates on a battery cycler (Arbin BT-G-48)[168]. The EIS was investigated from the frequency of 1 MHz to 100 mHz using Biologics SP-240. CV was performed on Biologic SP-

240 at scan rates of 0.1, 0.2 and 0.5 mV s^{-1}. All electrochemical testing was performed at room temperature (15 °C).

3.4 Conclusion

A DIT method is developed for making anisotropic electrode microstructures with aligned, interleaving lamellae of electrode material and pore arrays to provide fast dual electron and ion transport kinetics. In this work, DIT is applied to NMC811 active material for the first time, demonstrating that this technique can be extended from earlier proof-of-concept studies to a commercially relevant cathode chemistry. This aqueous DIT method eliminates the toxic, combustible, organic solvent NMP and is more sustainable and safer than the conventional SC method. DIT also enables modification of the fabricated electrode microstructure to improve electrochemical energy storage performance, particularly at faster (dis)charge rates. By controlling the DIT processing, the results of a range of surface-sensitive techniques (TEM, ToF-SIMS, XPS) show that the properties of the NMC811 particle surface were similar to that of pristine NMC811 particles in ambient environment and no significant electrochemical performance degradation was observed, demonstrating that water can serve as a viable alternative to NMP in the rapid DIT method. This significantly reduces the environmental impact and health risks associated with the use of NMP, thereby enhancing the sustainability of the battery manufacturing process. We also systematically reduced the porosity of the DIT electrodes to 35%, compatible with the conventional SC electrodes. Due to the almost doubling of the mass loading of the DIT electrodes with the designed microstructure compared with the SC electrode, the DIT-C electrode exhibited 3 times higher gravimetric capacity and 5 times higher areal capacity than the SC electrode at a (dis)charge current density of 5.7 mA cm^{-2}. CV and EIS measurements also show an improved ion diffusion coefficient and reduced impedance for the DIT-C electrode. Finally, the pouch cell configuration of DIT-C electrode exhibited superior gravimetric and volumetric energy densities of 496.2 Wh kg^{-1} and 1080.9 Wh L^{-1} at

5.7 mA cm^{-2} compared with 163.5 Wh kg^{-1} and 344.5 Wh L^{-1} for the SC electrodes, with approximately the same total pouch cell volume. This is because the aligned microstructure improves dual electron and lithium-ion transport kinetics during (dis)charging and discharging, while the higher thickness and mass loading reduce the proportion of inactive components (copper foil, aluminium foil, etc.) and increase the active components by 15.52% in the finite volume of pouch cells.

Chapter 4

4 Fabrication Method of Directional Microstructure for High Energy Density, High Power Battery Cathodes

4.1 Introduction

The conventional slurry coating method of making battery electrodes can only make congested microstructure with randomly distributed active materials particles[169], resulting in highly tortuous and inefficient ion transport pathways[170]. Conventional slurry coating has electrode thickness limitations of up to ~300 μm because the subsequent isotropic heating to evaporate solvent imposes capillary forces that cause electrode cracking[171][172]. Existing slurry coating of electrodes (particularly cathode materials such as NMC811) uses combustible, toxic organic solvent NMP which has safety hazards. Previous results show that prolonged exposure (~28 days) of NMC811 to moisture can lead to the formation of undesirable side products that may compromise electrode performance[58][27].

DIT uses extreme unidirectional supercooling of aqueous electrode slurry to form vertical ice columns. After ice sublimation, the electrodes contain microstructure with vertically aligned pore arrays. The unique vertical microstructure significantly reduces tortuosity[174], thereby shortening lithium ion diffusion pathways[175]. As a result, the DIT-structured electrode facilitates more efficient ion transport with minimal restriction, enabling high current density fast charging/discharging performance. The DIT method overcomes the thickness limitations of conventional slurry coating and enables fabrication of ultra-thick (~1000 μm) electrodes with high mass loading (≥70 mg cm^{-2}) without cracking as ice is directly sublimed to vapour. We have used ToF-SIMS, XPS and high-resolution transmission electron microscopy (HRTEM) to study the chemical composition, chemical bonding, and morphology of the high energy NMC811 particle surface during aqueous processing and identified the optimal aqueous manufacturing conditions for the NMC811 cathode material. This work complements other reports on aqueous processing, e.g. solving the gelation issue of NMC811 slurry[176], and has the potential for eliminating the organic NMP solvent to develop lower cost, more sustainable

battery manufacturing[177]. However, in our previous study[173][174], the DIT method was limited to small-scale electrode fabrication due to mould constraints, with a maximum diameter of 6.5 mm. To overcome the scaling limitations, here, we develop new manufacturing equipment that enables the DIT method to produce electrode sheets of customizable dimensions. This system maintains the fundamental DIT working principle while eliminating previous size constraints, allowing for industrial-scale applications such as pouch or cylindrical cell production[178].

The calendering process followed by slurry coating is also one of the major steps in electrode manufacturing for batteries[179]. This process involves applying compression towards electrodes usually by using a pair of rollers, resulting in electrode densification. The calendering step reduces electrode porosity to increase electrode density and volumetric capacity[180] and improves contact between particles to improve electrical conductivity and maintains mechanical integrity[181][182]. The electrodes made by the DIT method are usually not calendered[183], to protect the vertically aligned microstructure. Excessive compression and thickness reduction can lead to increased pore tortuosity and counteract the benefits of fast ion diffusion of the DIT electrode microstructure[184][185]. On the other hand, one common disadvantage of the DIT electrodes is high porosity and lower volumetric capacity although the gravimetric capacity and rate capability are attractive[183]. The balance between calendering to increase electrode density and deviation extent of the aligned microstructure is unknown but critical for the DIT processing[186][187][188]. Here, we systematically study for the first time the effects of the calendering process with different levels of thickness reduction on the anisotropic microstructure and electrochemical performance of the electrodes made by the DIT method. The goal is to identify the optimal thickness reduction ratio and compression degree

that maximises volumetric and gravimetric energy densities while balancing pore tortuosity to achieve fast (dis)charging rate capabilities.

This study makes two major contributions to the development of the DIT method of engineering battery electrode microstructure. Firstly, we develop a processing instrument to scale up DIT processing from lab scale to a larger production scale while maintaining high reproducibility. The instrument is based on a commercial coater to make the new DIT technology compatible to the existing battery manufacturing process. Secondly, we add the calendering step in DIT manufacturing for the first time to solve the long-standing challenge of high porosity in the electrodes made by DIT or other template-based techniques. Our electrochemical testing results show that 30% calendered DIT electrodes (i.e. reducing electrode thickness by 30% through compression) offer an optimal balance between increasing electrode density and maintaining a level of the anisotropic microstructure for improving lithium-ion diffusion kinetics. The 30% calendered DIT electrodes exhibit high gravimetric and areal capacities (200 mAh g^{-1} and 14 mAh cm^{-2}) at 0.1 C (current density 1.4 mA cm^{-2}), approximately 7 times higher than the conventional slurry coated electrodes of the same material[189] due to the high mass loading of the DIT electrode. Notably, when the current density increases to 7 mA cm^{-2}, the results identified the critical threshold of 30 % calendered electrode that exhibited the highest volumetric capacity of 148 mAh cm^{-3} and the highest volumetric energy density of 778.9 Wh L^{-1} among all other calendering condition electrodes and with similar porosity as those of conventional slurry coated electrodes. These results indicate the porosity and pore tortuosity remain within the favourable range for ion diffusion while the electrode density and volumetric performance are significantly improved at 30% calendering.

4.2 Results and Discussion

4.2.1 Fabrication of Electrodes by Scaled-up Directional Ice Templating (DIT)

Figure 4.1 is a schematic of the scaled-up DIT instrument. In this study, electrode slurry was prepared by combining 90 wt% NMC811 powder (active material), 5 wt% carbon black (conductive additive), 3 wt% SBR, and 2 wt% CMC as binders, with deionized water as the solvent in a 1:1 wt% ratio to the total solid content under ambient conditions[190][191][192]. The mixture underwent preliminary mixing at 500 rpm for 5 minutes, followed by mixing at 2,000 rpm for 20 minutes using a planetary mixer to ensure homogeneity[193]. The well-mixed slurry was cast by a doctor blade machine onto an aluminium plate positioned on top of a Peltier cooling device[194] which was added to the commercial doctor blade machine to obtain the new function of directional freezing. The casting speed was controlled at 5 mm s^{-1}. The Peltier device, when powered by an electrical source, transfers cooling from its cold side to its hot side, creating a temperature difference of approximately 60 °C between the two surfaces[195]. To maintain effective cooling, it is essential to dissipate heat from the hot side efficiently[196]. In this setup, the heat dissipation plate is attached to the hot side of the Peltier device, with inlet and outlet connections linking to a water-cooling module. Upon connection to the power supply, the Peltier device cools the aluminium plate to approximately -40 °C, leading to freezing of the electrode slurry. Simultaneously, a pump circulates cold water through the cooling module, ensuring rapid heat removal from the hot side and sustaining the desired low temperature on the cold side. This efficient cooling setup rapidly freezes the electrode slurry during processing.

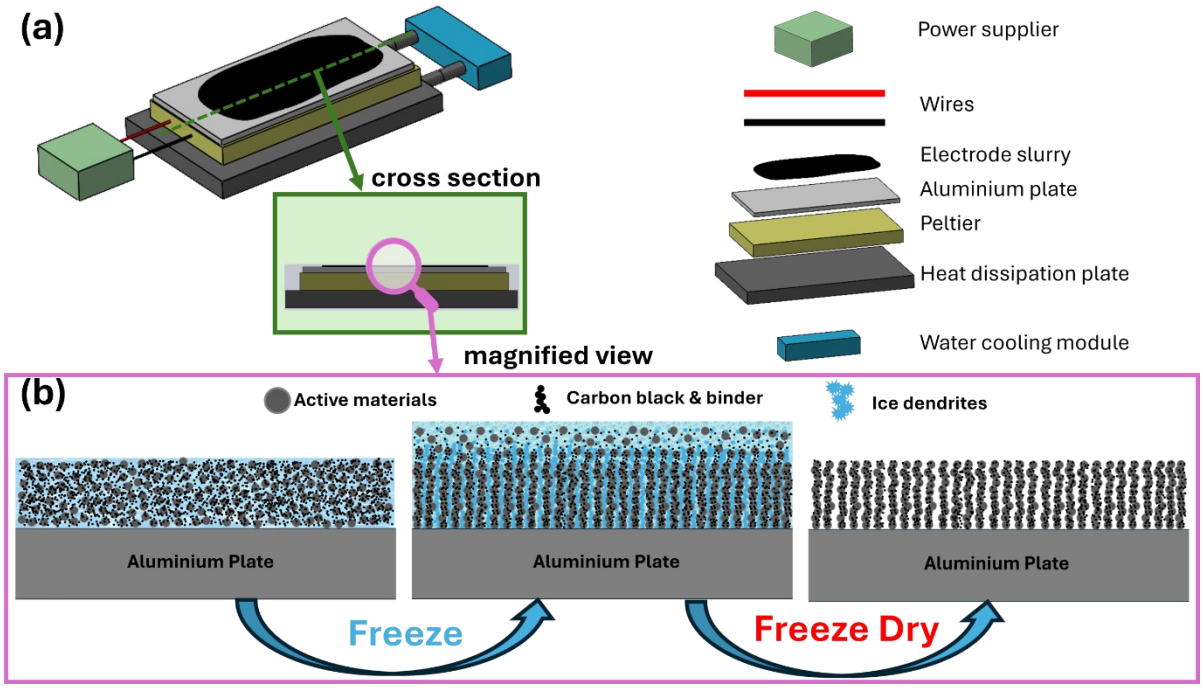


Figure 4.1 Schematics of (a) the directional-ice-templating (DIT) scaled-up apparatus; and (b) the DIT process.

Immediately after the electrode slurry is cast onto the aluminium plate, the active material (NMC811), conductive additives (carbon black), and binders (SBR and CMC) are uniformly but randomly distributed throughout the slurry. As illustrated in Figure 4.1b, the NMC811 particles are dispersed in the liquid medium and surrounded by carbon black and binder prior to freezing. At this stage, the deionized water remains in the liquid phase, corresponding to Status 1 in the water phase diagram (Figure 1.6). Once the Peltier device is activated, the aluminium plate rapidly cools, initiating directional freezing from the bottom to the top of the slurry. This results in the formation of ice dendrites that grow upward through the slurry[197]. As these dendrites form, they expel the materials particles into the interstitial spaces between the growing ice dendrites, as shown in Figure 4.1b[198]. During this process, the water transitions from Status 1 (liquid) to Status 2 (solid) as depicted in Figure 1.6. After complete freezing, the aluminium plate and frozen slurry are immediately transferred to a freeze dryer. The freeze-drying process is carried out at -40 °C and 10 Pa (Status 3 in Figure 1.6). The ice dendrites sublimate directly from solid to vapour, bypassing the liquid phase. This sublimation

process preserves the vertically aligned architecture formed by the expelled particles, resulting in a unidirectional porous electrode structure shown in Figure 4.1b. After the freeze-drying process, the freeze dryer environment is set to 15°C and 10 Pa to allow the aluminium plate to reach room temperature. This step prevents excessive moisture H_2O absorption from the ambient air. Finally, the electrodes are calendered by rolling press machine to varying degrees that result in different thickness reduction: 50%, 40%, 30%, 20%, and 0%. For instance, a 20% thickness reduction applied to an electrode with an initial thickness of 1000 μm yields a final thickness of 800 μm. The dried electrode sheets are typically 5 cm x 10 cm in size, the average mass loading is 70 ± 1 mg cm^{-2}.

4.2.2 Compositional Uniformity of Scaled-up DIT Electrodes

Figure 4.3a shows the scaled-up free-standing electrode sheet made by the upgraded DIT instrument, the sheet appeared uniform and intact, indicating good mechanical robustness and structural integrity. To evaluate the compositional uniformity of the scaled-up free-standing DIT electrode sheets, TGA analysis was carried out on five representative regions using a five-point sampling method. These sampling locations were selected to cover the centre and edges of the sheet so that any variation in material composition across the large area could be captured. The exact positions of the five points are labelled in Figure 4.3a. From each region, approximately 10 mg of electrode material was collected, ensuring consistent sample mass and preparation. All samples were tested under identical TGA conditions to allow direct comparison of their thermal decomposition behaviour. This approach makes it possible to assess whether the distribution of active material, conductive additive and binder remains uniform throughout the entire DIT-produced sheet. The raw data was normalized to 100 % at 65 °C to eliminate the influence of moisture content from the ambient environment and gas fluctuations at the start of the experiment. As shown in Figure 4.2, all five TGA curves exhibit nearly similar decomposition trend, indicative of consistent compositions across the 5 points. Obvious mass

loss was observed at 200 °C and 280 °C, corresponding to the decomposition of the SBR and CMC binder. At 400 °C, the carbon black contributed to the rapid mass loss and all samples stabilized at approximately 90 wt% residual mass with variations within 0.5 wt% which was aligned with the expected 90 wt% content of NMC811 active material. Areal composition stability is critical for industrial-scale manufacturing. At the lab scale, electrodes are typically characterized by assembling them into coin cells and performing galvanostatic (dis)charge cycling. Uniform active material mass across the electrode sheets and consistent electrochemical performance of the same batch coin cells is essential for performance evaluation and comparisons among different electrode batches. At the industrial scale, non-uniform distributions of active materials can result in significant issues, including poor cell performance and safety concerns[200][201]. Heterogeneity in active material loading on the electrode sheets may lead to localized overloading of current, and consequently exceeding resistance and generating hotspots which increases the pressure on heat dissipation[202][203]. In this study, the TGA results of five different regions on the electrode sheets revealed nearly identical composition profiles and residual mass values. This confirms a uniform distribution of active and inactive materials across the whole DIT scaled-up electrode sheets. The consistency reveals stability and reproducibility of the scaled-up DIT method and demonstrates its possibility of producing large-area electrodes with homogeneous compositions[204][205].

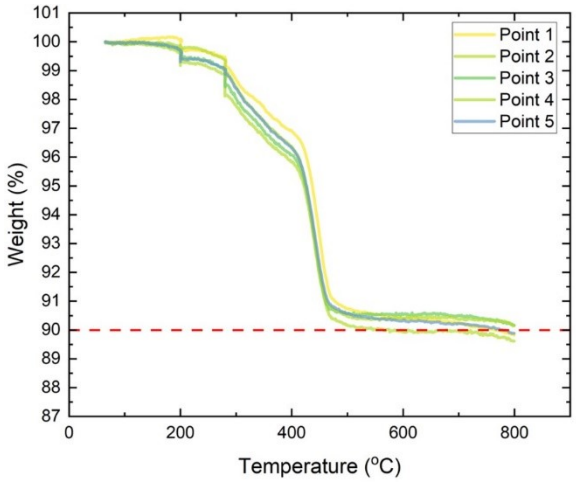


Figure 4.2 TGA curves from five representative points across the scaled-up DIT electrode sheet.

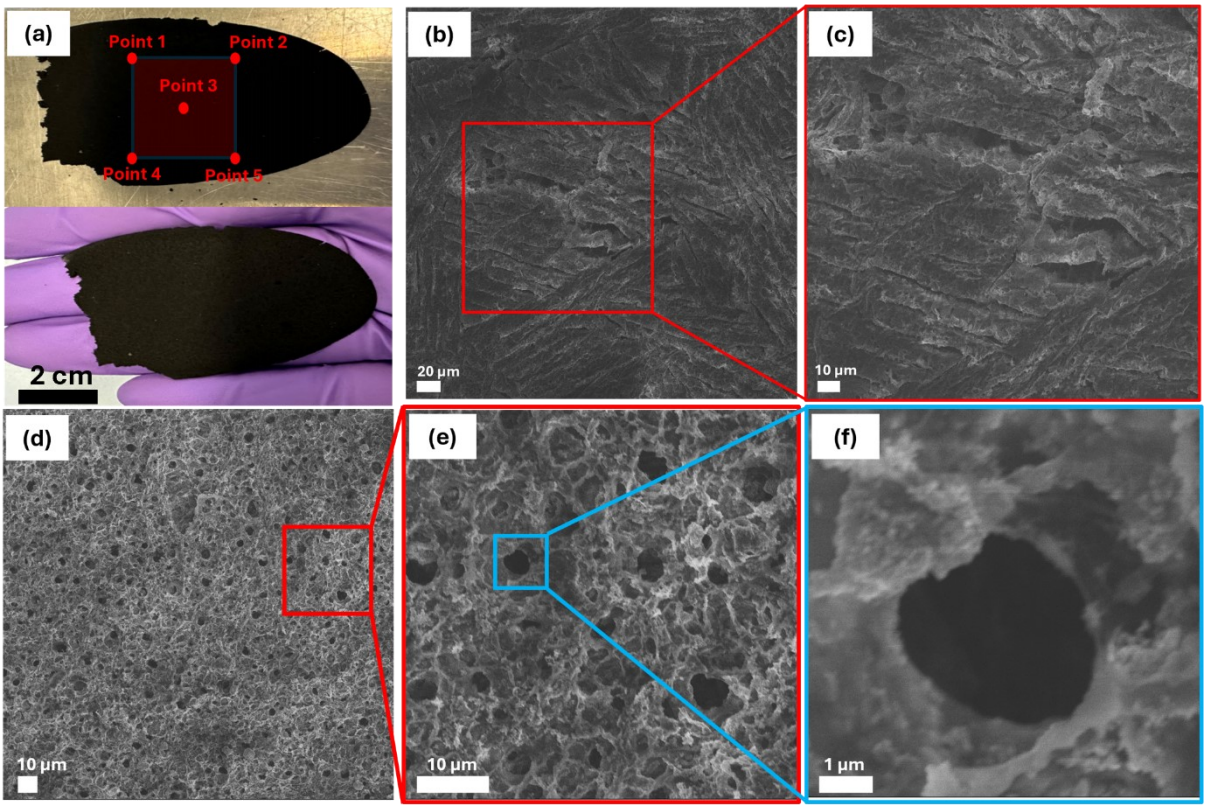


Figure 4.3 (a) Photo of free-standing NMC811 electrode sheet fabricated by the scaled-up DIT method. Scanning electron microscopy (SEM) images of (b) DIT electrode top surface and (c) its magnified view; (d) DIT electrode bottom surface and (e,f) its magnified views.

4.2.3 Electrode Microstructure

To investigate the microstructure of the DIT electrodes, SEM was conducted on both the top and bottom surface of the electrodes, as shown in Figure 4.3b-f. The bottom surface of the free-standing electrode is the supercooling interface in contact with the aluminium plate and nearest to the cooling device, showing homogeneously distributed porous microstructure with nearly

uniform small size pore diameters of 400 nm - 2 μm (Figure 4.3d-f). The bottom surface is the starting point of the freezing direction, ice crystals start to nucleate at this interface. The ice nucleation rate is high whereas the temperature gradient is low at this interface, resulting in more equiaxed ice structures[206]. The ice then starts to grow vertically upwards. The freezing temperature gradually increases from the bottom to the top surface through the electrode thickness as the ice needs to travel longer distances through the electrode materials. The top surface (Figure 4.3b) exhibits distinctly different morphology of aligned lamellar structures, a magnified view (Figure 4.3c) reveals well-defined interlamellar gaps ranging from 1 to 10 μm. These features arise from the directional growth of ice dendrites where the temperature gradient starts to become larger, and the diameter of the ice dendrites increases towards the top as ice has more time to grow, showing the unidirectional ice dendrite growth kinetics during the DIT process.

To reveal the internal microstructure of the electrodes, argon ion milling was used to gently polish the cross section of the electrodes. Figure 4.4 presents cross-sectional SEM images of the as-fabricated DIT electrodes and the DIT electrodes after varying degrees of calendering. During calendaring, the electrode is compressed between two rollers that exert a load normal to the electrode surface. This vertical compressive force reduces the electrode thickness and partially modifies the pore alignment within the DIT structure. The direction of this applied load is shown by the arrow in Figure 4.4. The cross-sectional SEM image of the as-fabricated electrode (Figure 4.4a) reveals a vertically aligned microstructure with pore arrays traversing uniformly throughout the electrode full 1000 μm thickness. At 20-30% calendering (Figure 4.4b,c), the overall alignment was largely retained, although localized deformation of the channels became apparent. The porosity was reduced from 46% for 20% calendering to 38% for 30% calendering. With further calendering to 40% (Figure 4.4d), the porosity was reduced

to 35%, but the porous channels were increasingly compressed and narrowed, leading to partial loss of structural integrity. At the highest calendering level of 50% (Figure 4.4e), the porosity was reduced to 30%, but the electrode morphology became significantly compressed, with the original aligned structure heavily distorted and the porosity substantially reduced. Some of the aligned structures appeared broken in the middle, which may obstruct ion diffusion pathways and hinder effective transport during charging and discharging. These images reveal electrode morphological evolution during calendering, the morphological transition reflects the mechanical response of the vertical structure under compression.

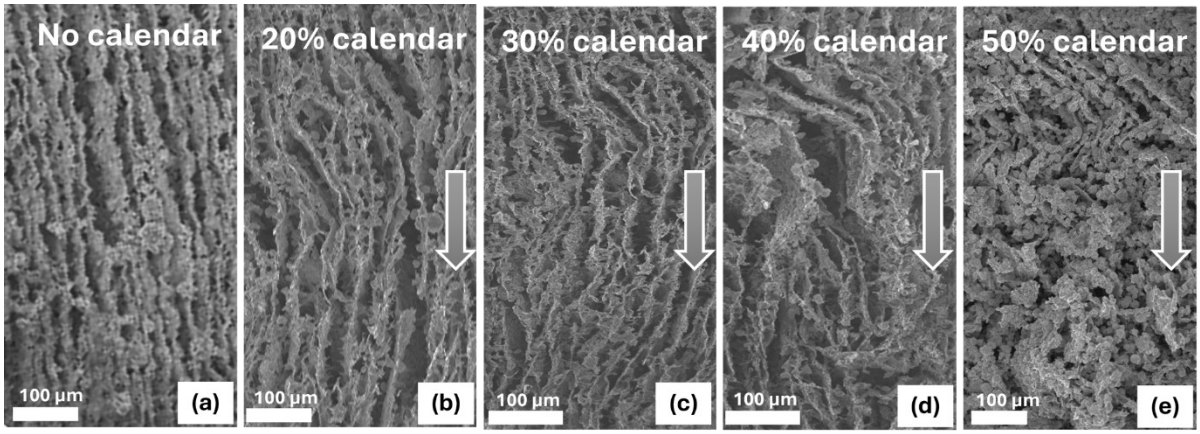


Figure 4.4 Cross-sectional SEM images of the as-fabricated scaled-up DIT electrode and under subsequent varying degrees of calendering.

4.2.4 Electrochemical Performance

The galvanostatic (dis)charge curves in Figure 4.5a,b indicate all electrodes, regardless of the calendering level, exhibited similar specific capacities (approximately 200 mAh g^{-1}) and areal capacities (approximately 14 mAh cm^{-2}) at 0.1 C rate (1.4 mA cm^{-2}), indicating comparable initial active material utilization. All electrodes showed high coulombic efficiency (higher than 98%), indicating stable and reversible electrochemical behaviour. The galvanostatic (dis)charge curves of the electrodes under varying calendering at 0.2 and 0.5 C are shown in Figure 4.6. Although the C rates appear low, this is because the DIT electrodes in this work have an exceptionally high average mass loading of 70 mg cm^{-2} compared with up to 10 mg cm^{-2} mass loading in other studies (e.g. [207]). Therefore, the actual current used for charging

and discharging of the battery cells in this study is approximately 7 times higher than the current used in other studies under the same C rate[207]. Beyond 1 C in this study (14 mA cm^{-2}), the current magnitude became too large that lithium plating on the anode side became the limiting factor, not the cathode[207]. As the C rate increased to 0.2 C (2.8 mA cm^{-2}), all the other electrodes maintained ~190 mAh g^{-1} and higher than 13.0 mAh cm^{-2} whereas the 50% calendered electrode exhibited the largest capacity loss, delivering a specific capacity of 181 mAh g^{-1} and an areal capacity of 12.6 mAh cm^{-2}. At 0.5 C (6.0 mA cm^{-2}), the 20% and 30% calendered electrodes retained higher capacities (approximately 139 mAh g^{-1} and 9.7 mAh cm^{-2}), the 40% electrode delivered 111 mAh g^{-1} and 8.5 mAh cm^{-2}, whereas the 50% sample again showed the most pronounced decline (around 100 mAh g^{-1}, 6.9 mAh cm^{-2}).

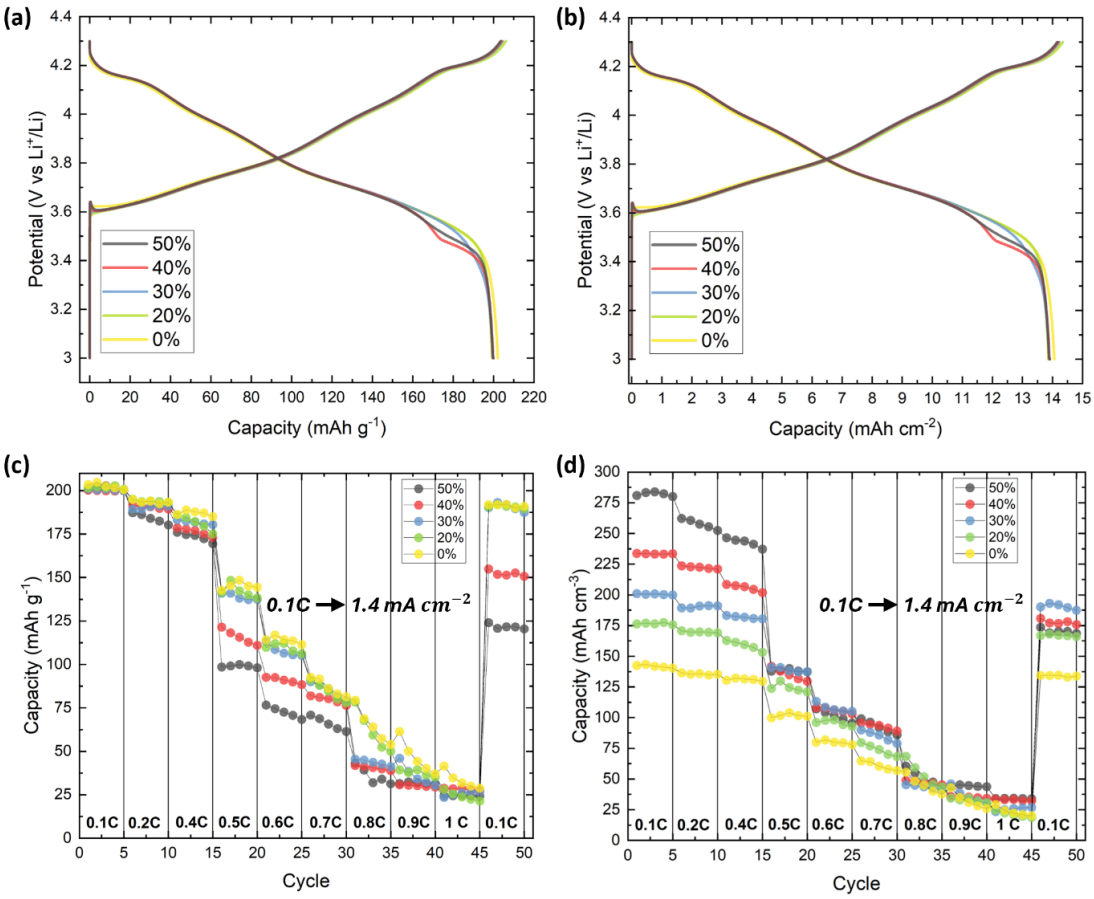


Figure 4.5 Galvanostatic (dis)charge curves of the scaled-up DIT NMC811 electrodes under varying calendering degrees at 0.1 C, showing (a) gravimetric capacities; and (b) areal capacities. Rate capability of the same electrodes, showing (a) gravimetric capacities; and (d) volumetric capacities.

Figure 4.5b,c show rate capability in terms of both gravimetric and volumetric capacities as C rate increased for the electrodes under varying degrees of calendering, even the lowest 0.1 C rate already used a high current density of 1.4 mA cm^{-2}. All electrodes were tested under increasing C rates from 0.1 to 1 C, followed by a return to 0.1 C. Figure 4.7 also shows rate capability in terms of areal capacities for analysing different performance metrics. As the C rate increased, a decline in capacity could not be avoided for all electrodes as there was less time for (dis)charging, however, notable differences emerged among the electrodes with the different calendering levels. At ≥50% calendering, the electrode exhibited a pronounced capacity drop, particularly at ≥0.5 C (7 mA cm^{-2}), likely because the over-compression increased pore tortuosity and hindered ionic transport. In contrast, the 30% calendered electrode consistently delivered among the highest gravimetric, areal and volumetric capacities at ≥0.5 C among all the electrodes, indicating a more favourable balance between high electrode density and low pore porosity. On the other hand, although the 0% and 20% calendered electrodes showed slightly better gravimetric capacity (~12 mAh g^{-1}, 8% of the total gravimetric capacity) and area capacity (~0.7 mAh cm^{-2}, 7% of the total areal capacity) at 0.5 C, these electrodes lacked sufficient high density, resulting in much lower volumetric capacities (~37 mAh cm^{-3}, 27% of the total volumetric capacity). Hence, the 30% calendering condition presents an optimal trade-off between rate capability and all the different capacity performance metrics. When the C rate returned to 0.1 C in the final step of the rate capability testing, the capacity recovery was also the highest for the 30% calendered electrodes, indicating the aligned microstructure was maintained with reversible electrochemical behaviour.

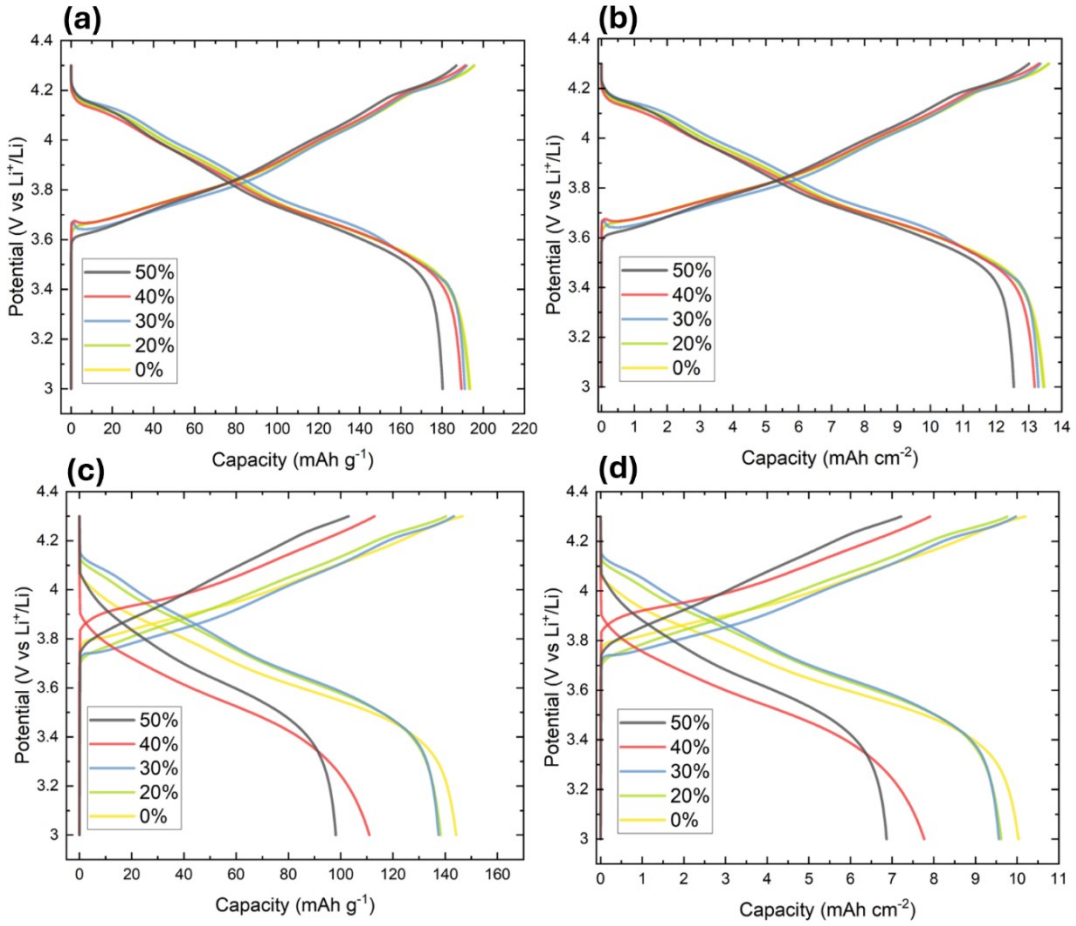


Figure 4.6 Galvanostatic (dis)charge curves of the scaled-up DIT NMC811 electrodes under varying calendering levels at (a,b) 0.2 and (c,d) 0.5 C, showing gravimetric and areal capacities.

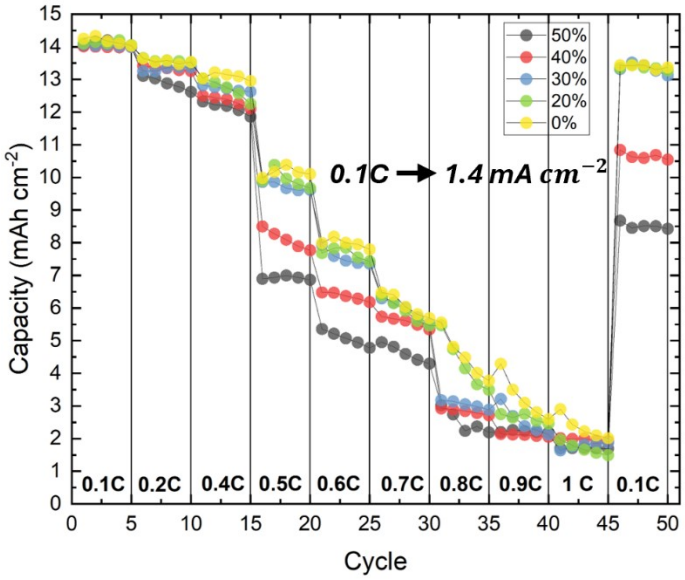


Figure 4.7 Rate capability of the DIT NMC811 electrodes under varying calendering levels, showing areal capacities.

To determine the lithium ion diffusion value of the best-performing 30% calendered electrode and compare with the 0% calendered electrode, their experimental CV curves and the fitted peak current/root of scan rate linear relations are shown in Figure 4.8. For the 30% calendered electrode, the anodic and cathodic peak currents were 1.48 mA and 0.96 mA, respectively. For the 0% calendered electrode, the anodic and cathodic peak currents were 1.54 mA and 0.95 mA, respectively. The fitted linear relations shown in Figure 4.8b,d confirms that the redox process was diffusion-limited and reversible in both electrodes. To estimate lithium ion diffusion coefficient *D*, Randles-Sevcik equation[160] [161]was applied.

$$i_p = 2.686 \times 10^5 \times n^{\frac{3}{2}} \times A \times D^{\frac{1}{2}} \times C \times v^{\frac{1}{2}} \quad \text{(Equation 4.1)}$$

Where i_p is the anodic or cathodic peak current obtained from CV curve (A), n is the number of electrons transferred in the redox event, A is the electrode surface area (cm^2), D is the diffusion coefficient ($cm^2\ s^{-1}$), C is the bulk concentration of NMC811 ($mol\ cm^{-3}$), and v is the scan rate ($V\ s^{-1}$). The average D_{Li+} was 2.88×10^{-9} and $3.01 \times 10^{-9}\ cm^2\ s^{-1}$ for the 30% calendered and 0% calendered DIT electrodes, respectively, indicated that both electrodes exhibited similar ionic diffusion behaviour and 30% calendering did not disrupt the fast ion diffusion pathways significantly. However, the 30% calendered electrode exhibited superior benefits in volumetric capacities, and hence, achieved a balance between preserving fast ion transport kinetics and high volumetric performance. Further, both DIT electrodes show significant improvement in lithium-ion diffusion coefficients in other conventional slurry coated NMC811 electrodes with random microstructure where the D_{Li+} values are in the range between 10^{-11} and $10^{-13}\ cm^2\ s^{-1}$ [208].

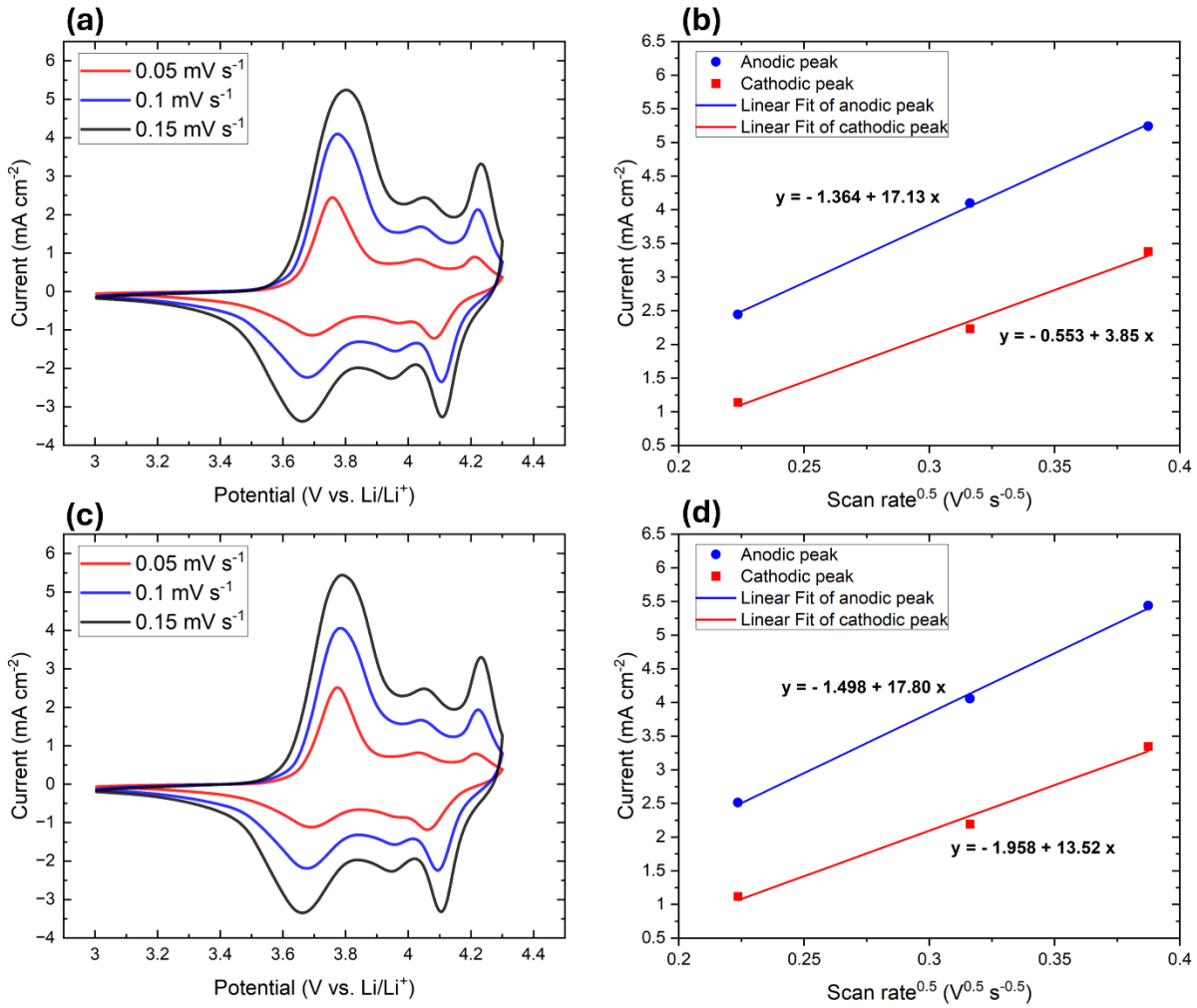


Figure 4.8 Cyclic voltammograms at 0.05 mV s^{-1}, 0.10 mV s^{-1}, 0.15 mV s^{-1} for (a) 30% calendered DIT electrode; and (c) 0% calendered DIT electrode. Fitted linear relations of the peak current in both anodic and cathodic scans against the square root of scan rate for (b) 30% calendered DIT electrode; and (d) 0% calendered DIT electrode.

EIS was performed on the battery cells at the pristine state to evaluate the effect of different calendering degrees on the electrochemical properties of the DIT NMC811 cathodes. A SC electrode (340 μm in thickness) of the same materials was also tested at the same conditions for comparison. The resulting Nyquist plots are shown in Figure 4.9a, the high frequency region is magnified in Figure 4.9b, and the corresponding equivalent circuit model[209] is in the inset of Figure 4.9b. The fitted resistance values are summarized in Table 4.1. The combined electronic resistance of the electrode and the ionic resistance of the electrolyte (Rs) remained relatively stable at ~7 Ω for the DIT electrodes with up to 40% calendering. However, at 50% calendering, Rs increased sharply to 12.8 Ω, likely due to possible cracks under the excessive

pressure. This measurement was consistent with the electrode microstructure from the cross-sectional SEM images in Figure 4.4, where partial structural breakdown was visible at the 50% thickness reduction. At medium to high frequencies, the semicircle in the Nyquist plots represents the combined charge transfer and interfacial resistance (Rct)[173]. The fitted results show that Rct remained low and decreased from 26.2 to 21.6 Ω from 0% to 40% calendering, indicating that both electronic and ionic pathways were well maintained and improved further when the electrodes were calendered up to 40%. However, when the thickness reduction reached 50%, Rct increased to 39.2 Ω.

Nevertheless, Rct for all the DIT electrodes were still significantly lower than 78.4 Ω for the slurry coated electrode, indicating the DIT electrodes reduced ion transfer resistance inside the electrodes in general. At low frequencies, the tail of the Nyquist plots for the DIT 0% - 40% calendered electrodes overlapped and displayed a steeper slope than the DIT 50% calendered electrode, but the slope of the latter was still steeper than the slurry coated electrode, indicating the DIT electrodes with vertically oriented pore arrays with low-tortuosity pathways exhibited faster lithium-ion diffusion. These EIS results correlate well with the galvanostatic (dis)charging curves and rate capabilities in Figure 4.5, where the DIT 50% calendered electrode exhibited reduced rate capability and poorer reversibility.

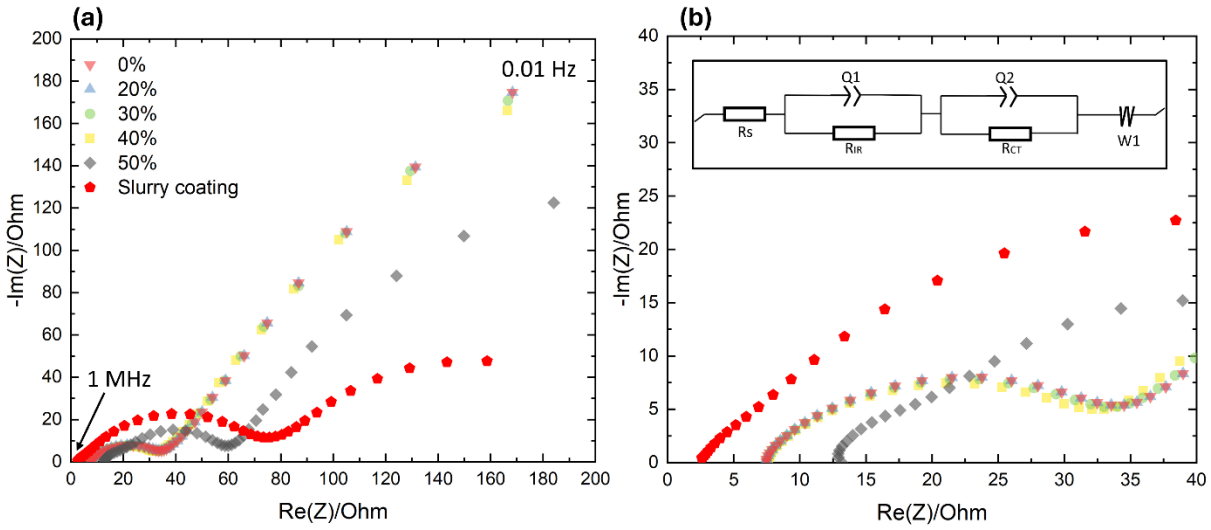


Figure 4.9 (a) Nyquist plots of the DIT NMC811 electrodes at different calendering levels and the conventional slurry coated electrode of the same materials at a frequency range from 1 MHz to 0.01 Hz, all at the pristine state; and (b) magnified high frequency region of the Nyquist plots. The inset of (b) is the equivalent circuit model that was used for fitting the Nyquist plots.

Table 4.1 Fitting resistances of the Nyquist plots of the DIT NMC811 electrodes under different calendering levels and the slurry coated electrode of the same materials as a reference using the equivalent circuit model.

Cathodes	Rs (Ω)	Rct (Ω)
0% calendered	6.9	26.2
20% calendered	6.9	22.7
30% calendered	6.8	22.3
40% calendered	6.8	21.6
50% calendered	12.8	39.2
Slurry coated	3.5	78.4

Figure 4.10 presents the long-term cycling performance of DIT electrodes calendered by varying levels at 0.2 C (current density = 2.8 mA cm^{-2}) over 100 cycles. The electrodes from uncalendered (0%) to moderate calendering levels (20% - 40%) exhibited comparable and stable capacity retention of ~80% after 100 cycles. These results demonstrate that moderate calendering (≤40%) gently bended the vertical structure but largely preserved the beneficial aligned porous microstructure of the DIT electrodes, allowing them to maintain open lithium-

ion transport pathways without significant degradation. The 50% calendered electrodes showed a rapid and continuous capacity decline throughout cycling. This poor performance indicates that excessive calendering severely damaged the DIT electrode microstructure and collapsed the pore channels.

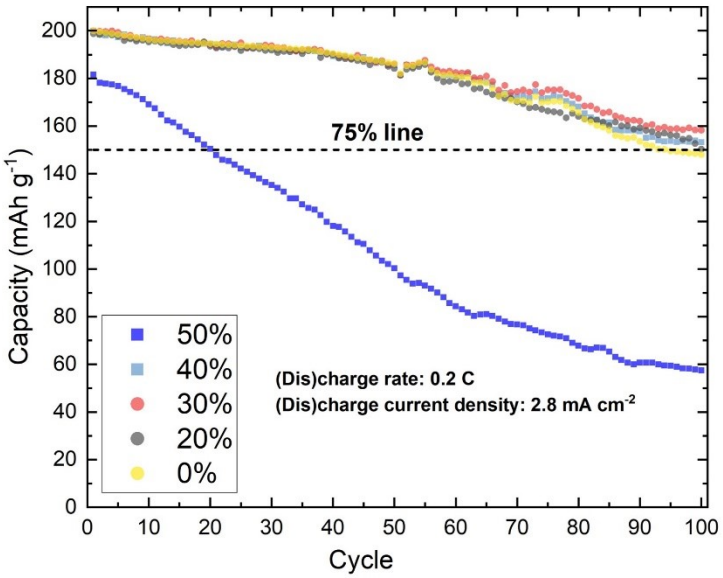


Figure 4.10 Long-term cycling performance of DIT NMC811 electrodes under varying calendering levels at 0.2 C (current density = 2.8 mA cm^{-2}) over 100 cycles.

The gravimetric (Wh kg^{-1}) and volumetric (Wh L^{-1}) energy densities of battery pouch cells (A4 size, 29.7 cm x 21 cm) using the DIT NMC811 cathodes under varying calendering degrees and the conventional slurry coated electrodes of the same materials estimated by the CAMS are summarized and compared in Table 4.2.

Table 4.2 Properties and gravimetric and volumetric energy densities of scaled-up A4 pouch cells containing DIT NMC811 cathodes under varying calendering levels and conventional slurry coated electrodes of the same materials for comparison estimated by the CAMS model.

C rate (h^{-1})	Energy density	Cathodes					
		0% calender	20% calender	30% calender	40% calender	50% calender	Slurry coating
0.1	Gravimetric (Wh kg^{-1})	461. 6	508.7	533.2	545.6	559.9	511.1
	Volumetric (Wh L^{-1})	846.1	1025.4	1133.1	1192.6	1264.9	1076.5
0.2	Gravimetric (Wh kg^{-1})	447.0	491.4	509.2	516.7	504.7	163.5
	Volumetric (Wh L^{-1})	819.5	990.5	1082.1	1129.4	1140.3	344.5
0.5	Gravimetric (Wh kg^{-1})	333.1	351.6	366.5	302.8	274.3	102.2
	Volumetric (Wh L^{-1})	610.6	708.8	778.9	661.9	619.8	215.3
Electrode thickness (µm)		1000	800	700	600	500	340
Mass loading (mg cm^{-2})		70	70	70	70	70	36
Aligned electrode microstructure?		✓	✓	✓	✗	✗	✗
Average porosity (%)		57	46	38	35	30	35
Pore size (µm)		16 ± 14	11 ± 9	8 ± 7	6 ± 4	6 ± 4	16 ± 14

4.3 Experimental Section

4.3.1 Characterization

Electrode morphology was examined using scanning electron microscopy (SEM, Zeiss Sigma300). To prepare the cross section of the electrodes in order to reveal the internal microstructure without damaging/altering the microstructure, a fully automated argon ion milling system (PECS II, GATAN) was employed to gently polish the cross section under an 8 keV beam for 6 hours. This ensured a flat cross-section suitable for accurate SEM focus and imaging. Porosity estimation was carried out using the segmentation function in ImageJ software applied to the SEM cross-sectional images of the electrodes. The Thermogravimetric (TGA) analysis was performed under STA 449 F5 Jupiter simultaneous thermal analyser (Netzsch GmbH, Germany). The obtained date was analysed using Proteus Software ((Netzsch GmbH, Germany). Approximately 10 mg of powder was used in each TGA measurement. A background measurement was conducted for the baseline before the experiment, where a reference crucible with Al_2O_3 and an empty crucible were placed on the balance holder. The purge air flow rate and protective argon flow rate were 50 and 20 ml min^{-1}, respectively. The sample measurements were conducted after baseline correction. In this experiment, the NMC811 electrode material was running under argon between 20 and 280 °C and air flow between 280 and 800 °C with a heating rate 3 °C min^{-1}.

4.3.2 Electrochemical Testing

All electrochemical testing was performed at room temperature at approximately 15 °C. The electrodes were assembled into CR2032-type coin cells in a half-cell configuration, using lithium metal chips as the counter electrode[210]. Electrode discs were carefully punched from the electrode sheets and transferred into an argon-filled glovebox where moisture and oxygen levels were maintained below 0.1 ppm. The electrolyte consisted of 1.0 M lithium

hexafluorophosphate ($LiPF_6$) dissolved in a 1:1 volume ratio mixture of ethylene carbonate (EC) and ethyl methyl carbonate (EMC). A microporous polypropylene membrane (Celgard 2500) was used as the separator. Galvanostatic charge–discharge tests and long-term cycling stability of the electrodes were conducted using a battery cycler (Arbin BT-G-48) within a voltage window of 3.0 V to 4.3 V at various C-rates and current densities to evaluate the electrochemical performance. EIS measurements were performed using a Biologic VSP in the frequency range of 1 MHz to 10 mHz with an amplitude of 10 mV. CV was conducted using a Biologic LBT20084 at scan rates of 0.05, 0.1, and 0.15 mV s^{-1}.

4.4 Conclusion

This study demonstrates the scale-up of the DIT manufacturing technique through directional extreme supercooling for the fabrication of ultra-thick (~1000 μm) battery electrodes using an aqueous solvent. The resulting electrode sheets achieved a high mass loading of 70 mg cm^{-2}, and maintained vertically aligned microstructure that effectively improved fast lithium-ion diffusion kinetics while ensuring good electrical connectivity. An analysis of the calendering process revealed the critical threshold of 30% calendering degree of the DIT electrodes to obtain a balance between maintaining the vertical microstructure essential for efficient ion transport and enhancing volumetric energy density. It was found the 30% calendered DIT NMC811 cathode was the critical threshold that exhibited comparable lithium-ion diffusion coefficient, low impedance, the highest volumetric capacities as the (dis)charging current density increased to 7 mA cm^{-2}, and stable cycling stability. Excessive calendering beyond 40% destroyed the vertically aligned electrode microstructure and caused rapid capacity fade in long term testing. Pouch cell performance estimation showed substantial gravimetric and volumetric energy densities of 367 Wh kg^{-1} and 779 Wh L^{-1} at 7 mA cm^{-2} using the 30% calendered DIT NMC811 cathode compared with 102 Wh kg^{-1} and 215 Wh L^{-1} for conventional SC electrodes of similar porosity. These results validate the feasibility of using the DIT method for

manufacturing-scale production of electrode microstructure engineering to achieve high energy density, fast charging batteries.

Chapter 5

5 Ultra-thick Graphite Anode Vertical Microstructure by Directional Ice Templating

5.1 Introduction

LIBs have become increasingly crucial in the world due to their versatile and efficient energy storage capabilities. LIBs, as a widely used energy storage device also played an important role in automotive industry, consumer electronics and grid energy storage system[211, 212]. Recent research trends and on lithium-ion batteries has been focused on energy density improvement, fast charging technology, longevity and cycle life[213, 214]. Due to the high demand for lithium-ion battery in various industries, a good manufacturing method can significantly impact the performance of lithium-ion battery by optimizing the processes[215]. A lithium-ion battery consists of several key components including a cathode, an anode, a separator, electrolyte and a current collector. Each parts works together to allow lithium ions diffuse and move between cathode and anode thus to store and release electrical energy[216]. Anode, as one of the core elements, can receive and store lithium ions during charge process. When discharging, anode releases lithium ions stored in the active materials and then the lithium ions pass through electrolyte and separator[217]. Graphite has gain significant attention as an anode material for lithium-ion batteries because its high electrical conductivity, good lithium intercalation capacity and relatively low cost[218, 219]. This study focuses on improving the electrochemical performance and energy density of the graphite anode by optimizing the electrode's microstructure.

In conventional anode manufacture method, the slurry is made by mixing graphite powder with binder which create a cohesive and mechanically stable structure and help hold the graphite particles together and adhere them to current collector[220]. Then a doctor blade is used to coat prepared slurry on the copper foil followed by vacuum oven drying and calendar step[221]. The microstructure of the anode made by this method will be random even if the planetary mixing machine is applied during the mixing procedure to make the powder suspended into the solvent homogeneously[222]. The congested particles arrangement and random size

distribution of pores structure prevent the electrode from better electrolyte penetration and ion diffusion[177]. Poor electrolyte penetration limits the contact between the active electrode materials and the electrolyte, leading to a decrease of electrochemical reactions and results in a reduced capacity of the battery[223]. While slow ion diffusion hinders the ability of lithium ions to move into and out of the electrode quickly and result in impaired rate capability of the cell[224]. The most straightforward way to overcome this situation is reducing the thickness of electrode which may improve electrolyte penetration and increase lithium-ion utilization in electrodes. However, the thickness reduction to electrode causes the decreased proportion of active materials in a cell which consequently decrease the energy density from the perspective of the entire battery[225]. Many studies aim to overcome the ion diffusion problem without reducing the energy density of a cell by developing new active materials and applying additives to battery components and less attention falls on the manufacturing process[226][227][228][229].

To enhance the ion diffusion kinetics and improve tortuosity in anode during charging and discharging, a new method called DIT method is applied in anode production process[230]. By using DIT method, the resulting reduction in tortuosity enhances the C-rate capability and conductivity of the anodes, addressing one of the critical limitations associated with traditional thick electrodes[231]. With the aim of proving the feasibility and reliability of DIT method in anode graphite production, the comparative experiment between graphite anode microstructure as well as electrochemical performance made by conventional SC method and new DIT method is implemented and repeated. Conventional SC method involves mixing the ingredients of anode, coating slurry on cooper foil and then subjecting the slurry to an oven drying process to remove moisture[232]. This is followed by vacuum oven drying to further ensure dryness which often results in challenges related to the microstructure and integrity of the electrodes when fabricating thick electrode[233]. Finally, the dried mixture is cut and assembled into coin

cell. In DIT method, the procedure begins with mixing and coating, but instead of oven drying, the mixture is subjected to freezing. After freezing, it undergoes a freeze-drying process to remove the moisture before being assembled. Comparatively, conventional SC primarily utilizes heat-based drying methods, while DIT method incorporates freezing and freeze-drying techniques. Neither of these two methods include calendaring process. The freeze-drying process enabled the production of thick electrodes (over 1000μm) with ultrahigh mass loading without cracking caused by capillary forces[234].

In this study, the DIT method was applied for the first time to fabricate graphite anodes featuring vertically aligned and highly interconnected porous networks, using solely commercially available components without any laboratory modifications. By first establishing the appropriate volume ratio for DIT processing of graphite slurry, we successfully produced thick freestanding electrodes with a thickness of approximately 500 μm. This approach offers several key advantages over conventional SC method: (1) it overcomes the typical thickness limitations associated with SC electrodes[235]; (2) it demonstrates scalability, as the lab-scale mould system used in this study can be readily adapted to larger plate-based formats; and (3) it enables structural tunability, as adjusting the solid-to-water ratio in the slurry allows for control over pore size and porosity. Under a charge rate of 0.1 C, the current densities for the DIT and SC anodes were 1.7 mA cm^{-2} and 0.6 mA cm^{-2}, respectively. At this rate, both electrodes delivered a specific capacity of 372.0 mAh g^{-1}. However, the DIT anode achieved a 2 times higher areal capacity of 11.0 mAh cm^{-2}, compared to 5.0 mAh cm^{-2} for the SC anode. At a higher rate of 0.6 C (approximately 10 mA cm^{-2}), the DIT electrode retained a specific capacity of 259.6 mAh g^{-1} and an areal capacity of 7.5 mAh cm^{-2}, while the SC electrode delivered only 212.9 mAh g^{-1} and 2.8 mAh cm^{-2}. These results highlight the potential of the DIT strategy to enable high-mass-loading graphite anodes with improved rate capability and areal performance. Additionally, the thickness and mass loading achieved through DIT without

structural failures signify a pivotal advancement in battery technology, focusing on not just performance but also scalable manufacturing methods suitable for future energy storage applications[236][237].

5.2 Results and Discussion

5.2.1 Fabrication of Graphite Anode by DIT

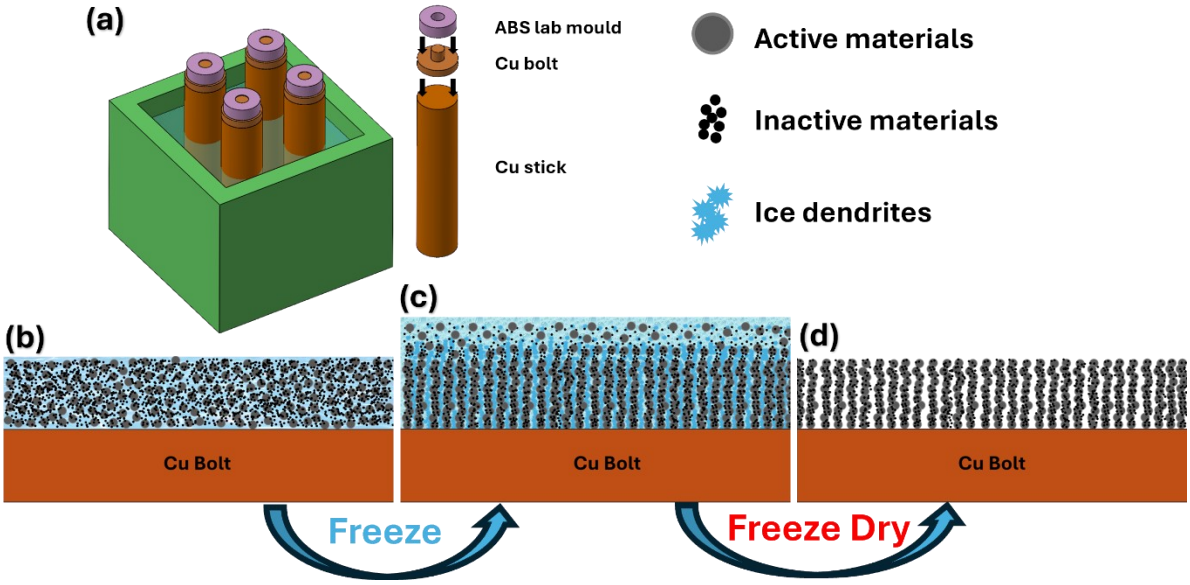


Figure 5.1 (a)Schematics of DIT apparatus for anode, and (b)-(d) cross section of the anode slurry during freezing and freeze-drying procedure.

The slurry was composed of graphite powder (95 wt%) as the active material, and a mixed binder system consisting of SBR (3 wt%) and CMC (2 wt%)[238]. The weight ratio of the solid mixture to deionized water was set at 26:74. This ratio was determined based on results from a previous study on the DIT cathode, where a solid-to-water weight ratio of 40:60 corresponded to a volume ratio of 15.8:84.2. Since the ratio of deionized water affects the porosity and microstructure formation of the electrode, the same volume ratio of 15.8:84.2 between the solid mixture and deionized water was maintained for the anode. Consequently, the weight ratio of the solid mixture to deionized water for the DIT anode was calculated to be 26:74. As shown in Figure 5.1, the schematic illustrates the DIT apparatus designed for anode fabrication, comprising ABS 3D-printed moulds, a copper (Cu) bolt, a Cu rod, and a container for liquid nitrogen. To initiate the freezing of the anode slurry, the ABS mould, Cu bolt, and Cu rod were

assembled from top to bottom. The components were precisely designed to create a 1 mm-thick annular gap at the top of the Cu bolt, with the inner wall of the ABS mould serving as the containment boundary for the slurry. This circular gap had a diameter of 6.5 mm and a thickness of 1 mm, providing the space for the anode slurry. This DIT apparatus allows the electrode thickness to be fabricated up to 1000 μm. The prepared ABS mould, Cu bolt, and Cu rod assembly were then placed into a container filled with liquid nitrogen at approximately -196 °C, which acted as the cold source[239]. Due to the high thermal conductivity of copper, the anode slurry within the gap froze completely within approximately 5 minutes[240]. During the 5-minute freezing process, the DI water contained in the anode slurry froze directionally from the bottom to the top, as the cold source was deliberately positioned beneath the assembly. As freezing progressed shown from Figure 5.1b to Figure 5.1c, ice crystals formed along this vertical direction, with ice dendrites growing upward from the bottom. The advancing ice front pushed suspended particles aside, resulting in the formation of aligned ice columns extending through the slurry[206]. After freezing, the Cu bolt and ABS mould containing the frozen slurry were removed and transferred to a freeze dryer. The freeze-drying procedure shown from Figure 5.1c to Figure 5.1d was conducted at -40 °C and 0.1 mbar. Under these conditions, the solid ice underwent sublimation, transitioning directly from the solid phase to the gas phase[56]. This process left behind vertical channels where the ice columns had formed, creating aligned pores within the electrode shown in Figure 5.1d. This fabrication method avoided the liquid-to-gas phase transition that typically occurs in conventional SC electrodes, which often leads to shrinkage and cracking due to capillary forces[241]. By eliminating these effects, the DIT method enabled the production of thick electrodes with ultrahigh mass loading while preserving the desirable vertically aligned microstructure.

The reference electrode group was prepared using the conventional slurry-coating (SC) method, resulting in an electrode thickness of 200 μm after drying and a mass loading of 16 mg cm^{-2}.

A thickness of 200 µm was selected because SC electrodes exceeding this thickness tend to crack easily during drying due to capillary forces, compromising production stability. The fabrication of thicker SC electrodes, compared to typical commercial SC graphite electrodes, enabled a fair comparison with the ultra-thick DIT graphite electrodes, which exhibited a thickness of 500 µm and a mass loading of 46 mg cm^{-2} with a porosity of 37.5%. This experimental design highlighted the advantages of the DIT fabrication method in producing stable, thick electrodes. Moreover, the thickness of the DIT graphite anode could be adjusted to match the capacity of the corresponding cathode in practical battery applications.

5.2.2 Electrode Structure

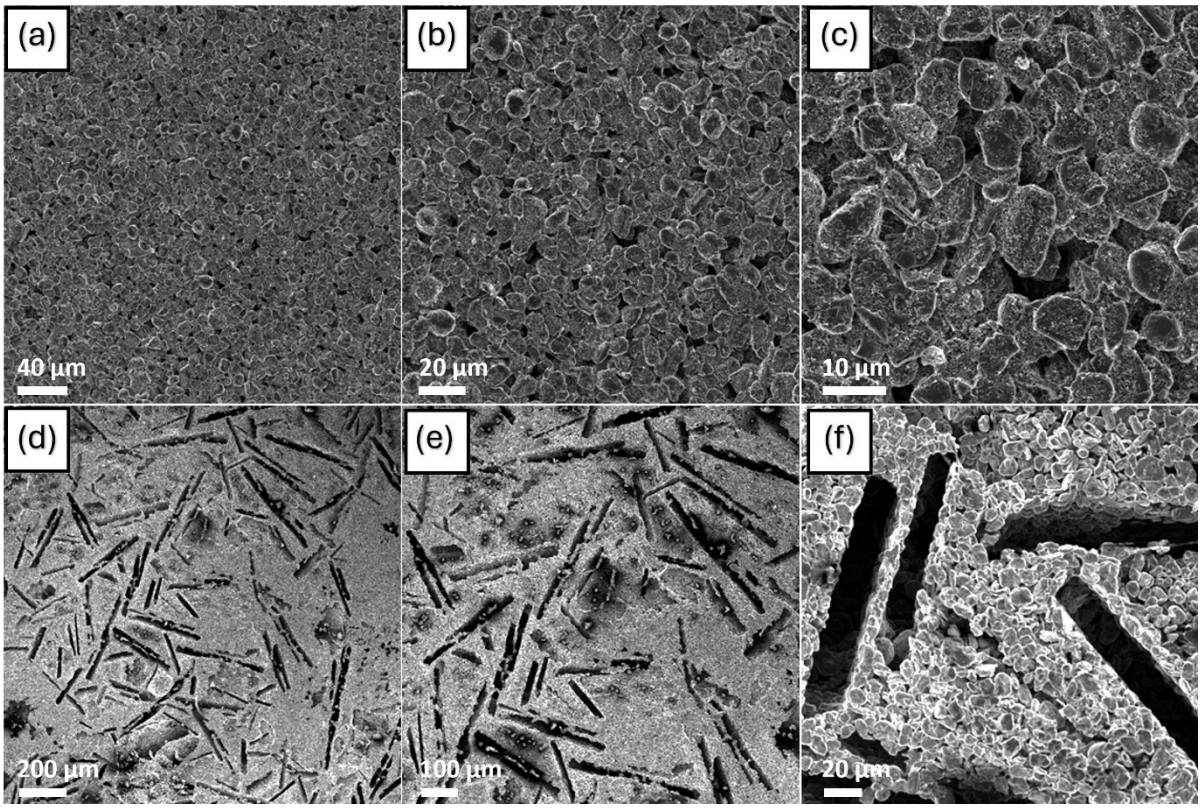


Figure 5.2 SEM images of the top surface and the magnification views of (a)-(c) SC graphite anode and (d)-(f) DIT graphite anode

Figure 5.2 a-c presents SEM images of the top surface of the SC graphite anode. As expected, this microstructure reflects the typical appearance of electrodes fabricated by conventional slurry casting and thermal drying processes. In this method, active and inactive particles are homogenized using a mixer, coated onto copper foil, and subsequently dried in a vacuum oven

to remove residual moisture. This process leads to the formation of a compact, densely packed particle network with randomly distributed, irregularly shaped pores, as shown in Figure 5.2a. Such a congested surface structure significantly restricts the formation of interconnected pathways for electrolyte infiltration. Consequently, electrolyte penetration into the thick SC graphite anode requires approximately 40 minutes. The limited porosity and high tortuosity force ionic transport to rely predominantly on slow solid-state diffusion rather than efficient liquid-phase conduction. This results in poor electrolyte wetting, non-uniform lithiation, and increased polarization during cycling, especially under high-rate conditions, ultimately contributing to accelerated capacity fade and reduced electrochemical stability. In contrast, Figure 5.2d-f shows the top surface morphology of the DIT graphite anode. These images reveal a unique surface structure compared to the SC anode. In Figure 5.2 d,e, well-defined pores can be clearly seen. These pores were created during the DIT process. When the slurry was frozen, ice crystals grew and pushed the solid particles aside. During freeze-drying, the ice sublimated directly from solid to vapor, leaving aligned pores where the ice columns had formed. Figure 5.2f shows that these pores are typically 15 - 20 μm wide and 80 - 100 μm long. This porous network provides connected channels that allow the electrolyte to penetrate quickly and evenly usually in 1 minute, which helps improve ion transport and promotes uniform lithiation across the thick electrode.

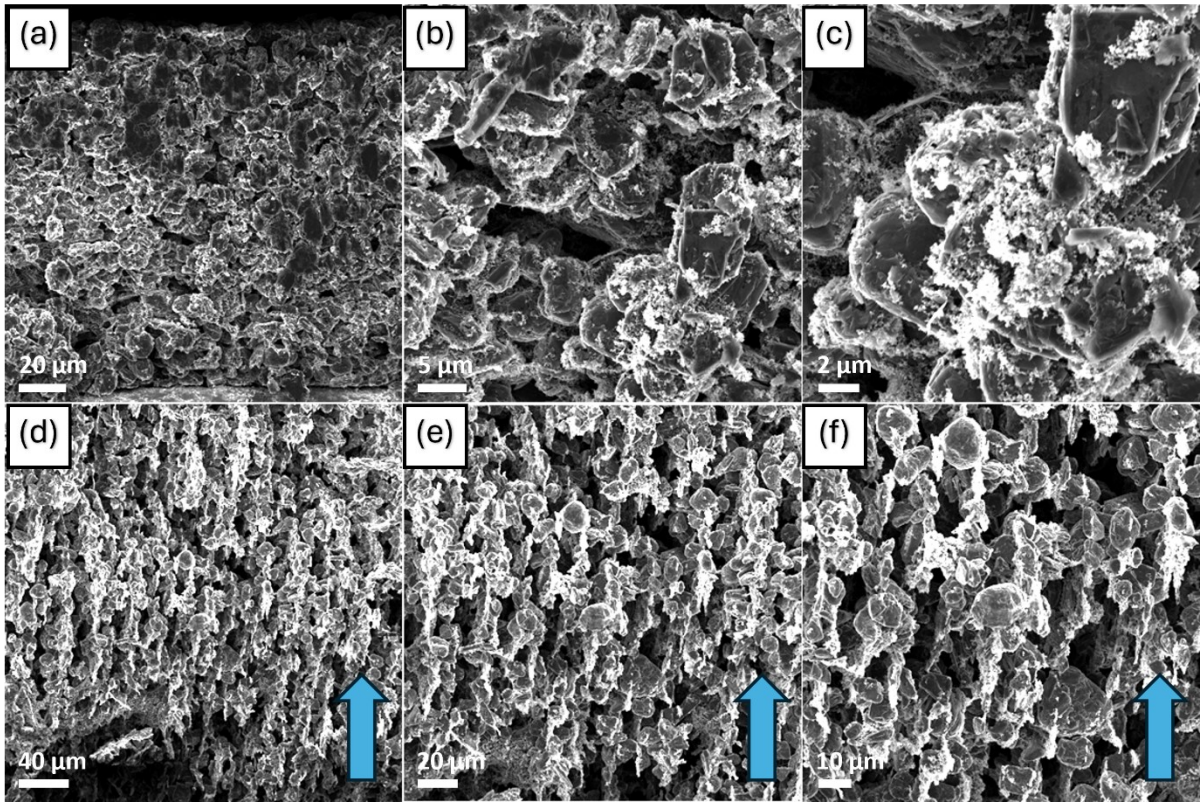


Figure 5.3 SEM images of the cross section and the magnification views of (a)-(c) SC graphite anode and (d)-(f) DIT graphite anode

Figure 5.3 presents SEM images of the cross sections of SC graphite anodes (a) - (c) and directionally ice-templated (DIT) graphite anodes (d) - (f), with blue arrows indicating the freezing direction during DIT fabrication. These cross-sectional views reveal the internal microstructures that directly influence lithium-ion transport during charge and discharge, where ions migrate from the electrode bulk toward the separator. Figure 5.3a-c show the SC anode cross sections at increasing magnifications. The electrode displays a dense, disordered microstructure, with graphite particles averaging ~5 µm in size and irregularly distributed pores ranging from ~2-30 µm. The SC electrode had an overall thickness of ~200 µm with a porosity of approximately 30%. The randomly shaped, isolated pores increase tortuosity and limit the formation of continuous ionic pathways, forcing lithium ions to follow convoluted diffusion paths that can hinder high-rate performance. In contrast, Figure 5.3d-f illustrate the DIT anode cross sections. These images show a vertically aligned porous network formed by directional freezing, as indicated by the blue arrows. The DIT electrodes maintained similar graphite

particle sizes (~5 μm) but exhibited more uniformly distributed pores (~2-10 μm). The DIT anodes had a slightly greater thickness of ~500 μm and a porosity of ~37.5%. The aligned pore channels provide continuous, low-tortuosity pathways for lithium-ion diffusion along the freezing direction, enabling faster and more uniform ionic transport through the thick electrode, which can improve rate capability and cycling stability. Neither electrode showed obvious surface cracking, and both electrodes were fabricated without undergoing any calendaring process to reduce their thickness.

5.2.3 Electrochemical Performance

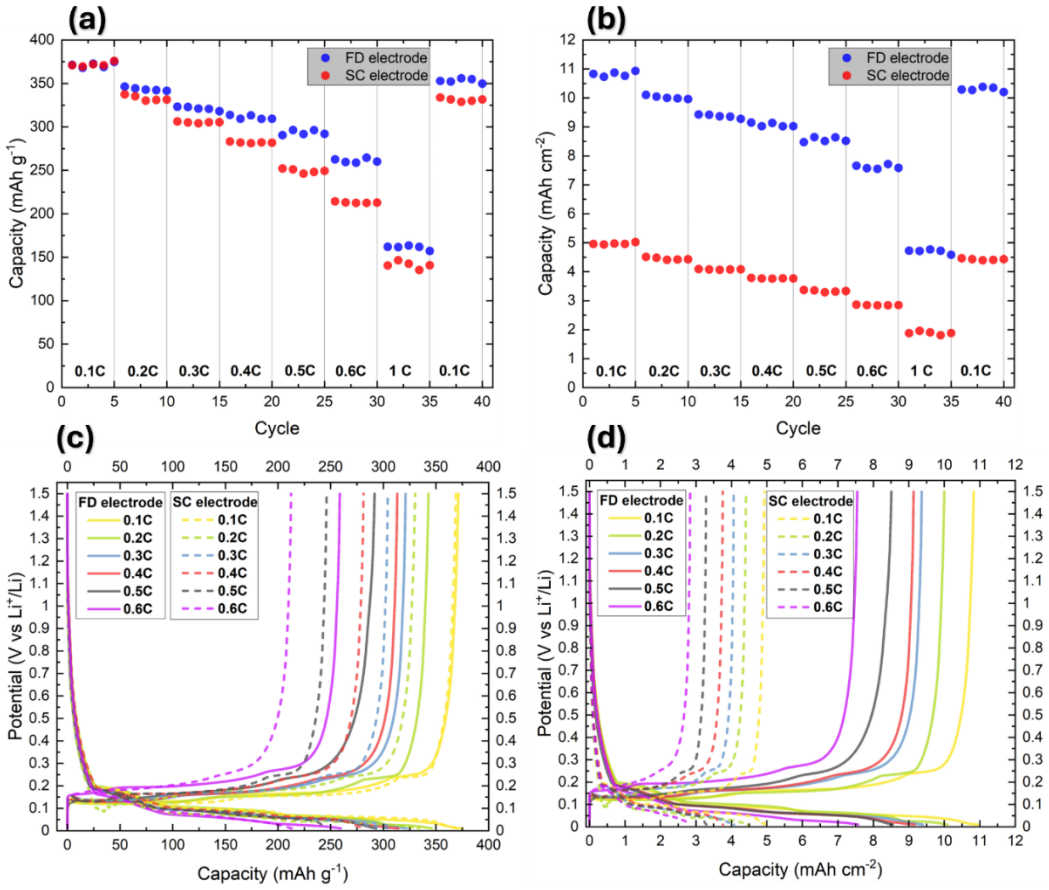


Figure 5.4 Comparative C-rate Performance and Charge–Discharge Profiles of FD(DIT) and SC Graphite Anodes

The mass loading of the DIT electrode was ~46 mg cm^{-2}, while the SC electrode had a mass loading of ~16 mg cm^{-2}. For reference, typical commercial graphite anodes have mass loadings around 8 mg cm^{-2}. Therefore, the tested C-rates for the DIT electrode (0.1C, 0.2C, 0.3C, 0.4C,

0.5C, 0.6C, and 1 C) correspond to approximately 0.6C, 1.2C, 1.8C, 2.4C, 3.0C, 3.6C, and 6 C equivalents when normalized to standard 8 mg cm^{-2} electrodes (calculated as 46/8 ≈ 5.75×), highlighting the high current densities applied in this study[242]. In this electrochemical performance test, the current density of DIT anode and SC anode at 0.1C was 1.7 mA cm^{-2} and 0.6 mA cm^{-2}. Figure 5.4a,b shows the C-rate performance of the DIT and SC graphite anodes in terms of specific capacity (mAh g^{-1}) and areal capacity (mAh cm^{-2}), respectively. Across all tested C-rates, the DIT anode consistently delivers higher capacities than the SC anode even though the DIT anode has almost 3 times mass loading. Specifically, the DIT electrode maintains a specific capacity above 300 mAh g^{-1} at low rates (0.1 - 0.2 C) and retains above 150 mAh g^{-1} at 1 C, while the SC anode shows faster capacity decay, falling below 150 mAh g^{-1} at 1 C. Areal capacities (Figure 5.4b) confirm this trend, with the DIT anode achieving more than 10 mAh cm^{-2} at 0.1 C and maintaining ~5 mAh cm^{-2} at 0.6 C, whereas the SC electrode reaches only ~7 mAh cm^{-2} initially and drops to ~2 mAh cm^{-2} at 0.6 C. Figure 5.4c,d display the charge-discharge voltage profiles of DIT and SC anodes in terms of specific and areal capacity, respectively. In both panels, the DIT electrode demonstrates longer and flatter plateaus across all C-rates, reflecting more stable lithiation/de-lithiation and better kinetic behaviour. The SC electrode shows increased polarization at higher C-rates, evidenced by steeper slopes and earlier voltage cutoffs, indicating limited ionic transport and higher overpotential. The superior performance of the DIT anode is attributed to its vertically aligned porous structure, which facilitates faster and more uniform electrolyte infiltration and lithium-ion diffusion, especially at high mass loading. After cycling at higher C-rates, both electrodes were returned to 0.1 C to assess capacity recovery. The DIT electrode demonstrated excellent reversibility, with its specific capacity recovering to above 350 mAh g^{-1} and areal capacity exceeding 10 mAh cm^{-2} after returning to 0.1 C. In contrast, the SC electrode only recovered to around 330 mAh g^{-1} and ~4.5 mAh cm^{-2}. These results indicate that the DIT electrode

maintains structural integrity and better electrochemical reversibility during high C-rate cycling, whereas the SC electrode exhibits more irreversible capacity loss due to its denser structure and limited ion transport pathways. Overall, the DIT graphite anode outperforms the conventional SC anode in both gravimetric and areal capacities, as well as in voltage stability across various charge–discharge rates. This demonstrates the effectiveness of the DIT approach for producing thick electrodes with high areal capacity and strong rate capability.

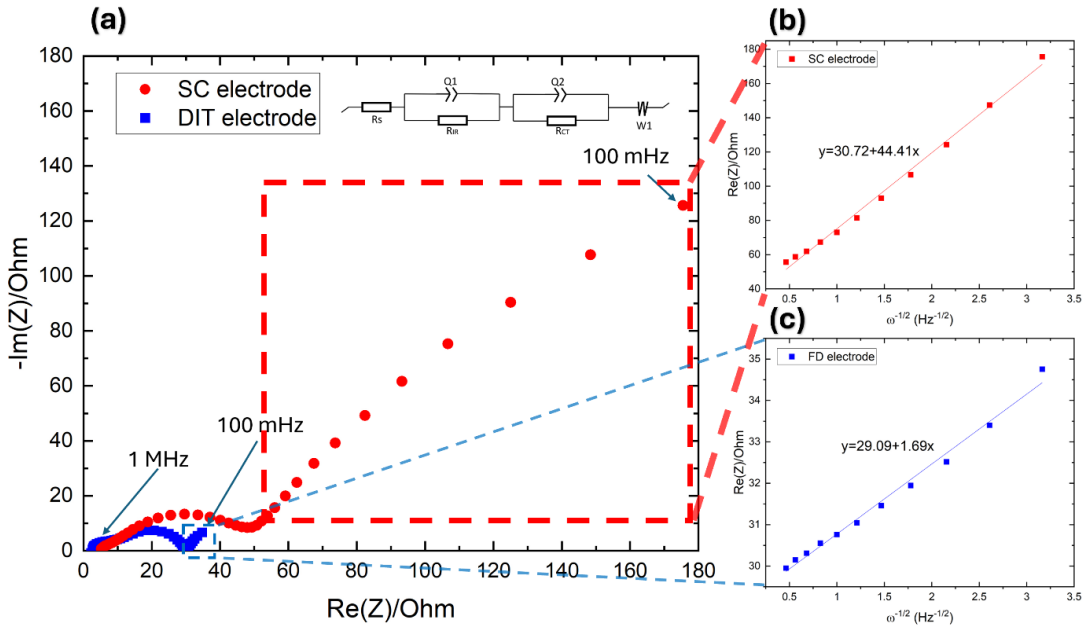


Figure 5.5 (a)Nyquist plots for comparison between DIT graphite anode and SC graphite anode and (b)-(c) linear fitting of real part Re(Z) of the impedance of SC and DIT anode.

Electrochemical impedance spectroscopy (EIS) was performed to evaluate the interfacial and transport properties of both SC and DIT graphite anodes[243]. The Nyquist plots (Figure 5.5a) reveal a significantly smaller semicircle and suppressed Warburg tail for the DIT electrode, indicating reduced charge transfer and diffusion resistances[244]. Fitting the impedance spectra to an equivalent circuit model comprising three resistive elements (shown in Figure 5.5a insert image) provided quantitative insight into the improvements[177]. The DIT electrode exhibited lower values across all resistance components: electrolyte resistance (R_S = 2.57 Ω vs. 4.84 Ω), internal resistance (R_{IR} = 5.19 Ω vs. 9.50 Ω), and charge transfer resistance (R_{ct} = 21.57 Ω vs. 25.11 Ω), compared to the SC electrode. This corresponds to a ~26% reduction in total

resistance, suggesting that the DIT process significantly enhances ionic and electronic pathways through improved electrode architecture[111]. These results demonstrate that the DIT structure not only facilitates better electrolyte accessibility but also promotes faster electrochemical kinetics, contributing to the overall superior performance of the electrode.

To investigate the how DIT fabrication method improves the lithium ion diffusion coefficient in graphite anode. The lithium-ion diffusion coefficient (D_{Li+}) was calculated based on EIS using Warburg impedance analysis[106]. The Warburg coefficient (σ) was obtained by linear fitting of the real part of the impedance (Z′) versus the inverse square root of angular frequency ($\omega^{-1/2}$) in the low-frequency region. The diffusion coefficient was then calculated using the following equation[107]:

$$D_{Li^+} = \frac{R^2T^2}{2A^2n^4F^4C^2\sigma^2}$$

where: D_{li}^+ is the diffusion coefficient of lithium ions ($cm^2\ s^{-1}$), R is the gas constant (8.314 J $mol^{-1}\ K^{-1}$), T is the absolute temperature (K), A is the electrode surface area (cm^2), n is the number of electrons transferred per reaction, F is the Faraday constant (96485 C mol^{-1}), C is the molar concentration of lithium ions in the electrode (mol cm^{-3}), σ is the Warburg coefficient ($\Omega \cdot s^{-1/2}$) obtained from the slope of the Z′ vs. $\omega^{-1/2}$ plot. The lithium ion diffusion of DIT graphite anode was 1.61 x 10^{-10} $cm^2\ s^{-1}$, and the SC graphite anode shows 4.62 x 10^{-15} $cm^2\ s^{-1}$. Although the DIT electrode possessed a significantly greater thickness of 500 µm compared to the 200 µm thickness of the SC electrode, it exhibited a much higher lithium-ion diffusion coefficient. This enhancement is attributed to the aligned porous microstructure formed via DIT, which facilitates more efficient ion transport pathways. In contrast, the SC electrode, despite being thinner than DIT anode, showed a substantially lower diffusion coefficient due to its densely packed structure and congested particle distribution, which hinder

lithium-ion movement. These results highlight the capability of the DIT approach to fabricate ultra-thick electrodes while maintaining efficient lithium-ion transport.

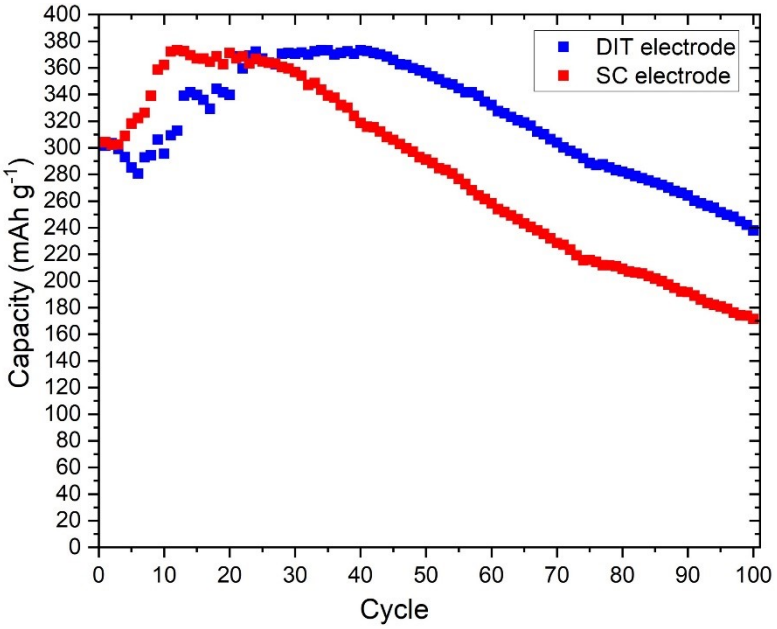


Figure 5.6 Long cycling results of DIT electrode and SC electrode

Under a 0.01 - 1.5 V window at 0.2 C, the DIT anode (3.4 mA cm^{-2}) outperforms the SC anode (1.2 mA cm^{-2}) despite the higher areal current. In the first cycle, the DIT and SC anodes delivered 301 and 304 mAh g^{-1}, respectively. After 100 cycles, the DIT retained 238 mAh g^{-1} (79.1 % of its initial capacity), whereas the SC anode decreased to 171 mAh g^{-1} (56.3 % of its initial capacity). When referenced from the post-formation plateau (~30 cycles), DIT maintained from 370 to 240 mAh g^{-1} (64.9 % retention), while SC fell from from 360 to 170 mAh g^{-1} (47.2 %). The corresponding fade rates are around 1.86 and around 2.71 mAh g^{-1} $cycle^{-1}$, respectively. These results clearly highlight that the vertically aligned, low-tortuosity pore network in DIT electrodes reduces ionic path length and polarization, sustaining higher capacity and suppressing degradation even under harsher current conditions

5.3 Experimental Section

5.3.1 Fabrication of Electrodes

The slurries for DIT and SC graphite anodes were prepared at ambient conditions (15 °C) with different solid-to-solvent weight ratios. For DIT anodes, graphite powder (95 wt%, Spherical, American Elements Ltd.), SBR (3 wt%, Cambridge Energy Solution Ltd.), and CMC (2 wt%) were dispersed in deionized water at a solid-to-solvent ratio of 26:74. All component masses were measured using an analytical balance (Ohaus, Model PR124/E) to ensure precise composition. For SC anodes, the same composition was used but with a solid-to-solvent ratio of 50:50. In both cases, the suspensions were homogenized using a planetary mixer (ARE-250, Thinky) at 2000 rpm for 20 minutes. For SC anodes, the homogeneous slurry was evenly coated onto copper foil (10 μm thickness) at a coating speed of 5 mm s^{-1} using a doctor blade coater (AFA-V, Shanghai Modern Instruments). The coated foils were dried in an oven at 80 °C for 50 minutes, followed by vacuum drying at 110 °C for 120 minutes. Circular electrodes with a diameter of 16 mm were then punched using a disc cutter. For DIT anodes, the homogeneous slurry was poured into 3D-printed moulds with controlled dimensions of 6.5 mm. The moulds containing the slurry were rapidly frozen from 15 °C to - 40 °C by placing them in contact with a cold source cooled by liquid nitrogen, inducing directional ice growth from the bottom upwards. Once fully frozen, the moulds containing the frozen slurry and Cu bolts were immediately transferred to a freeze dryer (Labconco - 50 °C Benchtop Freeze Dryer) operating at - 40 °C and 0.1 mbar for 2 hours to sublimate the ice and preserve the vertically aligned porous structure. After freeze-drying, the DIT electrodes were carefully removed from the moulds, resulting in freestanding electrodes with a final diameter of approximately 6 mm. 30 sets of samples were prepared for both DIT and SC graphite anodes, with mass loading errors maintained within 5%. The entire DIT fabrication process—from powder to cell assembly—takes less than 3 hours, whereas the conventional SC process requires approximately 3.5 hours.

5.3.2 Characterization

All component masses and finished electrode weights were determined using an analytical balance (Ohaus PR124/E, Switzerland) with an accuracy of 0.001 g. Electrode thickness measurements were obtained using a precision micrometre (DML Ltd., United Kingdom) capable of 0.001 mm resolution. The microstructure and surface morphology of the electrodes were characterized by scanning electron microscopy (SEM, Zeiss Sigma300). To achieve high-quality cross-sectional images, the electrodes were prepared using a fully automated argon ion milling system (PECS II, GATAN), operated at 8 keV for 6 hours, producing smooth and flat sections ideal for SEM observation. The porosity of the electrodes was quantified through analysis of SEM cross sections using ImageJ software, employing its segmentation tool to distinguish pore structures from solid phases.

5.3.3 Electrochemical Testing

To evaluate the electrochemical behaviour of the prepared graphite anodes, the thickness and mass of each DIT and SC electrode disc were measured in a cleanroom environment. The discs were then immediately transferred into an argon-filled glovebox (MBRAUN, Germany) maintained with moisture and oxygen levels below 0.1 ppm. Prior to introduction into the glovebox, all electrode discs were placed in the antechamber, where they underwent three cycles of argon purging and vacuum evacuation to ensure minimal exposure to ambient air. The electrodes were assembled into CR2032-type coin cells in a half-cell configuration, employing lithium metal chips as both the counter and reference electrodes. The electrolyte used was a 1.0 M solution of lithium hexafluorophosphate ($LiPF_6$) dissolved in a 1:1 volume ratio of ethylene carbonate (EC) and ethyl methyl carbonate (EMC). A microporous polypropylene separator (Celgard 2500) was placed between the working and counter electrodes. Galvanostatic charge–discharge measurements were carried out at various C-rates within a voltage window of 0.01 V to 1.5 V using a battery testing system (Arbin BT-G-48) to assess cycling performance. The long cycling test was conducted for 100 times by Arbin BT-

G-48 with the voltage window keeping constant between 0.01 V and 1.5 V. EIS was performed with a Biologic SP-240 across a frequency range of 1 MHz to 100 mHz with an amplitude of 10 mV. All electrochemical measurements were conducted at room temperature (approximately 15 °C).

5.4 Conclusion

In this study, a novel DIT method was successfully applied to fabricate thick graphite anodes with an aligned, vertically ordered porous microstructure. This architecture significantly enhances both electronic and ionic transport kinetics. By maintaining the same volumetric ratio used for DIT-fabricated NMC cathodes and optimizing the solid-to-water ratio in the slurry, a freestanding graphite anode with a thickness of ~500 μm and a high active material mass loading of 46 mg cm^{-2} was achieved. Despite its high loading, the DIT anode exhibited a porosity of 37.5%, comparable to the 35% of the SC graphite anode. The DIT electrode demonstrated nearly three times the mass loading of the SC electrode while maintaining excellent electrochemical performance across all charge/discharge rates. It also showed superior capacity retention and reversibility. Notably, the areal capacity of the DIT anode was more than twice that of the SC counterpart. EIS further confirmed the structural and transport advantages of the DIT architecture. The lithium-ion diffusion coefficient for the DIT anode was calculated to be 1.61 x 10^{-10} cm^2 s^{-1} and is significantly higher than that of the SC electrode 4.62 x 10^{-15} cm^2 s^{-1}. Additionally, the DIT electrode exhibited significantly lower internal resistance, reflecting improved ionic mobility and reduced charge-transfer impedance. Importantly, the DIT approach overcomes conventional thickness limitations in graphite anode fabrication. The ability to construct thick, high-performance anodes is critical for next-generation energy storage systems, as it reduces the relative volume of inactive components and improves overall energy density at the cell and pack level.

Chapter 6

6 Conclusion

6.1 Conclusion

This thesis has developed and advanced DIT as a sustainable and scalable electrode fabrication method for lithium-ion batteries, which was effective for both cathodes and anodes. Across the three main results chapters, this work established the feasibility of aqueous DIT processing. It also validated its scalability to industrially relevant dimensions and confirmed its versatility for different electrode chemistries.

In the results presented in Chapter 3, an aqueous DIT process was introduced for NMC811 cathodes. This method enabled the fabrication of vertically aligned microstructures that facilitated faster dual electron and ion transport. By removing the need for toxic NMP solvent, the approach provided a safer and more sustainable alternative to conventional slurry coating. Surface-sensitive characterisation confirmed that NMC811 remained stable during aqueous processing and electrochemical testing demonstrated clear performance advantages. Owing to the nearly doubled mass loading achieved through the DIT architecture, the DIT-C electrode delivered three times higher gravimetric capacity and five times higher areal capacity than the SC electrode at a current density of 5.7 mA cm^{-2}. CV and EIS measurements further revealed an enhanced ion diffusion coefficient and a reduction in impedance for the DIT-C electrode. In pouch cell configuration, these structural and transport benefits translated into significantly improved energy storage metrics, with the DIT-C electrode achieving 496.2 Wh kg^{-1} gravimetric energy density and 1080.9 Wh L^{-1} volumetric energy density, compared with 163.5 Wh kg^{-1} and 344.5 Wh L^{-1} for the SC electrode under the same conditions and similar cell volume. These findings highlight the ability of the aqueous DIT process to realise high-loading, high-performance NMC811 cathodes suitable for practical energy storage applications.

Chapter 4 extended the DIT concept toward manufacturing-scale electrodes. Using directional extreme supercooling, ultra-thick DIT cathodes of approximately 1000 μm and mass loadings up to 70 mg cm^{-2} were fabricated while maintaining a vertically aligned microstructure. A

systematic investigation of the calendaring process identified a critical threshold of 30% thickness reduction that provided the optimal balance between structural integrity and packing density. At this level, the electrodes exhibited low impedance, high volumetric capacity and stable cycling at elevated current densities, whereas excessive calendaring led to degradation of structural alignment and performance. Pouch cell performance estimation further confirmed the advantages of this optimised structure, with the 30% calendered DIT cathode achieving 367 Wh kg^{-1} gravimetric energy density and 779 Wh L^{-1} volumetric energy density at 7 mA cm^{-2}, compared with 102 Wh kg^{-1} and 215 Wh L^{-1} for SC electrodes of similar porosity. Analysis of Li^+ diffusion revealed average D_{Li+} values of 2.88×10^{-9} cm^2 s^{-1} for the 30% calendered electrode and 3.01×10^{-9} cm^2 s^{-1} for the uncalendered electrode, indicating that the calendaring process did not significantly disrupt ion transport pathways. The 30% calendered electrode therefore achieved a favourable balance between fast ion transport kinetics and enhanced volumetric performance. These findings demonstrate that DIT combined with controlled calendaring, provides a viable route toward scalable and high mass loading cathodes suitable for practical high-energy-density lithium-ion batteries.

Chapter 5 demonstrated the versatility of the DIT method by applying it to the fabrication of high mass loading graphite anodes. Freestanding DIT anodes with a thickness of approximately 500 μm and a mass loading of ~46 mg cm^{-2} were successfully produced, which is almost three times that of the SC electrode (~16 mg cm^{-2}) and far above commercial graphite anodes (~8 mg cm^{-2}). Despite this high loading, the DIT anodes maintained moderate porosity and delivered excellent electrochemical performance across a wide range of currents. When benchmarked to standard commercial loadings, the tested C-rates for the DIT electrode corresponded to high-rate equivalents of up to ~6 C, yet the electrode still maintained strong capacity retention. The DIT anode achieved specific capacities above 300 mAh g^{-1} at low C-rates and retained more than 150 mAh g^{-1} at 1 C, while also delivering areal capacities

exceeding 10 mAh cm^{-2} at 0.1 C and approximately 5 mAh cm^{-2} at 0.6 C. In contrast, the SC anode showed faster capacity decay and significantly lower areal capacities. After high C-rate cycling, the DIT electrode also demonstrated excellent recovery, returning to above 350 mAh g^{-1} and 10 mAh cm^{-2} at 0.1 C. The enhanced performance is strongly supported by transport analysis: the DIT anode exhibited a lithium-ion diffusion coefficient of 1.61×10^{-10} cm^2 s^{-1}, several orders of magnitude higher than the SC electrode (4.62×10^{-15} cm^2 s^{-1}), together with a much lower internal resistance. These results highlight the ability of DIT to overcome thickness-related transport limitations in graphite anodes and demonstrate its strong potential for enabling high energy density lithium-ion batteries at the cell and pack levels.

Taken together, the work presented in this thesis establishes DIT as a powerful and versatile microstructural engineering strategy for both cathodes and anodes, enabling electrodes with high mass loading, low tortuosity and enhanced rate performance. By demonstrating aqueous processing, manufacturing-scale feasibility and cross-chemistry compatibility, the thesis shows that DIT is not only a sustainable alternative to slurry coating at small scale but also a scalable approach for producing thick and aligned electrodes. These features reduce the proportion of inactive components and significantly enhance both gravimetric and volumetric energy density. Overall, the findings position DIT as a promising electrode design and manufacturing strategy for next-generation high-energy-density lithium-ion batteries, with meaningful implications for applications ranging from electric vehicles to grid-scale energy storage.

6.2 Future Work

Future work can extend the findings of this thesis in several directions. A key priority is to investigate the three-dimensional microstructure of DIT electrodes using high-resolution techniques such as X-ray nano-tomography or FIB-SEM reconstruction. This will provide a more complete understanding of pore alignment, tortuosity and structural uniformity. Another important direction is to study ion-transport behaviour and structural changes during cycling

through in situ or operando characterisation. Such studies will help clarify how microstructural evolution affects electrochemical performance. Further optimisation of full-cell design is also needed to make full use of DIT electrodes. Adjustments in electrode balancing, electrolyte choice and electrode thickness may further improve energy density and rate performance. Developing a room-temperature DIT process offers another promising path. By changing the solvent system or controlling solidification kinetics, it may be possible to lower energy consumption and simplify scale-up. In the longer term, designing a continuous industrial production line remains a major objective that would enable DIT to progress from laboratory development to factory manufacturing.

Several aspects of the research could be further refined or approached differently. First, a more systematic optimisation of the freezing gradient during DIT would be valuable, as controlling the thermal profile along the freezing front could improve lamella alignment and reduce microstructural variability. A dedicated study on the influence of freezing rate and thermal boundary conditions would help establish processing windows for consistent electrode structures. Second, the interfacial stability of NMC811 under aqueous processing conditions remains an important consideration. Although Chapter 3 confirmed no severe degradation, more detailed chemical analysis would deepen understanding of surface reactions and guide binder or electrolyte selection. Third, while small scale DIT processing was demonstrated, continuous processing introduces challenges in maintaining uniform freezing conditions, solvent removal and mechanical handling.

Finally, if this PhD were repeated, I would integrate the DIT NMC811 cathode and the DIT graphite anode into a full-cell configuration to evaluate their combined performance under practical operating conditions. I would also investigate the upper limits of electrode thickness achievable by DIT to determine the optimal balance between structural integrity, transport kinetics and overall pack-level energy density.

Reference

1. Energy sources through time – timeline — Science Learning Hub, https://www.sciencelearn.org.nz/resources/1636-energy-sources-through-time-timeline

2. MacDowell, N., Florin, N., Buchard, A., Hallett, J., Galindo, A., Jackson, G., Adjiman, C.S., Williams, C.K., Shah, N., Fennell, P.: An overview of CO2 capture technologies. Energy Environ Sci. 3, 1645 (2010). https://doi.org/10.1039/c004106h

3. U.S. Global Change Research Program: Climate science special report: Fourth national climate assessment, volume I. U.S. Global Change Research Program. 1, 470 (2018). https://doi.org/10.7930/J0J964J6

4. Battery Comparison of Energy Density - Cylindrical and Prismatic Cells, https://www.epectec.com/batteries/cell-comparison.html

5. Muralidharan, N., Self, E.C., Dixit, M., Du, Z., Essehli, R., Amin, R., Nanda, J., Belharouak, I.: Next-Generation Cobalt-Free Cathodes – A Prospective Solution to the Battery Industry's Cobalt Problem. Adv Energy Mater. 12, (2022). https://doi.org/10.1002/aenm.202103050

6. Allamehzadeh, H., Adams, D.: Renewable Energy Source Storage Cross Platform. In: 2024 IEEE 52nd Photovoltaic Specialist Conference (PVSC). pp. 1398–1401. IEEE (2024)

7. Bai, Y., Wang, J., He, W.: Energy arbitrage optimization of lithium-ion battery considering short-term revenue and long-term battery life loss. Energy Reports. 8, 364–371 (2022). https://doi.org/10.1016/j.egyr.2022.10.209

8. Ogle, J.P., Melton, R.B., Schneider, K.P., Jinsiwale, R.: Enhancing Responsiveness and Resilience with Distributed Applications in the Grid. In: 2021 IEEE Rural Electric Power Conference (REPC). pp. 15–20. IEEE (2021)

9. Lin, J., Li, W., Chen, Z.: Scaling Direct Recycling of Lithium-Ion Batteries toward Industrialization: Challenges and Opportunities. ACS Energy Lett. 10, 947–957 (2025). https://doi.org/10.1021/acsenergylett.4c03176

10. Villa-Ávila, E., Ochoa-Correa, D., Arévalo, P.: Advancements in Power Converter Technologies for Integrated Energy Storage Systems: Optimizing Renewable Energy Storage and Grid Integration. Processes. 13, 1819 (2025). https://doi.org/10.3390/pr13061819

11. Tian, J., Fan, Y., Pan, T., Zhang, X., Yin, J., Zhang, Q.: A critical review on inconsistency mechanism, evaluation methods and improvement measures for

lithium-ion battery energy storage systems. Renewable and Sustainable Energy Reviews. 189, 113978 (2024). https://doi.org/10.1016/j.rser.2023.113978

12. Ge, Y., Chen, J., Ma, G., Huang, R., Meng, F., Hu, R.: Low-Temperature-Sensitivity Materials for Low-Temperature Lithium-Ion Batteries. ACS Appl Mater Interfaces. 17, 13232–13245 (2025). https://doi.org/10.1021/acsami.4c21441

13. Ortiz, Y., Arévalo, P., Peña, D., Jurado, F.: Recent Advances in Thermal Management Strategies for Lithium-Ion Batteries: A Comprehensive Review. Batteries. 10, 83 (2024). https://doi.org/10.3390/batteries10030083

14. Sarakonsri, T., Kumar, R.V.: Primary Batteries. Rechargeable Ion Batteries: Materials, Design, and Applications of Li-Ion Cells and Beyond. 21–47 (2022). https://doi.org/10.1002/9783527836703.CH2;JOURNAL:JOURNAL:BOOKS;WGROUP:STRING:PUBLICATION

15. Li, J., Cai, Y., Wu, H., Yu, Z., Yan, X., Zhang, Q., Gao, T.Z., Liu, K., Jia, X., Bao, Z.: Polymers in Lithium-Ion and Lithium Metal Batteries. Adv Energy Mater. 11, 2003239 (2021). https://doi.org/10.1002/aenm.202003239

16. Huang, Y.: The discovery of cathode materials for lithium-ion batteries from the view of interdisciplinarity. Interdisciplinary Materials. 1, 323–329 (2022). https://doi.org/10.1002/idm2.12048

17. Scrosati, B.: History of lithium batteries. Journal of Solid State Electrochemistry. 15, 1623–1630 (2011). https://doi.org/10.1007/s10008-011-1386-8

18. Lithium-ion Battery Market to Rise at CAGR of 10.8% during, https://www.globenewswire.com/news-release/2022/08/16/2499338/0/en/Lithium-ion-Battery-Market-to-Rise-at-CAGR-of-10-8-during-Forecast-Period-2022-2031-notes-TMR-Study.html

19. Global Lithium-Ion Battery Market to Reach $113.89 Billion, https://www.globenewswire.com/en/news-release/2022/08/11/2496429/28124/en/Global-Lithium-Ion-Battery-Market-to-Reach-113-89-Billion-by-2030.html

20. Jena, K.K., AlFantazi, A., Mayyas, A.T.: Comprehensive Review on Concept and Recycling Evolution of Lithium-Ion Batteries (LIBs). Energy & Fuels. 35, 18257–18284 (2021). https://doi.org/10.1021/acs.energyfuels.1c02489

21. Li, R., Eesbatteries, /, Yao, Y.-X., Xu, L., Yan, C., Zhang, Q.: Principles and trends in extreme fast charging lithium-ion batteries. EES Batteries. 1, 9–22 (2025). https://doi.org/10.1039/D4EB00011K

22. Li, Q., Zhou, D., Chu, M., Liu, Z., Yang, L., Wu, W., Ning, D., Li, W., Liu, X., Li, J., Passerini, S., Wang, J.: A comprehensive understanding on the anionic redox

chemistry of high-voltage cathode materials for high-energy-density lithium-ion batteries. Chem Soc Rev. 54, 3441–3474 (2025). https://doi.org/10.1039/D4CS00797B

23. Ramyashri, S., Amiruddin, R., Emelyanov, A. V., Santhosh Kumar, M.C.: Development of Al foil-based flexible ZnO nanowires/PTAA hybrid piezoelectric nanogenerators. Appl Surf Sci. 709, 163818 (2025). https://doi.org/10.1016/j.apsusc.2025.163818

24. Ahmed, I., Majid, A.: First principles study of titanium oxychloride as an anode material in monovalent and multivalent ion batteries. Mater Sci Semicond Process. 200, 109889 (2025). https://doi.org/10.1016/j.mssp.2025.109889

25. Chen, S., Liu, C., Feng, R., Chen, Z., Lu, Y., Chen, L., Huang, Q., Guan, Y., Yan, W., Su, Y., Li, N., Wu, F.: Natural graphite anode for advanced lithium-ion Batteries: Challenges, Progress, and Perspectives. Chemical Engineering Journal. 503, 158116 (2025). https://doi.org/10.1016/j.cej.2024.158116

26. Liu, C., Sheng, L., Jiang, L.: Research on performance constraints and electrolyte optimization strategies for lithium-ion batteries at low temperatures. RSC Adv. 15, 7995–8018 (2025). https://doi.org/10.1039/D4RA08490J

27. Alzamer, H., Jaafreh, R., Kim, J.G., Hamad, K.: Artificial Intelligence and Li Ion Batteries: Basics and Breakthroughs in Electrolyte Materials Discovery. Crystals 2025, Vol. 15, Page 114. 15, 114 (2025). https://doi.org/10.3390/CRYST15020114

28. Sangsanit, T., Tejangkura, W., Joraleechanchai, N., Sawangphruk, M.: LiF-rich interphase engineering via high-FEC electrolytes in scalable NMC90//graphite 18650 cells for safe and durable electric two-wheelers. Chemical Engineering Journal. 521, 166432 (2025). https://doi.org/10.1016/j.cej.2025.166432

29. Yu, T., Liu, Y., Li, H., Sun, Y., Guo, S., Zhou, H.: Ductile Inorganic Solid Electrolytes for All-Solid-State Lithium Batteries. Chem Rev. 125, 3595–3662 (2025). https://doi.org/10.1021/acs.chemrev.4c00894

30. Yang, J., Weng, C., Sun, P., Yin, Y., Xu, M., Pan, L., Li, J.: Comprehensive regulation strategies for gel electrolytes in aqueous zinc-ion batteries. Coord Chem Rev. 530, 216475 (2025). https://doi.org/10.1016/J.CCR.2025.216475

31. Hao, Z., Lu, Y., Yang, G., Zhao, Q., Yan, Z., Chen, J.: Designing Current Collectors to Stabilize Li Metal Anodes. Advanced Materials. 37, 2415258 (2025). https://doi.org/10.1002/adma.202415258

32. Fujimoto, H., Takagi, S., Shimoda, K., Kiuchi, H., Okazaki, K., Murata, T., Ogumi, Z., Abe, T.: Analysis of Intercalation/De-Intercalation of Li Ions Into/From Graphite at

0 °C via Operando Synchrotron X-ray Diffraction. J Electrochem Soc. 168, 090515 (2021). https://doi.org/10.1149/1945-7111/AC2280

33. Huang, C., Wilson, M.D., Cline, B., Sivarajah, A., Stolp, W., Boone, M.N., Connolley, T., Leung, C.L.A.: Li+ concentration and morphological changes at the anode and cathode interphases inside solid-state lithium metal batteries. Journal of Physics: Energy. 7, 025009 (2025). https://doi.org/10.1088/2515-7655/ADAFDA

34. Sun, K., Peng, Z.: Intermetallic interphases in lithium metal and lithium ion batteries. InfoMat. 3, 1083–1109 (2021). https://doi.org/10.1002/inf2.12216

35. Zhan, R., Wang, X., Chen, Z., Seh, Z.W., Wang, L., Sun, Y.: Promises and Challenges of the Practical Implementation of Prelithiation in Lithium-Ion Batteries. Adv Energy Mater. 11, 2101565 (2021). https://doi.org/10.1002/AENM.202101565

36. Odetallah, M., Kuss, C.: A Review of Chemically Induced Intercalation and Deintercalation in Battery Materials. Energy Technology. 11, 2201060 (2023). https://doi.org/10.1002/ENTE.202201060

37. Wang, R., Wang, L., Liu, R., Li, X., Wu, Y., Ran, F.: “Fast-Charging” Anode Materials for Lithium-Ion Batteries from Perspective of Ion Diffusion in Crystal Structure. ACS Nano. 18, 2611–2648 (2024). https://doi.org/10.1021/acsnano.3c08712

38. Wang, M., Feng, Z.: Interfacial processes in electrochemical energy systems. Chemical Communications. 57, 10453–10468 (2021). https://doi.org/10.1039/D1CC01703A

39. Zhan, H., Qian, Z., Qiao, Y., Lv, B., Liu, R., Chen, H., Liu, Z.: Triggering Ion Diffusion and Electron Transport Dual Pathways for High Efficiency Electrochemical Li + Extraction. ACS Nano. 18, 31204–31214 (2024). https://doi.org/10.1021/acsnano.4c09379

40. Zhang, X., Ju, Z., Zhu, Y., Takeuchi, K.J., Takeuchi, E.S., Marschilok, A.C., Yu, G.: Multiscale Understanding and Architecture Design of High Energy/Power Lithium-Ion Battery Electrodes. Adv Energy Mater. 11, 2000808 (2021). https://doi.org/10.1002/AENM.202000808

41. Trevisanello, E., Ruess, R., Conforto, G., Richter, F.H., Janek, J.: Polycrystalline and Single Crystalline NCM Cathode Materials—Quantifying Particle Cracking, Active Surface Area, and Lithium Diffusion. Adv Energy Mater. 11, 2003400 (2021). https://doi.org/10.1002/AENM.202003400

42. Roy, T., Salazar de Troya, M.A., Worsley, M.A., Beck, V.A.: Topology optimization for the design of porous electrodes. Structural and Multidisciplinary Optimization. 65, 1–21 (2022). https://doi.org/10.1007/S00158-022-03249-2/METRICS

43. Zheng, J., Xing, G., Jin, L., Lu, Y., Qin, N., Gao, S., Zheng, J.P.: Strategies and Challenge of Thick Electrodes for Energy Storage: A Review. Batteries. 9, 151 (2023). https://doi.org/10.3390/batteries9030151

44. Reynolds, C.D., Slater, P.R., Hare, S.D., Simmons, M.J.H., Kendrick, E.: A review of metrology in lithium-ion electrode coating processes. Mater Des. 209, 109971 (2021). https://doi.org/10.1016/J.MATDES.2021.109971

45. Zhang, N., Li, A., Zhang, W., Wang, Z., Liu, Y., Zhang, X., Cai, G., Wan, H., Xu, J., Wang, C.: 4.6 V Moisture-Tolerant Electrolytes for Lithium-Ion Batteries. Advanced Materials. 36, 2408039 (2024). https://doi.org/10.1002/adma.202408039

46. Huttner, F., Marth, A., Eser, J.C., Heckmann, T., Mohacsi, J., Mayer, J.K., Scharfer, P., Schabel, W., Kwade, A.: Design of Vacuum Post-Drying Procedures for Electrodes of Lithium-Ion Batteries. Batter Supercaps. 4, 1499–1515 (2021). https://doi.org/10.1002/BATT.202100088

47. Reynolds, C., Faraji Niri, M., Hidalgo, M.F., Heymer, R., Román, L., Alsofi, G., Khanom, H., Pye, B., Marco, J., Kendrick, E.: Impact of Formulation and Slurry Properties on Lithium-ion Electrode Manufacturing. Batter Supercaps. 7, e202300396 (2024). https://doi.org/10.1002/batt.202300396

48. Yan, Z., Wang, L., Zhang, H., He, X.: Determination and Engineering of Li-Ion Tortuosity in Electrode Toward High Performance of Li-Ion Batteries. Adv Energy Mater. 14, 2303206 (2024). https://doi.org/10.1002/aenm.202303206

49. Schmied-Tobies, M.I.H., Murawski, A., Rucic, E., Schwedler, G., Bury, D., Kasper-Sonnenberg, M., Koslitz, S., Koch, H.M., Brüning, T., Kolossa-Gehring, M.: Alkyl pyrrolidone solvents N–methyl–2–pyrrolidone (NMP) and N–ethyl–2–pyrrolidone (NEP) in urine of children and adolescents in Germany – human biomonitoring results of the German Environmental Survey 2014–2017 (GerES V). Environ Int. 146, 106221 (2021). https://doi.org/10.1016/J.ENVINT.2020.106221

50. Hu, Z., Xu, L., Huang, Y., Li, J., Ouyang, M., Du, X., Jiang, H.: Comprehensive analysis of galvanostatic charge method for fuel cell degradation diagnosis. Appl Energy. 212, 1321–1332 (2018). https://doi.org/10.1016/j.apenergy.2018.01.005

51. Zhou, L., Zhou, Y., Sun, Y.: Enhanced storage of hydrogen at the temperature of liquid nitrogen. Int J Hydrogen Energy. 29, 319–322 (2004). https://doi.org/10.1016/S0360-3199(03)00155-1

52. Originlab GraphGallery, https://www.originlab.com/www/products/GraphGallery.aspx?GID=621

53. Du, Z., Rollag, K.M., Li, J., An, S.J., Wood, M., Sheng, Y., Mukherjee, P.P., Daniel, C., Wood, D.L.: Enabling aqueous processing for crack-free thick electrodes. J Power Sources. 354, 200–206 (2017). https://doi.org/10.1016/j.jpowsour.2017.04.030

54. Huang, C., Grant, P.S.: Coral-like directional porosity lithium ion battery cathodes by ice templating. J Mater Chem A Mater. 6, 14689–14699 (2018). https://doi.org/10.1039/c8ta05049j

55. Huang, C., Dontigny, M., Zaghib, K., Grant, P.S.: Low-tortuosity and graded lithium ion battery cathodes by ice templating. J Mater Chem A Mater. 7, 21421–21431 (2019). https://doi.org/10.1039/c9ta07269a

56. Huang, C., Leung, C.L.A., Leung, P., Grant, P.S.: A Solid-State Battery Cathode with a Polymer Composite Electrolyte and Low Tortuosity Microstructure by Directional Freezing and Polymerization. Adv Energy Mater. 11, (2021). https://doi.org/10.1002/aenm.202002387

57. Amin, R., Delattre, B., Tomsia, A.P., Chiang, Y.-M.: Electrochemical Characterization of High Energy Density Graphite Electrodes Made by Freeze-Casting. ACS Appl Energy Mater. 1, 4976–4981 (2018). https://doi.org/10.1021/acsaem.8b00962

58. Busà, C., Belekoukia, M., Loveridge, M.J.: The effects of ambient storage conditions on the structural and electrochemical properties of NMC-811 cathodes for Li-ion batteries. Electrochim Acta. 366, 137358 (2021). https://doi.org/10.1016/J.ELECTACTA.2020.137358

59. Sander, J.S., Erb, R.M., Li, L., Gurijala, A., Chiang, Y.-M.: High-performance battery electrodes via magnetic templating. Nat Energy. 1, 16099 (2016). https://doi.org/10.1038/nenergy.2016.99

60. Yang, K., Jiang, Y., Huang, C.: Aligned NMC811 electrodes by functionalized conductive graphite flakes for fast-charging Li-ion battery. Next Energy. 2, 100087 (2024). https://doi.org/10.1016/j.nxener.2023.100087

61. Kim, C., Jang, I.: TOPICAL REVIEW • OPEN ACCESS You may also like Electrospun Nanofiber Electrodes with in situ Exsolved Nanocatalysts for Symmetrical SOCs Self-Discharge and Calendar Aging Behavior of Li-Ion and Na-Ion Cells Comprehensive review and future perspectives: 3D printing technology for all types of solid oxide cells. J. Phys. Energy. 6, 32003 (2024). https://doi.org/10.1088/2515-7655/ad5fbb

62. Goel, V., Chen, K.H., Dasgupta, N.P., Thornton, K.: Optimization of laser-patterned electrode architectures for fast charging of Li-ion batteries using simulations parameterized by machine learning. Energy Storage Mater. 57, 44–58 (2023). https://doi.org/10.1016/J.ENSM.2023.01.050

63. von Wald Cresce, A., Xu, K.: Aqueous lithium-ion batteries. Carbon Energy. 3, 721–751 (2021). https://doi.org/10.1002/CEY2.106;WGROUP:STRING:PUBLICATION

64. Rahman, M.M., Imani, S., Anjum, N., Sijuade, A.A., Okoli, O.: Materials and design strategies for next-generation energy storage: A review. Renewable and Sustainable Energy Reviews. 212, 115368 (2025). https://doi.org/10.1016/J.RSER.2025.115368

65. Bitsch, B., Dittmann, J., Schmitt, M., Scharfer, P., Schabel, W., Willenbacher, N.: A novel slurry concept for the fabrication of lithium-ion battery electrodes with beneficial properties. J Power Sources. 265, 81–90 (2014). https://doi.org/10.1016/J.JPOWSOUR.2014.04.115

66. Keppeler, M., Roessler, S., Braunwarth, W.: Production Research as Key Factor for Successful Establishment of Battery Production on the Example of Large-Scale Automotive Cells Containing Nickel-Rich LiNi0.8Mn0.1Co0.1O2 Electrodes. Energy Technology. 8, (2020). https://doi.org/10.1002/ENTE.202000183

67. Märker, K., Reeves, P.J., Xu, C., Griffith, K.J., Grey, C.P.: Evolution of Structure and Lithium Dynamics in LiNi 0.8 Mn 0.1 Co 0.1 O 2 (NMC811) Cathodes during Electrochemical Cycling. Chemistry of Materials. 31, 2545–2554 (2019). https://doi.org/10.1021/acs.chemmater.9b00140

68. R.N., R., Bosubabu, D., M.G., K.B., Ramesha, K.: Tuning of Ni, Mn, and Co (NMC) Content in 0.4(LiNi *x* Mn *y* Co *z* O 2)·0.4(Li 2 MnO 3) toward Stable High-Capacity Lithium-Rich Cathode Materials. ACS Appl Energy Mater. 3, 10872–10881 (2020). https://doi.org/10.1021/acsaem.0c01897

69. Saaid, F.I., Kasim, M.F., Winie, T., Elong, K.A., Azahidi, A., Basri, N.D., Yaakob, M.K., Mastuli, M.S., Amira Shaffee, S.N., Zolkiffly, M.Z., Mahmood, M.R.: Ni-rich lithium nickel manganese cobalt oxide cathode materials: A review on the synthesis methods and their electrochemical performances. Heliyon. 10, (2024). https://doi.org/10.1016/J.HELIYON.2023.E23968

70. Yu, Y., Karayaylali, P., Giordano, L., Corchado-García, J., Hwang, J., Sokaras, D., Maglia, F., Jung, R., Gittleson, F.S., Shao-Horn, Y.: Probing Depth-Dependent Transition-Metal Redox of Lithium Nickel, Manganese, and Cobalt Oxides in Li-Ion Batteries. ACS Appl Mater Interfaces. 12, 55865–55875 (2020). https://doi.org/10.1021/acsami.0c16285

71. Tang, L., Cheng, X., Wu, R., Cao, T., Lu, J., Zhang, Y., Zhang, Z.: Monitoring the morphology evolution of LiNi0.8Mn0.1Co0.1O2 during high-temperature solid state synthesis via in situ SEM. Journal of Energy Chemistry. 66, 9–15 (2022). https://doi.org/10.1016/J.JECHEM.2021.07.021

72. Park, D., Sherrell, P.C., Xie, F., Ellis, A. V.: Improved lithium-ion battery cathode rate performance via carbon black functionalization. J Mater Chem A Mater. 12, 4884–4892 (2024). https://doi.org/10.1039/D3TA05093A

73. He, Y., Jing, L., Ji, Y., Zhu, Z., Feng, L., Fu, X., Wang, Y.: Revisiting the electrode manufacturing: A look into electrode rheology and active material microenvironment. Journal of Energy Chemistry. 72, 41–55 (2022). https://doi.org/10.1016/J.JECHEM.2022.04.038

74. Dallaev, R., Pisarenko, T., Sobola, D., Orudzhev, F., Ramazanov, S., Trčka, T.: Brief Review of PVDF Properties and Applications Potential. Polymers 2022, Vol. 14, Page 4793. 14, 4793 (2022). https://doi.org/10.3390/POLYM14224793

75. Bauer, W., Nötzel, D.: Rheological properties and stability of NMP based cathode slurries for lithium ion batteries. Ceram Int. 40, 4591–4598 (2014). https://doi.org/10.1016/J.CERAMINT.2013.08.137

76. Lee, K.P., Chromey, N.C., Culik, R., Barnes, J.R., Schneider, P.W.: Toxicity of N-methyl-2-pyrrolidone (NMP): Teratogenic, subchronic, and two-year inhalation studies. Fundamental and Applied Toxicology. 9, 222–235 (1987). https://doi.org/10.1016/0272-0590(87)90045-5

77. Gao, H., Ma, T., Duong, T., Wang, L., He, X., Lyubinetsky, I., Feng, Z., Maglia, F., Lamp, P., Amine, K., Chen, Z.: Protecting Al foils for high-voltage lithium-ion chemistries. Mater Today Energy. 7, 18–26 (2018). https://doi.org/10.1016/J.MTENER.2017.12.001

78. Faegh, E., Ng, B., Hayman, D., Mustain, W.E.: Author Correction: Practical assessment of the performance of aluminium battery technologies. Nat Energy. 6, 450–450 (2021). https://doi.org/10.1038/s41560-021-00791-z

79. Buqa, H., Holzapfel, M., Krumeich, F., Veit, C., Novák, P.: Study of styrene butadiene rubber and sodium methyl cellulose as binder for negative electrodes in lithium-ion batteries. J Power Sources. 161, 617–622 (2006). https://doi.org/10.1016/J.JPOWSOUR.2006.03.073

80. Moradi, B., Botte, G.G.: Recycling of graphite anodes for the next generation of lithium ion batteries. Journal of Applied Electrochemistry 2015 46:2. 46, 123–148 (2015). https://doi.org/10.1007/S10800-015-0914-0

81. Shi, M., Song, C., Tai, Z., Zou, K., Duan, Y., Dai, X., Sun, J., Chen, Y., Liu, Y.: Coal-derived synthetic graphite with high specific capacity and excellent cyclic stability as anode material for lithium-ion batteries. Fuel. 292, 120250 (2021). https://doi.org/10.1016/j.fuel.2021.120250

82. Schmidt-Wellenburg, P., Geltenbort, P., Nesvizhevsky, V. V., Plonka, C., Soldner, T., Vezzu, F., Zimmer, O.: A source of ultra-cold neutrons for the gravitational spectrometer GRANIT. (2007). https://doi.org/https://doi.org/10.48550/arXiv.0708.1373

83. Zhang, Q., Wang, H., Ling, Z., Fang, X., Zhang, Z.: RT100/expand graphite composite phase change material with excellent structure stability, photo-thermal performance and good thermal reliability. Solar Energy Materials and Solar Cells. 140, 158–166 (2015). https://doi.org/10.1016/J.SOLMAT.2015.04.008

84. Sun, L., Liu, Y., Shao, R., Wu, J., Jiang, R., Jin, Z.: Recent progress and future perspective on practical silicon anode-based lithium ion batteries. Energy Storage Mater. 46, 482–502 (2022). https://doi.org/10.1016/J.ENSM.2022.01.042

85. Fang, C., Wang, X., Meng, Y.S.: Key Issues Hindering a Practical Lithium-Metal Anode. Trends Chem. 1, 152–158 (2019). https://doi.org/10.1016/j.trechm.2019.02.015

86. McDowell, M.T., Woo Lee, S., Wang, C., Cui, Y.: The effect of metallic coatings and crystallinity on the volume expansion of silicon during electrochemical lithiation/delithiation. Nano Energy. 1, 401–410 (2012). https://doi.org/10.1016/J.NANOEN.2012.03.004

87. Dai, S., Li, J., Lu, N.: Research progress of diamond/copper composites with high thermal conductivity. Diam Relat Mater. 108, 107993 (2020). https://doi.org/10.1016/J.DIAMOND.2020.107993

88. Tang, C.Y., Yang, Z.: Transmission Electron Microscopy (TEM). In: Membrane Characterization. pp. 145–159. Elsevier (2017)

89. Zaefferer, S.: A critical review of orientation microscopy in SEM and TEM. Crystal Research and Technology. 46, 607–628 (2011). https://doi.org/10.1002/CRAT.201100125;CTYPE:STRING:JOURNAL

90. Busà, C., Belekoukia, M., Loveridge, M.J.: The effects of ambient storage conditions on the structural and electrochemical properties of NMC-811 cathodes for Li-ion batteries. Electrochim Acta. 366, 137358 (2021). https://doi.org/10.1016/J.ELECTACTA.2020.137358

91. Vickerman, J.C.: ToF-SIMS-An Overview. , Manchester (2001)

92. Eldosoky, D.S., Kerherve, G., Cobb, J., Hansen, U., Abel, R.: Chemical Bonding between Organic Matrix and Mineral in Human Bone Evidenced by X-Ray Photoelectron Spectroscopy. (2025). https://doi.org/10.2139/SSRN.5332552

93. Yu, H., Gao, Y., Kirtley, J., Borgmeyer, G., He, X., Liang, X.: Recovery of Degraded Ni-Rich NMC811 Particles for Lithium-Ion Batteries. J Electrochem Soc. 169, 050520 (2022). https://doi.org/10.1149/1945-7111/AC6C56

94. Zhu, F.Y., Wang, Q.Q., Zhang, X.S., Hu, W., Zhao, X., Zhang, H.X.: 3D nanostructure reconstruction based on the SEM imaging principle, and applications. Nanotechnology. 25, 185705 (2014). https://doi.org/10.1088/0957-4484/25/18/185705

95. Du, H., Wang, Y., Kang, Y., Zhao, Y., Tian, Y., Wang, X., Tan, Y., Liang, Z., Wozny, J., Li, T., Ren, D., Wang, L., He, X., Xiao, P., Mao, E., Tavajohi, N., Kang, F., Li, B.: Side Reactions/Changes in Lithium-Ion Batteries: Mechanisms and Strategies for Creating Safer and Better Batteries. Advanced Materials. 36, 2401482 (2024). https://doi.org/10.1002/ADMA.202401482

96. Bala, H., Kukuła, I., Giza, K., Marciniak, B., Rózycka-Sokołowska, E., Drulis, H.: Evaluation of electrochemical hydrogenation and corrosion behavior of LaNi5-based materials using galvanostatic charge/discharge measurements. Int J Hydrogen Energy. 37, 16817–16822 (2012). https://doi.org/10.1016/J.IJHYDENE.2012.07.126

97. Stolz, L., Gaberšček, M., Winter, M., Kasnatscheew, J.: Different Efforts but Similar Insights in Battery R&D: Electrochemical Impedance Spectroscopy *vs* Galvanostatic (Constant Current) Technique. Chemistry of Materials. 34, 10272–10278 (2022). https://doi.org/10.1021/acs.chemmater.2c02376

98. Saxena, S., Xing, Y., Kwon, D., Pecht, M.: Accelerated degradation model for C-rate loading of lithium-ion batteries. International Journal of Electrical Power & Energy Systems. 107, 438–445 (2019). https://doi.org/10.1016/J.IJEPES.2018.12.016

99. Li, M., Song, Q., Xie, H., -, al, Alaniz, R.D., Gavilán-Arriazu, E.M., O Lépori, C.M., Lebreton, A., Lethien, C., Coleman, J.N.: Impact of Different Operational Voltage Windows in a Micro-Cycle Formation Process on NMC811||Graphite and NMC811||Graphite/SiOx Pouch Cells. J Electrochem Soc. 172, 040522 (2025). https://doi.org/10.1149/1945-7111/ADC953

100. Kissinger, P.T., Heineman, W.R.: Cyclic voltammetry. J Chem Educ. 60, 702 (1983). https://doi.org/10.1021/ed060p702

101. Lazanas, A.Ch., Prodromidis, M.I.: Electrochemical Impedance Spectroscopy–A Tutorial. ACS Measurement Science Au. 3, 162–193 (2023). https://doi.org/10.1021/acsmeasuresciau.2c00070

102. Mansfeld, F.: Recording and Analysis of AC Impedance Data for Corrosion StudiesI. Background and Methods of Analysis. Corrosion. 37, 301–307 (1981). https://doi.org/10.5006/1.3621688

103. Huang, J., Li, Z., Liaw, B.Y., Zhang, J.: Graphical analysis of electrochemical impedance spectroscopy data in Bode and Nyquist representations. J Power Sources. 309, 82–98 (2016). https://doi.org/10.1016/J.JPOWSOUR.2016.01.073

104. Abdi, Z., Vandichel, M., Sologubenko, A.S., Willinger, M.G., Shen, J.R., Allakhverdiev, S.I., Najafpour, M.M.: The importance of identifying the true catalyst when using Randles-Sevcik equation to calculate turnover frequency. Int J Hydrogen Energy. 46, 37774–37781 (2021). https://doi.org/10.1016/J.IJHYDENE.2021.09.039

105. Cruz-Manzo, S., Greenwood, P.: An impedance model based on a transmission line circuit and a frequency dispersion Warburg component for the study of EIS in Li-ion batteries. Journal of Electroanalytical Chemistry. 871, 114305 (2020). https://doi.org/10.1016/J.JELECHEM.2020.114305

106. Nowak, A.P., Rutecki, P., Szkoda, M., Trzciński, K.: Determination of Sodium Ion Diffusion Coefficient in Tin Sulfide@Carbon Anode Material Using GITT and EIS Techniques. Energies . 17, (2024). https://doi.org/10.3390/en17133233

107. Lee, H., Yang, S., Kim, S., Song, J., Park, J., Doh, C.-H., Ha, Y.-C., Kwon, T.-S., Lee, Y.M.: Understanding the effects of diffusion coefficient and exchange current density on the electrochemical model of lithium-ion batteries. Curr Opin Electrochem. 34, 100986 (2022). https://doi.org/10.1016/j.coelec.2022.100986

108. Dr. John-Joseph Marie: Cell Analysis and Modelling System (CAMS)

109. Saadatkhah, N., Carillo Garcia, A., Ackermann, S., Leclerc, P., Latifi, M., Samih, S., Patience, G.S., Chaouki, J.: Experimental methods in chemical engineering: Thermogravimetric analysis—TGA. Can J Chem Eng. 98, 34–43 (2020). https://doi.org/10.1002/CJCE.23673

110. Liu, Y., Zhang, R., Wang, J., Wang, Y.: iScience Perspective Current and future lithium-ion battery manufacturing. (2021). https://doi.org/10.1016/j.isci

111. Huang, C., Wilson, M.D., Suzuki, K., Liotti, E., Connolley, T., Magdysyuk, O. V., Collins, S., Van Assche, F., Boone, M.N., Veale, M.C., Lui, A., Wheater, R.M., Leung, C.L.A.: 3D Correlative Imaging of Lithium Ion Concentration in a Vertically Oriented Electrode Microstructure with a Density Gradient. Advanced Science. 9, (2022). https://doi.org/10.1002/advs.202105723

112. Märker, K., Reeves, P.J., Xu, C., Griffith, K.J., Grey, C.P.: Evolution of Structure and Lithium Dynamics in LiNi0.8Mn0.1Co0.1O2 (NMC811) Cathodes during Electrochemical Cycling. Chemistry of Materials. 31, 2545–2554 (2019). https://doi.org/10.1021/acs.chemmater.9b00140

113. Zapata Dominguez, D., Xu, J., Boudjema, Y., Ben Hadj Ali, S., Zanotto, F.M., Franco, A.A.: Influence of the mixing speed in the rheology of NMC622-based Li-ion battery

electrode slurries. Journal of Power Sources Advances. 26, 100141 (2024). https://doi.org/10.1016/J.POWERA.2024.100141

114. Väyrynen, A., Salminen, J.: Lithium ion battery production. J Chem Thermodyn. 46, 80–85 (2012). https://doi.org/10.1016/J.JCT.2011.09.005

115. Huang, Z., Deng, Z., Zhong, Y., Xu, M., Li, S., Liu, X., Zhou, Y., Huang, K., Shen, Y., Huang, Y.: Progress and challenges of prelithiation technology for lithium-ion battery. Carbon Energy. 4, 1107–1132 (2022). https://doi.org/10.1002/cey2.256

116. Goriparti, S., Miele, E., De Angelis, F., Di Fabrizio, E., Proietti Zaccaria, R., Capiglia, C.: Review on recent progress of nanostructured anode materials for Li-ion batteries. J Power Sources. 257, 421–443 (2014). https://doi.org/10.1016/J.JPOWSOUR.2013.11.103

117. Goriparti, S., Miele, E., De Angelis, F., Di Fabrizio, E., Proietti Zaccaria, R., Capiglia, C.: Review on recent progress of nanostructured anode materials for Li-ion batteries. J Power Sources. 257, 421–443 (2014). https://doi.org/10.1016/J.JPOWSOUR.2013.11.103

118. Bitsch, B., Dittmann, J., Schmitt, M., Scharfer, P., Schabel, W., Willenbacher, N.: A novel slurry concept for the fabrication of lithium-ion battery electrodes with beneficial properties. J Power Sources. 265, 81–90 (2014). https://doi.org/10.1016/j.jpowsour.2014.04.115

119. Park, J.H., Sung, S.H., Kim, S., Ahn, K.H.: Significant Agglomeration of Conductive Materials and the Dispersion State Change of the Ni-Rich NMC-Based Cathode Slurry during Storage. Ind Eng Chem Res. 61, 2100–2109 (2022). https://doi.org/10.1021/acs.iecr.1c04205

120. Bi, Y., Li, Q., Yi, R., Xiao, J.: To Pave the Way for Large-Scale Electrode Processing of Moisture-Sensitive Ni-Rich Cathodes. J Electrochem Soc. 169, 020521 (2022). https://doi.org/10.1149/1945-7111/ac4e5d

121. Huang, C., Wilson, M.D., Cline, B., Sivarajah, A., Stolp, W., Boone, M.N., Connolley, T., Leung, C.L.A.: Li+ concentration and morphological changes at the anode and cathode interphases inside solid-state lithium metal batteries. JPhys Energy. 7, (2025). https://doi.org/10.1088/2515-7655/adafda

122. Ke, X., Prahl, J.M., Alexander, J.I.D., Savinell, R.F.: Redox flow batteries with serpentine flow fields: Distributions of electrolyte flow reactant penetration into the porous carbon electrodes and effects on performance. J Power Sources. 384, 295–302 (2018). https://doi.org/10.1016/j.jpowsour.2018.03.001

123. Shojaei, M.J., Sivarajah, A., Safdar, T., Magdysyuke, O. V., Leung, C.L.A., Huang, C.: Advanced battery cathode microstructure analysis through operando synchrotron

X-ray tomography and super-resolution deep learning. Solid State Ion. 422, (2025). https://doi.org/10.1016/j.ssi.2025.116818

124. Balke, N., Jesse, S., Morozovska, A.N., Eliseev, E., Chung, D.W., Kim, Y., Adamczyk, L., García, R.E., Dudney, N., Kalinin, S. V.: Nanoscale mapping of ion diffusion in a lithium-ion battery cathode. Nat Nanotechnol. 5, 749–754 (2010). https://doi.org/10.1038/nnano.2010.174

125. Han, X., Lu, L., Zheng, Y., Feng, X., Li, Z., Li, J., Ouyang, M.: A review on the key issues of the lithium ion battery degradation among the whole life cycle. eTransportation. 1, 100005 (2019). https://doi.org/10.1016/j.etran.2019.100005

126. Ma, C., Cai, W., Zhu, Z., Ji, Z., Yang, J., Li, H., Wen, G., Zhao, Z., Fu, X., Yang, W., Wang, Y.: How Binder Nanofibration Affects the Active-Material Microenvironment in Battery Electrodes? Adv Funct Mater. (2024). https://doi.org/10.1002/adfm.202412193

127. Feng, L., Yan, R., Sun, X.R., Zhu, Z., Jia, W., Yan, X., Yang, Y.Y., Li, S., Fu, X., Yang, W., Wang, Y.: Cell-Membrane Inspired Multifunctional Nanocoating for Rescuing the Active-Material Microenvironment in High-Capacity Sulfur Cathode. Adv Energy Mater. 14, (2024). https://doi.org/10.1002/aenm.202303848

128. Zhu, Z., Wu, D., Feng, L., He, X., Hu, T., Ye, A., Fu, X., Yang, W., Wang, Y.: Architecting the Microenvironment Skeleton of Active Materials in High-Capacity Electrodes by Self-Assembled Nano-Building Blocks. Small. 20, (2024). https://doi.org/10.1002/smll.202307086

129. Leung, C.L.A., Wilson, M.D., Connolley, T., Collins, S.P., Magdysyuk, O. V., Boone, M.N., Suzuki, K., Veale, M.C., Liotti, E., Van Assche, F., Lui, A., Huang, C.: Correlative full field X-ray compton scattering imaging and X-ray computed tomography for in situ observation of Li ion batteries. Mater Today Energy. 31, (2023). https://doi.org/10.1016/j.mtener.2022.101224

130. Zheng, H., Li, J., Song, X., Liu, G., Battaglia, V.S.: A comprehensive understanding of electrode thickness effects on the electrochemical performances of Li-ion battery cathodes. Electrochim Acta. 71, 258–265 (2012). https://doi.org/10.1016/J.ELECTACTA.2012.03.161

131. Huang, L., Barker, K., Liu, X., Jian, Y., Skinner, S.J., Ryan, M.P., Huang, C.: A mixed-anion strategy for constructing rapid ion-conducting Na solid-state electrolyte. Chemistry of Inorganic Materials. 6, 100102 (2025). https://doi.org/10.1016/j.cinorg.2025.100102

132. Huang, C., Wilson, M.D., Cline, B., Sivarajah, A., Stolp, W., Boone, M.N., Connolley, T., Leung, C.L.A.: Correlating lithium-ion transport and interfacial lithium

microstructure evolution in solid-state batteries during the first cycle. Cell Rep Phys Sci. 5, (2024). https://doi.org/10.1016/j.xcrp.2024.101995

133. Zubi, G., Dufo-López, R., Carvalho, M., Pasaoglu, G.: The lithium-ion battery: State of the art and future perspectives. Renewable and Sustainable Energy Reviews. 89, 292–308 (2018). https://doi.org/10.1016/J.RSER.2018.03.002

134. Huang, C., Dontigny, M., Zaghib, K., Grant, P.S.: Low-tortuosity and graded lithium ion battery cathodes by ice templating. J Mater Chem A Mater. 7, 21421–21431 (2019). https://doi.org/10.1039/c9ta07269a

135. Rolandi, A.C., de Meatza, I., Casado, N., Forsyth, M., Mecerreyes, D., Pozo-Gonzalo, C.: Unlocking sustainable power: advances in aqueous processing and water-soluble binders for NMC cathodes in high-voltage Li-ion batteries. RSC Sustainability. 2, 2125–2149 (2024). https://doi.org/10.1039/D4SU00098F

136. Ruff, Z., Xu, C., Grey, C.P.: Transition Metal Dissolution and Degradation in NMC811-Graphite Electrochemical Cells. J Electrochem Soc. 168, 060518 (2021). https://doi.org/10.1149/1945-7111/ac0359

137. Jung, R., Metzger, M., Maglia, F., Stinner, C., Gasteiger, H.A.: Chemical versus electrochemical electrolyte oxidation on NMC111, NMC622, NMC811, LNMO, and conductive carbon. Journal of Physical Chemistry Letters. 8, 4820–4825 (2017). https://doi.org/10.1021/acs.jpclett.7b01927

138. Spotte-Smith, E.W.C., Petrocelli, T.B., Patel, H.D., Blau, S.M., Persson, K.A.: Elementary Decomposition Mechanisms of Lithium Hexafluorophosphate in Battery Electrolytes and Interphases. ACS Energy Lett. 8, 347–355 (2023). https://doi.org/10.1021/acsenergylett.2c02351

139. Stich, M., Göttlinger, M., Kurniawan, M., Schmidt, U., Bund, A.: Hydrolysis of LiPF6 in Carbonate-Based Electrolytes for Lithium-Ion Batteries and in Aqueous Media. Journal of Physical Chemistry C. 122, 8836–8842 (2018). https://doi.org/10.1021/acs.jpcc.8b02080

140. Nagler, F., Christian, N., Daubinger, P., Flegler, A., Hofmann, M., Giffin, G.A.: Unraveling the importance of water ratio in direct lithium-ion battery cathode recycling. Journal of Power Sources Advances. 24, (2023). https://doi.org/10.1016/j.powera.2023.100131

141. Neidhart, L., Fröhlich, K., Eshraghi, N., Cupid, D., Winter, F., Jahn, M.: Aqueous Manufacturing of Defect-Free Thick Multi-Layer NMC811 Electrodes. Nanomaterials. 12, (2022). https://doi.org/10.3390/nano12030317

142. Busà, C., Belekoukia, M., Loveridge, M.J.: The effects of ambient storage conditions on the structural and electrochemical properties of NMC-811 cathodes for Li-ion

batteries. Electrochim Acta. 366, (2021). https://doi.org/10.1016/j.electacta.2020.137358

143. Sahore, R., Wood, M., Kukay, A., Du, Z., Livingston, K.M., Wood, D.L., Li, J.: Performance of Different Water-Based Binder Formulations for Ni-Rich Cathodes Evaluated in LiNi 0.8 Mn 0.1 Co 0.1 O 2 //Graphite Pouch Cells . J Electrochem Soc. 169, 040567 (2022). https://doi.org/10.1149/1945-7111/ac682d

144. Liu, H., Yang, Y., Zhang, J.: Reaction mechanism and kinetics of lithium ion battery cathode material LiNiO2 with CO2. J Power Sources. 173, 556–561 (2007). https://doi.org/10.1016/J.JPOWSOUR.2007.04.083

145. Deville, S.: Freeze-Casting of Porous Ceramics: A Review of Current Achievements and Issues. Adv Eng Mater. 10, 155–169 (2008). https://doi.org/10.1002/adem.200700270

146. Boudenne, J.L., Cerclier, O., Galéa, J., Van der Vlist, E.: Electrochemical oxidation of aqueous phenol at a carbon black slurry electrode. Appl Catal A Gen. 143, 185–202 (1996). https://doi.org/10.1016/0926-860X(96)00027-0

147. Chang, W.J., Lee, G.H., Cheon, Y.J., Kim, J.T., Lee, S. Il, Kim, J., Kim, M., Park, W. Il, Lee, Y.J.: Direct Observation of Carboxymethyl Cellulose and Styrene-Butadiene Rubber Binder Distribution in Practical Graphite Anodes for Li-Ion Batteries. ACS Appl Mater Interfaces. 11, 41330–41337 (2019). https://doi.org/10.1021/acsami.9b13803

148. Li, T., Yuan, X.-Z., Zhang, L., Song, D., Shi, K., Bock, C.: Degradation Mechanisms and Mitigation Strategies of Nickel-Rich NMC-Based Lithium-Ion Batteries. Electrochemical Energy Reviews. 3, 43–80 (2020). https://doi.org/10.1007/s41918-019-00053-3

149. Li, T., Li, D., Zhang, Q., Gao, J., Zhang, L., Liu, X.: Improving Fast Charging-Discharging Performances of Ni-Rich LiNi0.8Co0.1Mn0.1O2 Cathode Material by Electronic Conductor LaNiO3 Crystallites. Materials. 15, (2022). https://doi.org/10.3390/ma15010396

150. Thapaliya, B.P., Misra, S., Yang, S. ze, Jafta, C.J., Meyer, H.M., Bagri, P., Unocic, R.R., Bridges, C.A., Dai, S.: Enhancing Cycling Stability and Capacity Retention of NMC811 Cathodes by Reengineering Interfaces via Electrochemical Fluorination. Adv Mater Interfaces. 9, (2022). https://doi.org/10.1002/admi.202200035

151. Märker, K., Xu, C., Grey, C.P.: Operando NMR of NMC811/Graphite Lithium-Ion Batteries: Structure, Dynamics, and Lithium Metal Deposition. J Am Chem Soc. 142, 17447–17456 (2020). https://doi.org/10.1021/jacs.0c06727

152. Quilty, C.D., Luo, J., Rodriguez-Campos, A., Liu, S., West, P.J., Tong, X., Kiss, A., Yang, Y., Jaye, C., Fischer, D.A., Takeuchi, E.S., Marschilok, A.C., Bock, D.C., Yan, S., Takeuchi, K.J.: Capacity Fade of Graphite/NMC811: Influence of Particle Morphology, Electrolyte, and Charge Voltage. J Electrochem Soc. 171, 080515 (2024). https://doi.org/10.1149/1945-7111/ad6a90

153. Wu, F., Yushin, G.: Conversion cathodes for rechargeable lithium and lithium-ion batteries. Energy Environ Sci. 10, 435–459 (2017). https://doi.org/10.1039/C6EE02326F

154. Wei, L., Wu, H., Liu, S., Zhou, Y., Guo, X.: Construction of Hierarchical Conductive Networks for LiNi0.8Mn0.1Co0.1O2 Cathode toward Stable Cycling at High Areal Mass Loadings. Small. (2024). https://doi.org/10.1002/smll.202312059

155. McNulty, R.C., Hampson, E., Cutler, L.N., Grey, C.P., Dose, W.M., Johnson, L.R.: Understanding the limits of Li-NMC811 half-cells. J Mater Chem A Mater. 11, 18302–18312 (2023). https://doi.org/10.1039/d3ta00912b

156. Wan, S., Chen, S.: A dithiol-based new electrolyte additive for improving electrochemical performance of NCM811 lithium ion batteries. https://doi.org/10.1007/s11581-020-03768-2/Published

157. Vivier, V., Orazem, M.E.: Impedance Analysis of Electrochemical Systems. Chem Rev. 122, 11131–11168 (2022). https://doi.org/10.1021/acs.chemrev.1c00876

158. Dose, W.M., Temprano, I., Allen, J.P., Björklund, E., O'Keefe, C.A., Li, W., Mehdi, B.L., Weatherup, R.S., De Volder, M.F.L., Grey, C.P.: Electrolyte Reactivity at the Charged Ni-Rich Cathode Interface and Degradation in Li-Ion Batteries. ACS Appl Mater Interfaces. 14, 13206–13222 (2022). https://doi.org/10.1021/acsami.1c22812

159. Hou, P., Li, F., Sun, Y., Li, H., Xu, X., Zhai, T.: Multishell Precursors Facilitated Synthesis of Concentration-Gradient Nickel-Rich Cathodes for Long-Life and High-Rate Lithium-Ion Batteries. ACS Appl Mater Interfaces. 10, 24508–24515 (2018). https://doi.org/10.1021/acsami.8b06286

160. González-Meza, O.A., Larios-Durán, E.R., Gutiérrez-Becerra, A., Casillas, N., Escalante, J.I., Bárcena-Soto, M.: Development of a Randles-Ševčík-like equation to predict the peak current of cyclic voltammetry for solid metal hexacyanoferrates. Journal of Solid State Electrochemistry. 23, 3123–3133 (2019). https://doi.org/10.1007/s10008-019-04410-6

161. Commandeur, D., Sabado, C., Ashton, T.E., Darr, J.A.: Combinatorial Performance Mapping of Near-NMC111 Li-ion Cathodes. Journal of Materiomics. 8, 437–445 (2022). https://doi.org/10.1016/j.jmat.2021.07.003

162. McNulty, R.C., Hampson, E., Cutler, L.N., Grey, C.P., Dose, W.M., Johnson, L.R.: Understanding the limits of Li-NMC811 half-cells. J Mater Chem A Mater. 11, 18302–18312 (2023). https://doi.org/10.1039/d3ta00912b

163. Sun, X.-G., Jafta, C.J., Tan, S., Borisevich, A., Gupta, R.B., Paranthaman, M.P.: Facile Surface Coatings for Performance Improvement of NMC811 Battery Cathode Material. J Electrochem Soc. 169, 020565 (2022). https://doi.org/10.1149/1945-7111/ac5302

164. McNulty, R.C., Hampson, E., Cutler, L.N., Grey, C.P., Dose, W.M., Johnson, L.R.: Understanding the limits of Li-NMC811 half-cells. J Mater Chem A Mater. 11, 18302–18312 (2023). https://doi.org/10.1039/d3ta00912b

165. Kühn, S.P., Weiling, M., Diddens, D., Baghernejad, M., Winter, M., Cekic-Laskovic, I.: Impact of in coin cell atmosphere on lithium metal battery performance. Energy Materials. (2023). https://doi.org/10.20517/energymater.2023.07

166. Jung, R., Metzger, M., Maglia, F., Stinner, C., Gasteiger, H.A.: Chemical versus electrochemical electrolyte oxidation on NMC111, NMC622, NMC811, LNMO, and conductive carbon. Journal of Physical Chemistry Letters. 8, 4820–4825 (2017). https://doi.org/10.1021/acs.jpclett.7b01927

167. Huang, X.: Separator technologies for lithium-ion batteries. Journal of Solid State Electrochemistry. 15, 649–662 (2011). https://doi.org/10.1007/s10008-010-1264-9

168. Fantham, T.L., Gladwin, D.T.: An overview of safety for laboratory testing of lithium-ion batteries. Energy Reports. 7, 2–8 (2021). https://doi.org/10.1016/J.EGYR.2021.03.004

169. Faraji Niri, M., Reynolds, C., Román Ramírez, L.A., Kendrick, E., Marco, J.: Systematic analysis of the impact of slurry coating on manufacture of Li-ion battery electrodes via explainable machine learning. Energy Storage Mater. 51, 223–238 (2022). https://doi.org/10.1016/J.ENSM.2022.06.036

170. Daems, K., Yadav, P., Dermenci, K.B., Van Mierlo, J., Berecibar, M.: Advances in inorganic, polymer and composite electrolytes: Mechanisms of Lithium-ion transport and pathways to enhanced performance. Renewable and Sustainable Energy Reviews. 191, 114136 (2024). https://doi.org/10.1016/J.RSER.2023.114136

171. Allard, J., Burgers, S., Rodríguez González, M.C., Zhu, Y., De Feyter, S., Koos, E.: Effects of particle roughness on the rheology and structure of capillary suspensions. Colloids Surf A Physicochem Eng Asp. 648, 129224 (2022). https://doi.org/10.1016/J.COLSURFA.2022.129224

172. Park, J., Ahn, K.H.: Controlling Drying Stress and Mechanical Properties of Battery Electrodes Using a Capillary Force-Induced Suspension System. Ind Eng Chem Res. 60, 4873–4882 (2021). https://doi.org/10.1021/acs.iecr.0c06130

173. Huang, C., Grant, P.S.: Coral-like directional porosity lithium ion battery cathodes by ice templating. J Mater Chem A Mater. 6, 14689–14699 (2018). https://doi.org/10.1039/c8ta05049j

174. Huang, C., Dontigny, M., Zaghib, K., Grant, P.S.: Low-tortuosity and graded lithium ion battery cathodes by ice templating. J Mater Chem A Mater. 7, 21421–21431 (2019). https://doi.org/10.1039/c9ta07269a

175. Leung, C.L.A., Wilson, M.D., Connolley, T., Collins, S.P., Magdysyuk, O. V., Boone, M.N., Suzuki, K., Veale, M.C., Liotti, E., Van Assche, F., Lui, A., Huang, C.: Correlative full field X-ray compton scattering imaging and X-ray computed tomography for in situ observation of Li ion batteries. Mater Today Energy. 31, (2023). https://doi.org/10.1016/j.mtener.2022.101224

176. Bi, Y., Li, Q., Yi, R., Xiao, J.: To Pave the Way for Large-Scale Electrode Processing of Moisture-Sensitive Ni-Rich Cathodes. J Electrochem Soc. 169, 020521 (2022). https://doi.org/10.1149/1945-7111/ac4e5d

177. Li, G., Su, J., Huang, C.: Battery Cathode with Vertically Aligned Microstructure Fabricated by Directional Ice Templating. Small Science. (2025). https://doi.org/10.1002/smsc.202500198

178. Keppeler, M., Tran, H.-Y., Braunwarth, W.: The Role of Pilot Lines in Bridging the Gap Between Fundamental Research and Industrial Production for Lithium-Ion Battery Cells Relevant to Sustainable Electromobility: A Review. Energy Technology. 9, (2021). https://doi.org/10.1002/ente.202100132

179. Hidalgo, M.F.V., Apachitei, G., Dogaru, D., Faraji-Niri, M., Lain, M., Copley, M., Marco, J.: Design of experiments for optimizing the calendering process in Li-ion battery manufacturing. J Power Sources. 573, 233091 (2023). https://doi.org/10.1016/J.JPOWSOUR.2023.233091

180. Zhu, P., Slater, P.R., Kendrick, E.: Insights into architecture, design and manufacture of electrodes for lithium-ion batteries. Mater Des. 223, 111208 (2022). https://doi.org/10.1016/J.MATDES.2022.111208

181. Ngandjong, A.C., Lombardo, T., Primo, E.N., Chouchane, M., Shodiev, A., Arcelus, O., Franco, A.A.: Investigating electrode calendering and its impact on electrochemical performance by means of a new discrete element method model: Towards a digital twin of Li-Ion battery manufacturing. J Power Sources. 485, 229320 (2021). https://doi.org/10.1016/J.JPOWSOUR.2020.229320

182. Sun, W., Huang, C.: Elucidating the effect of electrode calendering on electrochemical performance using 3D image-based modelling. J Power Sources. 611, 234774 (2024). https://doi.org/10.1016/J.JPOWSOUR.2024.234774

183. Li, M., Dai, X., Gao, W., Bai, H.: Ice-Templated Fabrication of Porous Materials with Bioinspired Architecture and Functionality. Acc Mater Res. 3, 1173–1185 (2022). https://doi.org/10.1021/accountsmr.2c00169

184. Kim, J., Jeong, H., Oh, E., Jang, J., Lee, S.W., Kim, D.-H., Han, S.-D., Kim, J., Yang, J.: Negative Effect of the Calendering Process on the Interphase Formation and Electrochemical Behavior of Reduced Graphene Oxide Electrodes. ACS Appl Mater Interfaces. 16, (2024). https://doi.org/10.1021/acsami.4c09721

185. Zhan, R., Ren, D., Liu, S., Chen, Z., Liu, X., Wang, W., Fu, L., Wang, X., Tu, S., Ou, Y., Ge, H., Wong, A.J.Y., Seh, Z.W., Wang, L., Sun, Y.: A Paradigm of Calendaring-Driven Electrode Microstructure for Balanced Battery Energy Density and Power Density. Adv Energy Mater. 13, (2023). https://doi.org/10.1002/aenm.202202544

186. Li, R., Li, W., Singh, A., Ren, D., Hou, Z., Ouyang, M.: Effect of external pressure and internal stress on battery performance and lifespan. Energy Storage Mater. 52, 395–429 (2022). https://doi.org/10.1016/J.ENSM.2022.07.034

187. Müller, V., Scurtu, R.G., Memm, M., Danzer, M.A., Wohlfahrt-Mehrens, M.: Study of the influence of mechanical pressure on the performance and aging of Lithium-ion battery cells. J Power Sources. 440, 227148 (2019). https://doi.org/10.1016/J.JPOWSOUR.2019.227148

188. Sun, W., Huang, C.: Elucidating the effect of electrode calendering on electrochemical performance using 3D image-based modelling. J Power Sources. 611, 234774 (2024). https://doi.org/10.1016/J.JPOWSOUR.2024.234774

189. Quilty, C.D., Luo, J., Rodriguez-Campos, A., Liu, S., West, P.J., Tong, X., Kiss, A., Yang, Y., Jaye, C., Fischer, D.A., Takeuchi, E.S., Marschilok, A.C., Bock, D.C., Yan, S., Takeuchi, K.J.: Capacity Fade of Graphite/NMC811: Influence of Particle Morphology, Electrolyte, and Charge Voltage. J Electrochem Soc. 171, 080515 (2024). https://doi.org/10.1149/1945-7111/AD6A90

190. Neidhart, L., Fröhlich, K., Eshraghi, N., Cupid, D., Winter, F., Jahn, M.: Aqueous Manufacturing of Defect-Free Thick Multi-Layer NMC811 Electrodes. Nanomaterials. 12, (2022). https://doi.org/10.3390/nano12030317

191. Tao, R., Gu, Y., Du, Z., Lyu, X., Li, J.: Advanced electrode processing for lithium-ion battery manufacturing. Nature Reviews Clean Technology. 1, 116–131 (2025). https://doi.org/10.1038/s44359-024-00018-w

192. Surace, Y., Jahn, M., Cupid, D.M.: The Rate Capability Performance of High-Areal-Capacity Water-Based NMC811 Electrodes: The Role of Binders and Current Collectors. Batteries. 10, (2024). https://doi.org/10.3390/batteries10030100

193. Keppeler, M., Roessler, S., Braunwarth, W.: Production Research as Key Factor for Successful Establishment of Battery Production on the Example of Large-Scale Automotive Cells Containing Nickel-Rich LiNi0.8Mn0.1Co0.1O2 Electrodes. Energy Technology. 8, (2020). https://doi.org/10.1002/ente.202000183

194. Shilpa, M.K., Raheman, M.A., Aabid, A., Baig, M., Veeresha, R.K., Kudva, N.: A Systematic Review of Thermoelectric Peltier Devices: Applications and Limitations. Fluid Dynamics and Materials Processing. 19, 187–206 (2022). https://doi.org/10.32604/fdmp.2022.020351

195. Nimmagadda, L.A., Mahmud, R., Sinha, S.: Materials and Devices for On-Chip and Off-Chip Peltier Cooling: A Review. IEEE Trans Compon Packaging Manuf Technol. 11, 1267–1281 (2021). https://doi.org/10.1109/TCPMT.2021.3095048

196. Sharma, T., Jain, P., Patel, S., Bhatt, N., Kathia, Prof.K.: A Review on Peltier Device and Heat Dissipation of It's Hot Surface Using Fins. Int J Res Appl Sci Eng Technol. 10, 1084–1094 (2022). https://doi.org/10.22214/ijraset.2022.40819

197. Boyce, A.M., Cumming, D.J., Huang, C., Zankowski, S.P., Grant, P.S., Brett, D.J.L., Shearing, P.R.: Design of Scalable, Next-Generation Thick Electrodes: Opportunities and Challenges. ACS Nano. 15, 18624–18632 (2021). https://doi.org/10.1021/acsnano.1c09687

198. Huang, C., Wilson, M.D., Suzuki, K., Liotti, E., Connolley, T., Magdysyuk, O. V., Collins, S., Van Assche, F., Boone, M.N., Veale, M.C., Lui, A., Wheater, R.M., Leung, C.L.A.: 3D Correlative Imaging of Lithium Ion Concentration in a Vertically Oriented Electrode Microstructure with a Density Gradient. Advanced Science. 9, (2022). https://doi.org/10.1002/advs.202105723

199. Song, W., Chen, M., Bai, F., Lin, S., Chen, Y., Feng, Z.: Non-uniform effect on the thermal/aging performance of Lithium-ion pouch battery. Appl Therm Eng. 128, 1165–1174 (2018). https://doi.org/10.1016/J.APPLTHERMALENG.2017.09.090

200. Zhang, G., Shaffer, C.E., Wang, C.-Y., Rahn, C.D.: Effects of Non-Uniform Current Distribution on Energy Density of Li-Ion Cells. J Electrochem Soc. 160, A2299–A2305 (2013). https://doi.org/10.1149/2.061311jes

201. Vaidyanathan, H., Kelly, W.H., Rao, G.: Heat dissipation in a lithium ion cell. J Power Sources. 93, 112–122 (2001). https://doi.org/10.1016/S0378-7753(00)00550-4

202. Bahru, R., Zamri, M.F.M.A., Shamsuddin, A.H., Shaari, N., Mohamed, M.A.: A review of thermal interface material fabrication method toward enhancing heat

dissipation. Int J Energy Res. 45, 3548–3568 (2021). https://doi.org/10.1002/er.6078

203. Mauler, L., Duffner, F., Leker, J.: Economies of scale in battery cell manufacturing: The impact of material and process innovations. Appl Energy. 286, 116499 (2021). https://doi.org/10.1016/J.APENERGY.2021.116499

204. Attia, P.M., Moch, E., Herring, P.K.: Challenges and opportunities for high-quality battery production at scale. Nat Commun. 16, 611 (2025). https://doi.org/10.1038/s41467-025-55861-7

205. Huang, C., Dontigny, M., Zaghib, K., Grant, P.S.: Low-tortuosity and graded lithium ion battery cathodes by ice templating. J Mater Chem A Mater. 7, 21421–21431 (2019). https://doi.org/10.1039/c9ta07269a

206. Bi, Y., Li, Q., Yi, R., Xiao, J.: To Pave the Way for Large-Scale Electrode Processing of Moisture-Sensitive Ni-Rich Cathodes. J Electrochem Soc. 169, 020521 (2022). https://doi.org/10.1149/1945-7111/ac4e5d

207. Chien, Y.-C., Liu, H., Menon, A., Brant, W., Brandell, D., Lacey, M.J.: A Fast Alternative to the Galvanostatic Intermittent Titration Technique, https://www.researchsquare.com/article/rs-960461/v1, (2021)

208. Rolandi, A.C., Pozo-Gonzalo, C., de Meatza, I., Casado, N., Mecerreyes, D., Forsyth, M.: Fluorine-Free Poly(ionic Liquid)s Binders for the Aqueous Processing of High-Voltage NMC811 Cathodes. Advanced Energy and Sustainability Research. 4, (2023). https://doi.org/10.1002/aesr.202300149

209. McNulty, R.C., Hampson, E., Cutler, L.N., Grey, C.P., Dose, W.M., Johnson, L.R.: Understanding the limits of Li-NMC811 half-cells. J Mater Chem A Mater. 11, 18302–18312 (2023). https://doi.org/10.1039/d3ta00912b

210. Tarascon, J.-M., Armand, M.: Issues and challenges facing rechargeable lithium batteries. Nature. 414, 359–367 (2001). https://doi.org/10.1038/35104644

211. Nitta, N., Wu, F., Lee, J.T., Yushin, G.: Li-ion battery materials: present and future. Materials Today. 18, 252–264 (2015). https://doi.org/10.1016/J.MATTOD.2014.10.040

212. Li, M., Lu, J., Chen, Z., Amine, K.: 30 Years of Lithium-Ion Batteries. Advanced Materials. 30, (2018). https://doi.org/10.1002/adma.201800561

213. Tian, J., Xiong, R., Shen, W.: A review on state of health estimation for lithium ion batteries in photovoltaic systems. eTransportation. 2, 100028 (2019). https://doi.org/10.1016/J.ETRAN.2019.100028

214. Xu, B., Qian, D., Wang, Z., Meng, Y.S.: Recent progress in cathode materials research for advanced lithium ion batteries. Materials Science and Engineering: R: Reports. 73, 51–65 (2012). https://doi.org/10.1016/J.MSER.2012.05.003

215. Liu, T., Yu, Y., Yang, X.Y., Wang, J., Zhang, X.B.: Lithium and Stannum Hybrid Anodes for Flexible Wire-Type Lithium–Oxygen Batteries. Small Struct. 1, (2020). https://doi.org/10.1002/sstr.202000015

216. Goodenough, J.B., Park, K.-S.: The Li-Ion Rechargeable Battery: A Perspective. J Am Chem Soc. 135, 1167–1176 (2013). https://doi.org/10.1021/ja3091438

217. Dahn, J.R., Zheng, T., Liu, Y., Xue, J.S.: Mechanisms for Lithium Insertion in Carbonaceous Materials. Science (1979). 270, 590–593 (1995). https://doi.org/10.1126/science.270.5236.590

218. Etacheri, V., Marom, R., Elazari, R., Salitra, G., Aurbach, D.: Challenges in the development of advanced Li-ion batteries: a review. Energy Environ Sci. 4, 3243 (2011). https://doi.org/10.1039/c1ee01598b

219. Verbrugge, M.W., Koch, B.J.: Electrochemical Analysis of Lithiated Graphite Anodes. J Electrochem Soc. 150, A374 (2003). https://doi.org/10.1149/1.1553788

220. Wood, D.L., Li, J., Daniel, C.: Prospects for reducing the processing cost of lithium ion batteries. J Power Sources. 275, 234–242 (2015). https://doi.org/10.1016/J.JPOWSOUR.2014.11.019

221. Ebner, M., Marone, F., Stampanoni, M., Wood, V.: Visualization and Quantification of Electrochemical and Mechanical Degradation in Li Ion Batteries. Science (1979). 342, 716–720 (2013). https://doi.org/10.1126/science.1241882

222. Zheng, J., Xing, G., Jin, L., Lu, Y., Qin, N., Gao, S., Zheng, J.P.: Strategies and Challenge of Thick Electrodes for Energy Storage: A Review. Batteries. 9, 151 (2023). https://doi.org/10.3390/batteries9030151

223. Gao, Y., Yang, Y., Yang, T., Zhang, Z., Tang, L., Mao, Z., Zhang, Y., Luo, D., Chen, Z.: Design Lithium Exchanged Zeolite Based Multifunctional Electrode Additive for Ultra-High Loading Electrode Toward High Energy Density Lithium Metal Battery. Adv Energy Mater. 15, (2025). https://doi.org/10.1002/aenm.202403063

224. Kuang, Y., Chen, C., Kirsch, D., Hu, L.: Thick Electrode Batteries: Principles, Opportunities, and Challenges. Adv Energy Mater. 9, (2019). https://doi.org/10.1002/aenm.201901457

225. Grießl, D., Adam, A., Huber, K., Kwade, A.: Effect of the Slurry Mixing Process on the Structural Properties of the Anode and the Resulting Fast-Charging Performance of the Lithium-Ion Battery Cell. J Electrochem Soc. 169, 020531 (2022). https://doi.org/10.1149/1945-7111/ac4cdb

226. Ingried, V.F., Haryati, S., Syarif, N.: Hydrothermal LiTiO2 Cathode and Polyurethane Binder of High Current Lithium Ion Batteries. Int J Adv Sci Eng Inf Technol. 12, 1032–1036 (2022). https://doi.org/10.18517/ijaseit.12.3.12683

227. Qu, H., Hou, J., Tang, Y., Semenikhin, O., Skorobogatiy, M.: Thin flexible lithium-ion battery featuring graphite paper based current collectors with enhanced conductivity. Can J Chem. 95, 169–173 (2017). https://doi.org/10.1139/cjc-2015-0593

228. Potrykus, S., Kutt, F., Nieznanski, J., Morales, F.J.F.: Advanced lithium-ion battery model for power system performance analysis. Energies (Basel). 13, (2020). https://doi.org/10.3390/en13102411

229. Huang, C., Grant, P.S.: Coral-like directional porosity lithium ion battery cathodes by ice templating. J Mater Chem A Mater. 6, 14689–14699 (2018). https://doi.org/10.1039/c8ta05049j

230. Delattre, B., Amin, R., Sander, J., De Coninck, J., Tomsia, A.P., Chiang, Y.-M.: Impact of Pore Tortuosity on Electrode Kinetics in Lithium Battery Electrodes: Study in Directionally Freeze-Cast LiNi 0.8 Co 0.15 Al 0.05 O 2 (NCA) . J Electrochem Soc. 165, A388–A395 (2018). https://doi.org/10.1149/2.1321802jes

231. Ghasemi Yeklangi, A., Ghafari, A., Asgari Sima, F., Akbari, S.: Advancing lithium-ion battery manufacturing: novel technologies and emerging trends. J Appl Electrochem. 54, 2653–2682 (2024). https://doi.org/10.1007/s10800-024-02142-8

232. Stolze, C., Janoschka, T., Schubert, U.S., Müller, F.A., Flauder, S.: Directional Solidification with Constant Ice Front Velocity in the Ice-Templating Process. Adv Eng Mater. 18, 111–120 (2016). https://doi.org/10.1002/adem.201500235

233. Shen, L., Song, X., Xu, Y., Tian, R., Wang, Y., Li, P., Li, J., Bai, H., Zhu, H., Wang, D.: Patterned vascularization in a directional ice-templated scaffold of decellularized matrix. Eng Life Sci. 21, 683–692 (2021). https://doi.org/10.1002/elsc.202100034

234. Li, Z., Wang, C., Ding, X., Li, X., Yu, J., Li, Q., Qu, Y.: Effect of Slurry Thickness on the Quality of Aluminized Coatings. Materials. 15, (2022). https://doi.org/10.3390/ma15196758

235. Ma, H.Y., Li, Y.W., Yang, S.X., Cao, F., Gong, J., Deng, Y.L.: Effects of solvent and doping acid on the morphology of polyaniline prepared with the ice-templating method. Journal of Physical Chemistry C. 114, 9264–9269 (2010). https://doi.org/10.1021/jp101525q

236. Spiegel, S., Heckmann, T., Altvater, A., Diehm, R., Scharfer, P., Schabel, W.: Investigation of edge formation during the coating process of Li-ion battery

electrodes. J Coat Technol Res. 19, 121–130 (2022). https://doi.org/10.1007/s11998-021-00521-w

237. Reynolds, C.D., Hare, S.D., Slater, P.R., Simmons, M.J.H., Kendrick, E.: Rheology and Structure of Lithium-Ion Battery Electrode Slurries. Energy Technology. 10, (2022). https://doi.org/10.1002/ente.202200545

238. Cheng, W., Cui, D., Sun, Y., Liu, W., Xu, Y., Liu, B.: Cryogenic work-hardening behavior for a metastable austenitic stainless steel at liquid nitrogen temperature. Materials Science and Engineering: A. 861, 144352 (2022). https://doi.org/10.1016/J.MSEA.2022.144352

239. Jia, S.Q., Yang, F.: High thermal conductive copper/diamond composites: state of the art. J Mater Sci. 56, 2241–2274 (2021). https://doi.org/10.1007/s10853-020-05443-3

240. Guo, Y., Jiang, Y., Zhang, Q., Wan, D., Huang, C.: Directional LiFePO4 cathode structure by freeze tape casting to improve lithium ion diffusion kinetics. J Power Sources. 506, 230052 (2021). https://doi.org/10.1016/J.JPOWSOUR.2021.230052

241. Zhong, J., Wang, T., Wang, L., Peng, L., Fu, S., Zhang, M., Cao, J., Xu, X., Liang, J., Fei, H., Duan, X., Lu, B., Wang, Y., Zhu, J., Duan, X.: A Silicon Monoxide Lithium-Ion Battery Anode with Ultrahigh Areal Capacity. Nanomicro Lett. 14, (2022). https://doi.org/10.1007/s40820-022-00790-z

242. Zhang, B., Wang, L., Zhang, Y., Wang, X., Qiao, Y., Sun, S.G.: Reliable impedance analysis of Li-ion battery half-cell by standardization on electrochemical impedance spectroscopy (EIS). Journal of Chemical Physics. 158, (2023). https://doi.org/10.1063/5.0139347

243. Zeng, Z., Mei, B.A., Song, G., Hamza, M., Yan, Z., Wei, Q., Feng, H., Zuo, Z., Jia, B., Xiong, R.: Physical interpretation of the electrochemical impedance spectroscopy (EIS) characteristics for diffusion-controlled intercalation and surface-redox charge storage behaviors. J Energy Storage. 102, 114021 (2024). https://doi.org/10.1016/J.EST.2024.114021